Journees de l'ATPEM 2025

RÉPUBLIQUE FRANÇAISE
Liberté
Égalité
Fraternité

Unfolding the high-redshift Universe with GRBs

ANDREA SACCARDI
CNES Postdoctoral Fellow
@CEA/Irfu/DAp - AIM

Action Thématique des Phénomènes Extrêmes et Multi-Messagers

1 October 2025

The advent of JWST is revolutionizing the field

(i) The current redshift record for a galaxy observed with the JWST is z = 14.4
(ii) Galaxy observations at similar redshifts already show strong metal enrichment

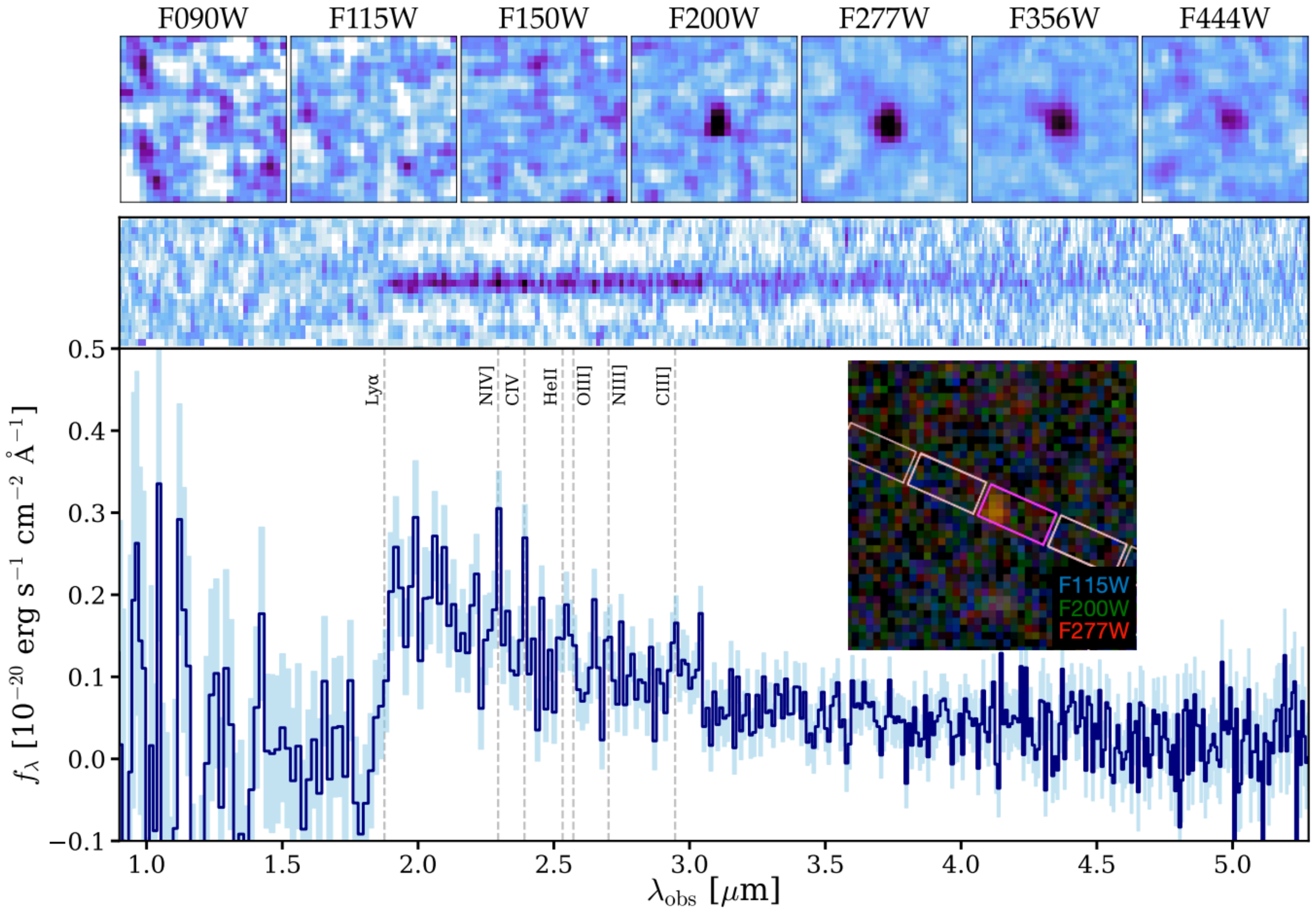

Naidu et al. 2025

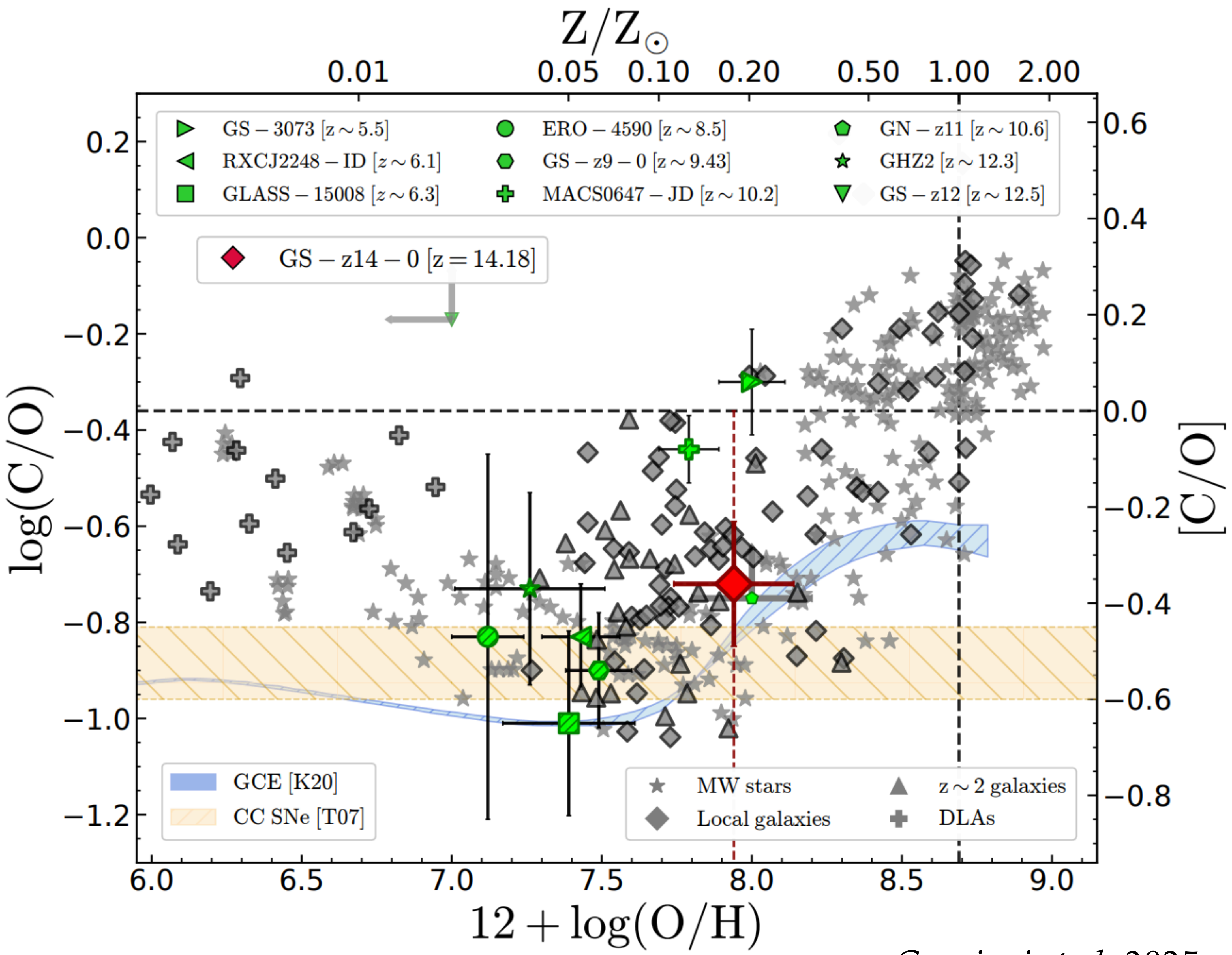

Carniani et al. 2025

The FAINTNESS of high-z galaxies limits the available diagnostics even for JWST

—> **FEW CONSTRAINTS ON THE PROPERTIES OF NEUTRAL COLD/WARM GAS IN GALAXIES**

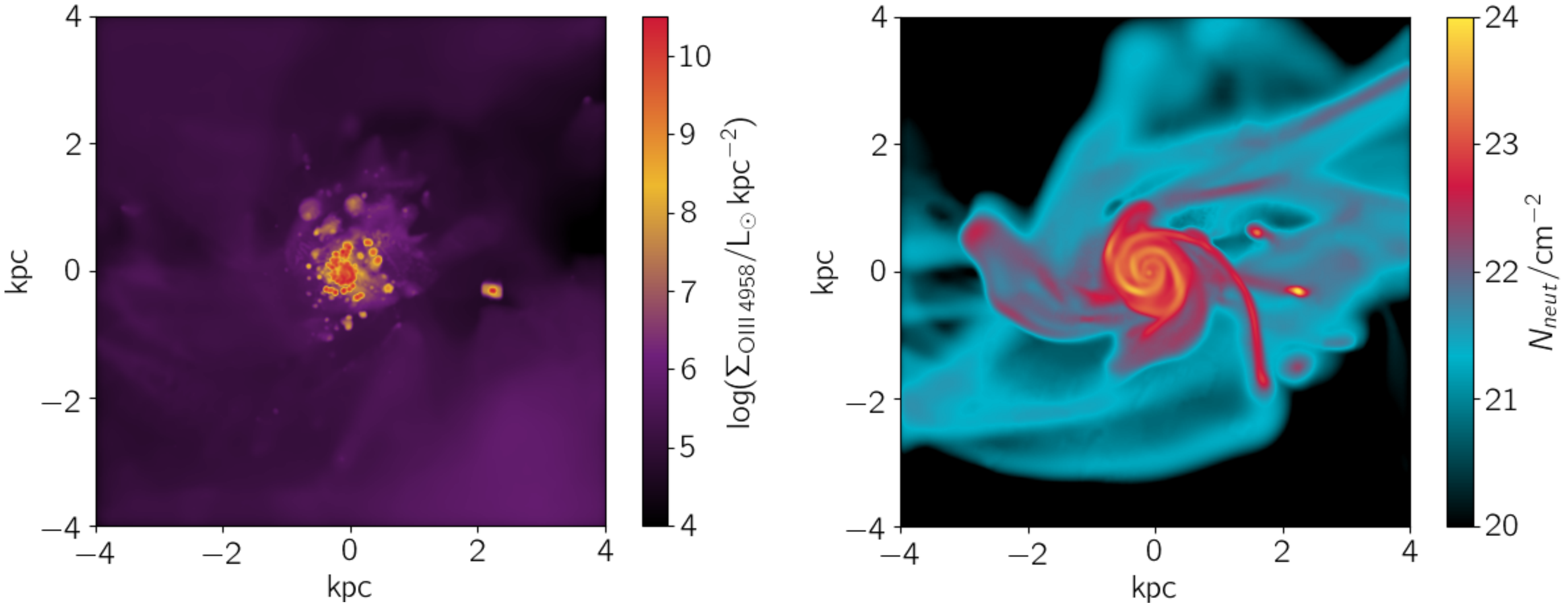

Credits: adapted from Pallottini et al. 2019

High-redshift Galaxies: Neutral Gas

Direct measurement of neutral hydrogen gas reservoirs in the local environments of galaxies at z > 8 with JWST!

Heintz et al. 2024

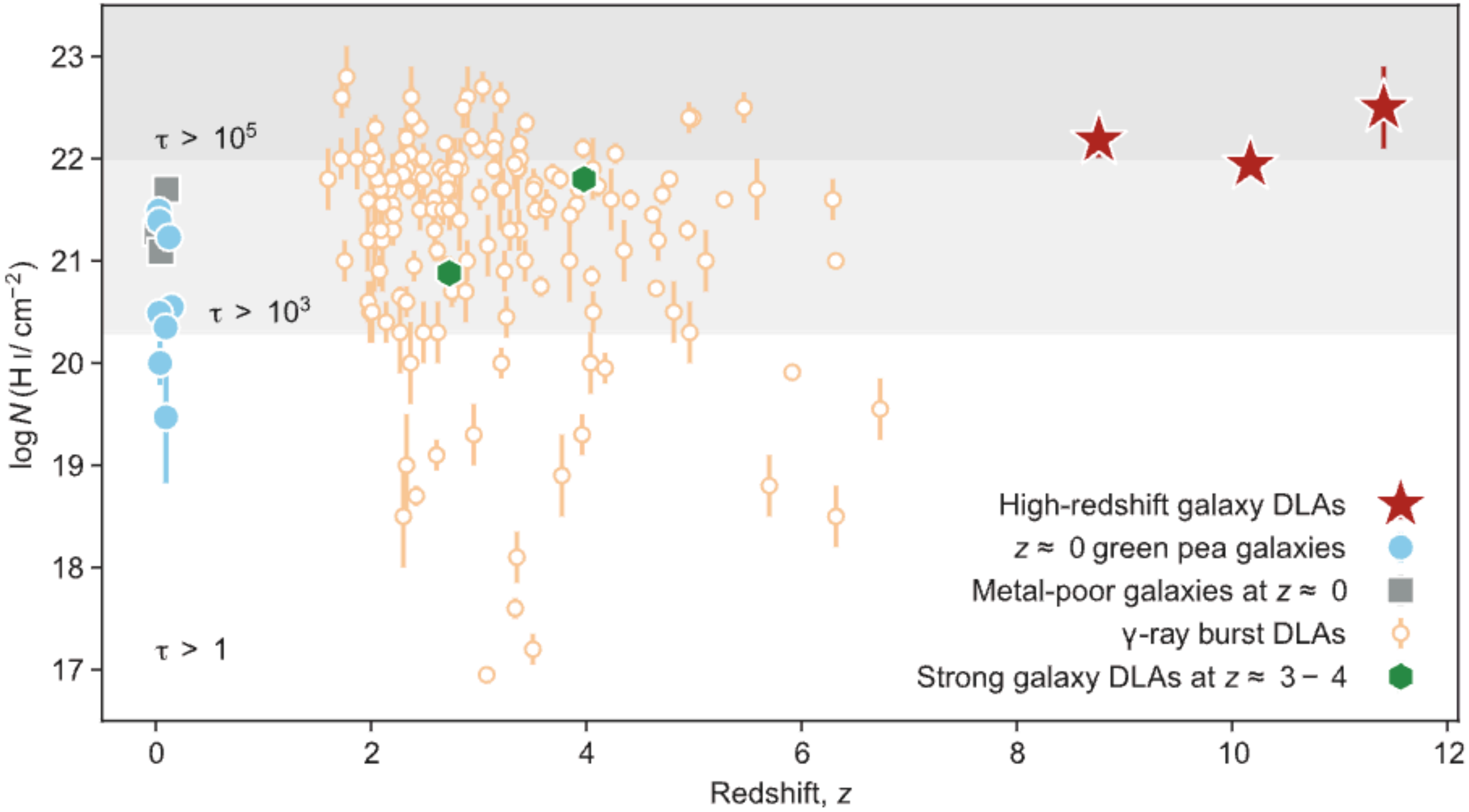

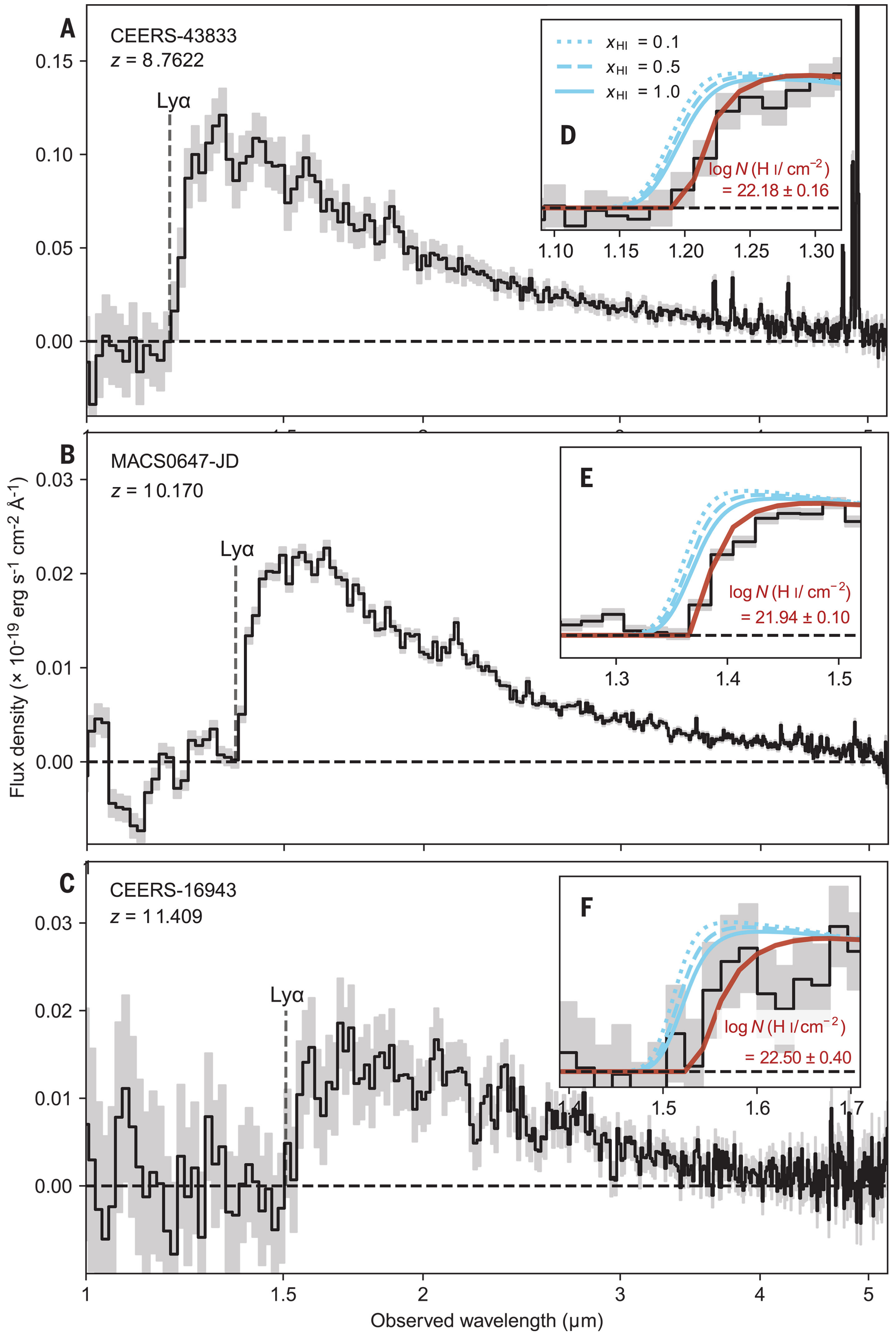

The GRB Phenomenon

Ultra-Relativistic Jet produced by a new-born accreting compact object

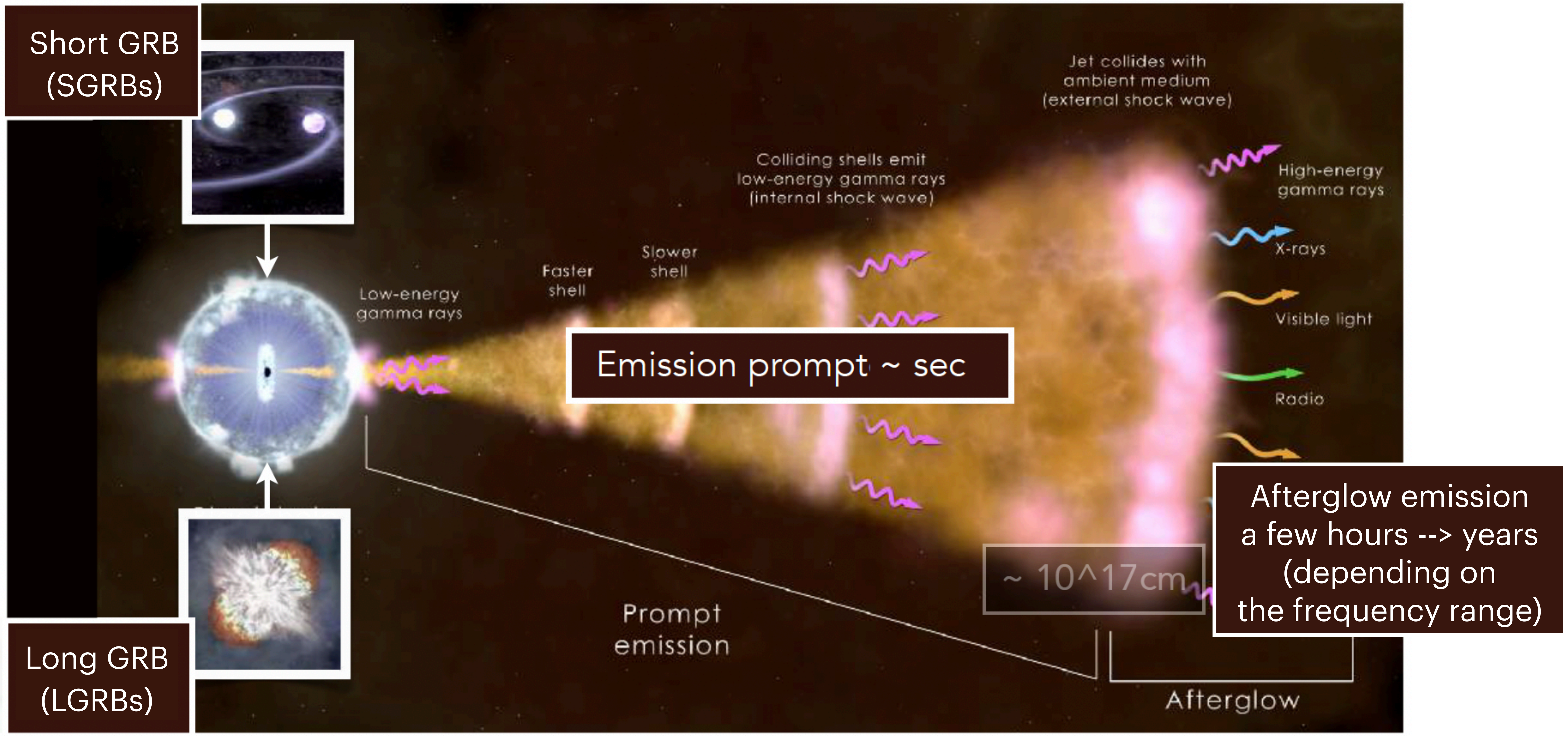

Credits: NASA

Long GRBs

1. Extremely bright at all redshift
2. Associated with the collapse of massive star
3. Trace star formation to the highest redshift
4. Afterglow emission fades

—> Study of the LGRB host (Neutral Gas + Ionised Gas)

LGRBs as probes of the high redshift Universe

GRBs ARE IDEAL TOOLS to explore the properties of faint high-redshift star-forming galaxies !

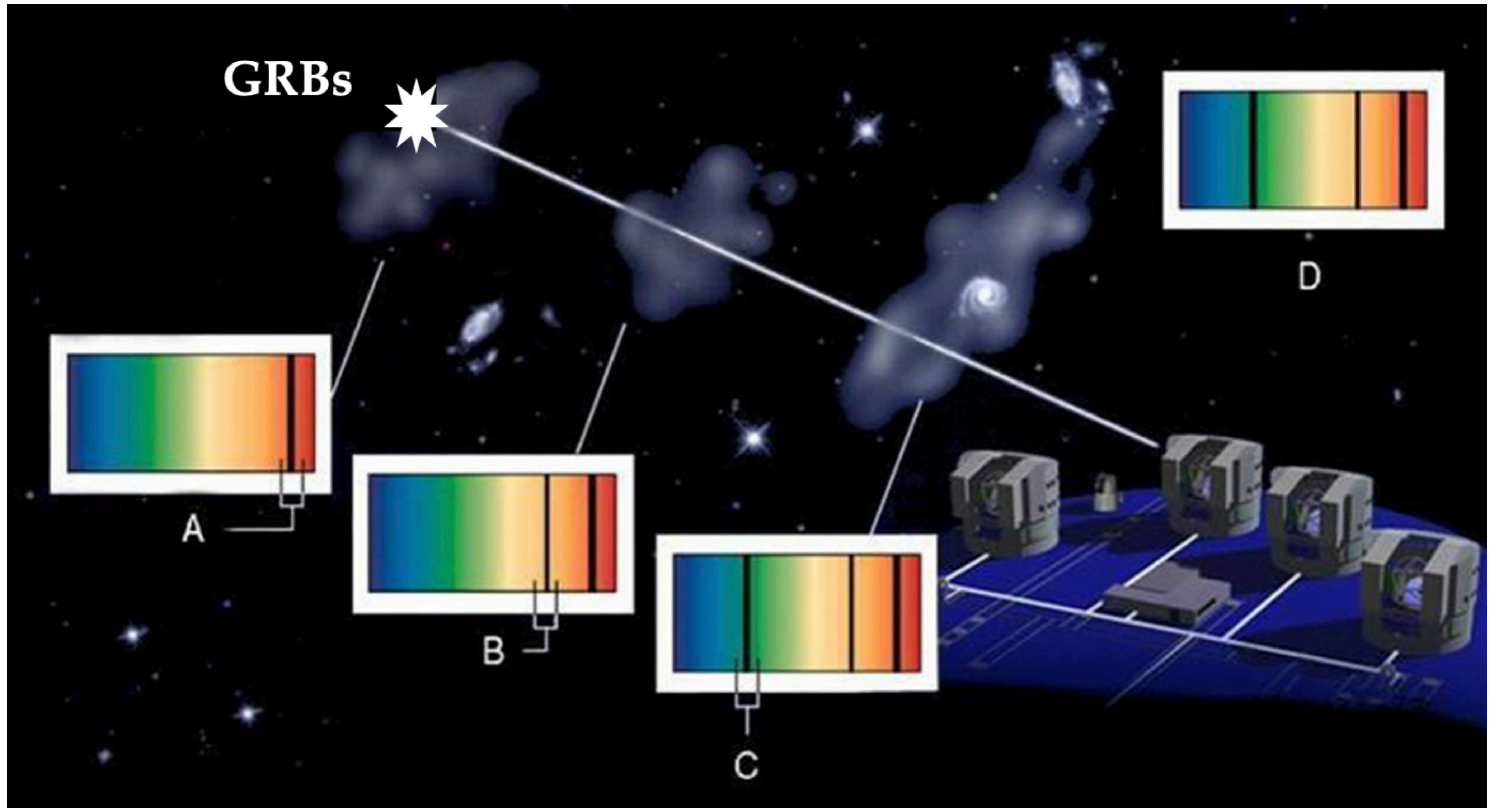

Credits: Adapted from ESO PR0813a

GRB 050730
z=3.968

~1h Observation

Chen et al. 2005; Nial Tanvir; Starling et al. 2005

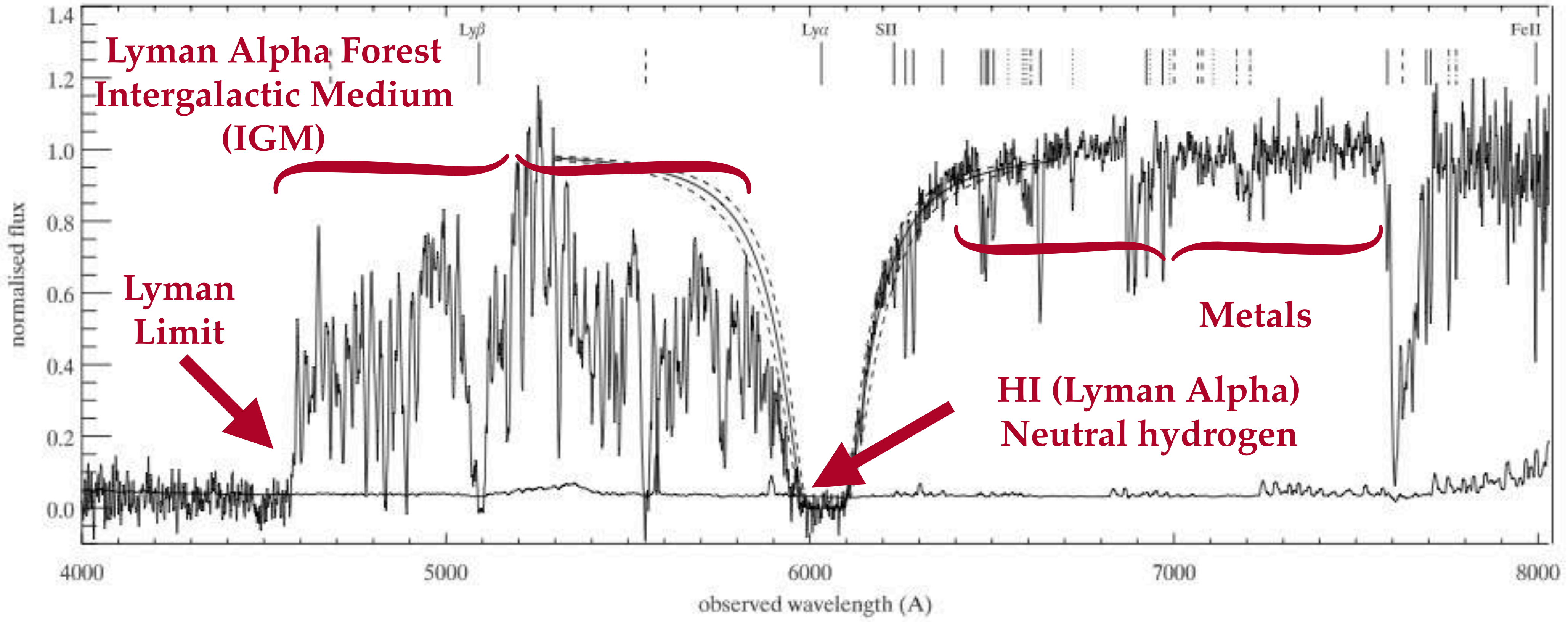

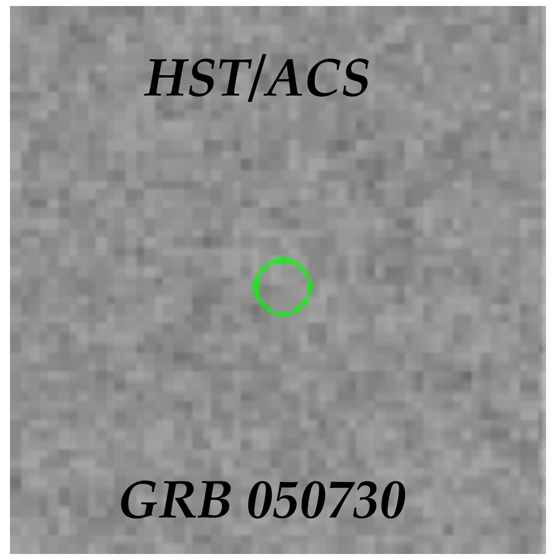

R>28.5

The powerful potential of LGRBs afterglow to access detailed information on the <u>neutral gas and its components</u>

<u>We can measure:</u>

- ➡ *Redshift of the absorbers*
- ➡ *Column densities of the ions of different chemical elements*

<u>To study:</u>

-Metallicity and dust depletion
-The distance of the corresponding gas clouds
-Kinematic of the gas
-Chemical abundance pattern

VLT follow-up

Stargate Collaboration

PIs: N. Tanvir, S.D. Vergani, D. Malesani

<u>ESO Large Programme</u>

GRBs Follow-up with optical-NIR telescopes

Credits: ESO/M. Claro

High-z GRBs

GRB 130606A
GRB 120521C
GRB 050904A
GRB 210905A
GRB 140515A
GRB 080913A
GRB 240218A
GRB 250314A
GRB 120923A
GRB 100905A
GRB 090423A
GRB 090429B
Redshift (z)
z=5.913
Lya break
Metal lines
z_{ph}~6
z=6.295
Lya break
Metal lines
z=6.312
Lya break
Metal lines
z=6.327
Lya break
z=6.733
Lya break
z=6.782
Lya break
Metal lines
z~7.3
Lya break
z~7.8
Lya break
z_{ph}~7.88
z~8.2
Lya break
z_{ph}~9.4

GRB 250314A

z~7.3

Credits: Cordier et al. 2025

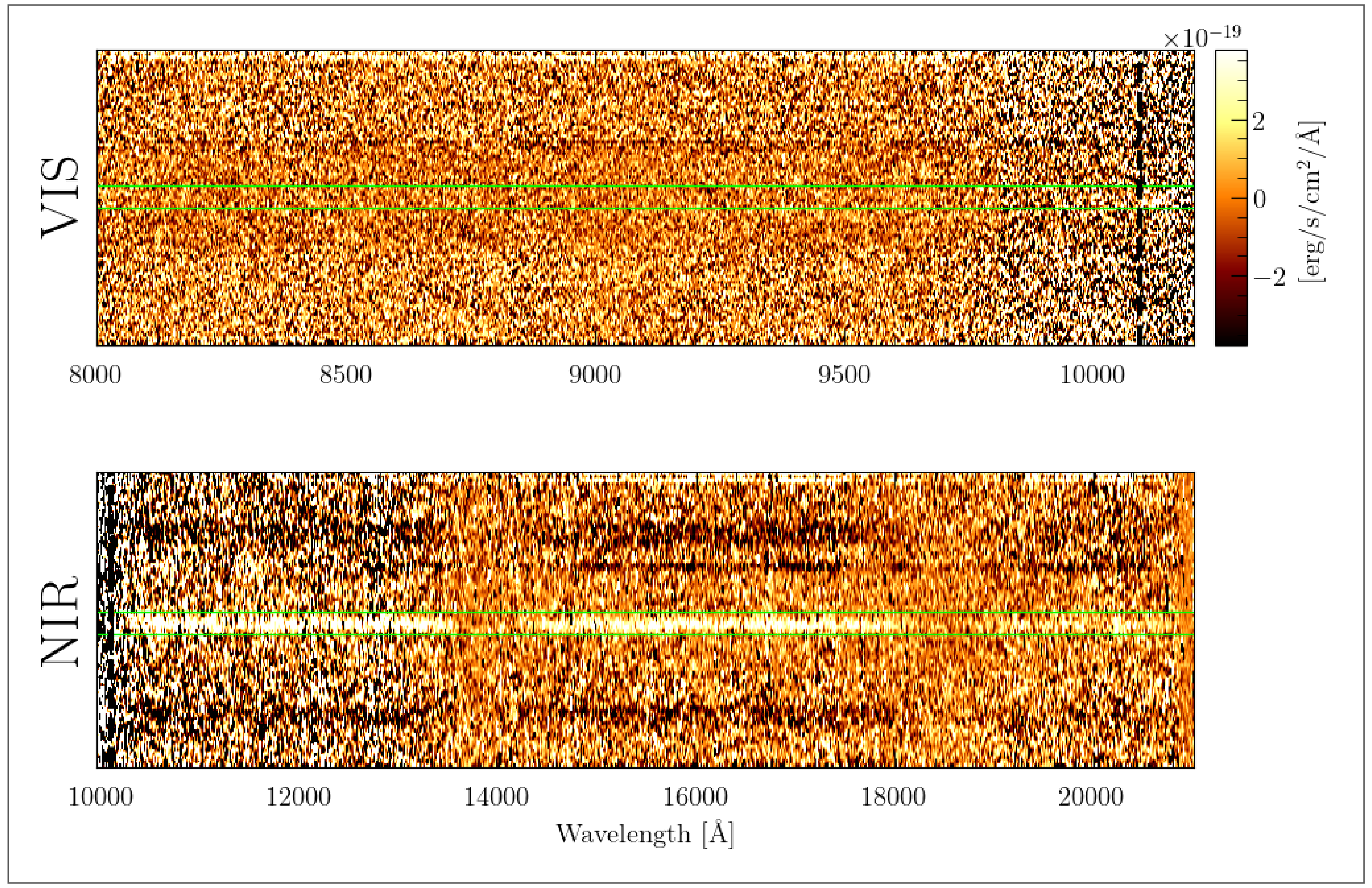

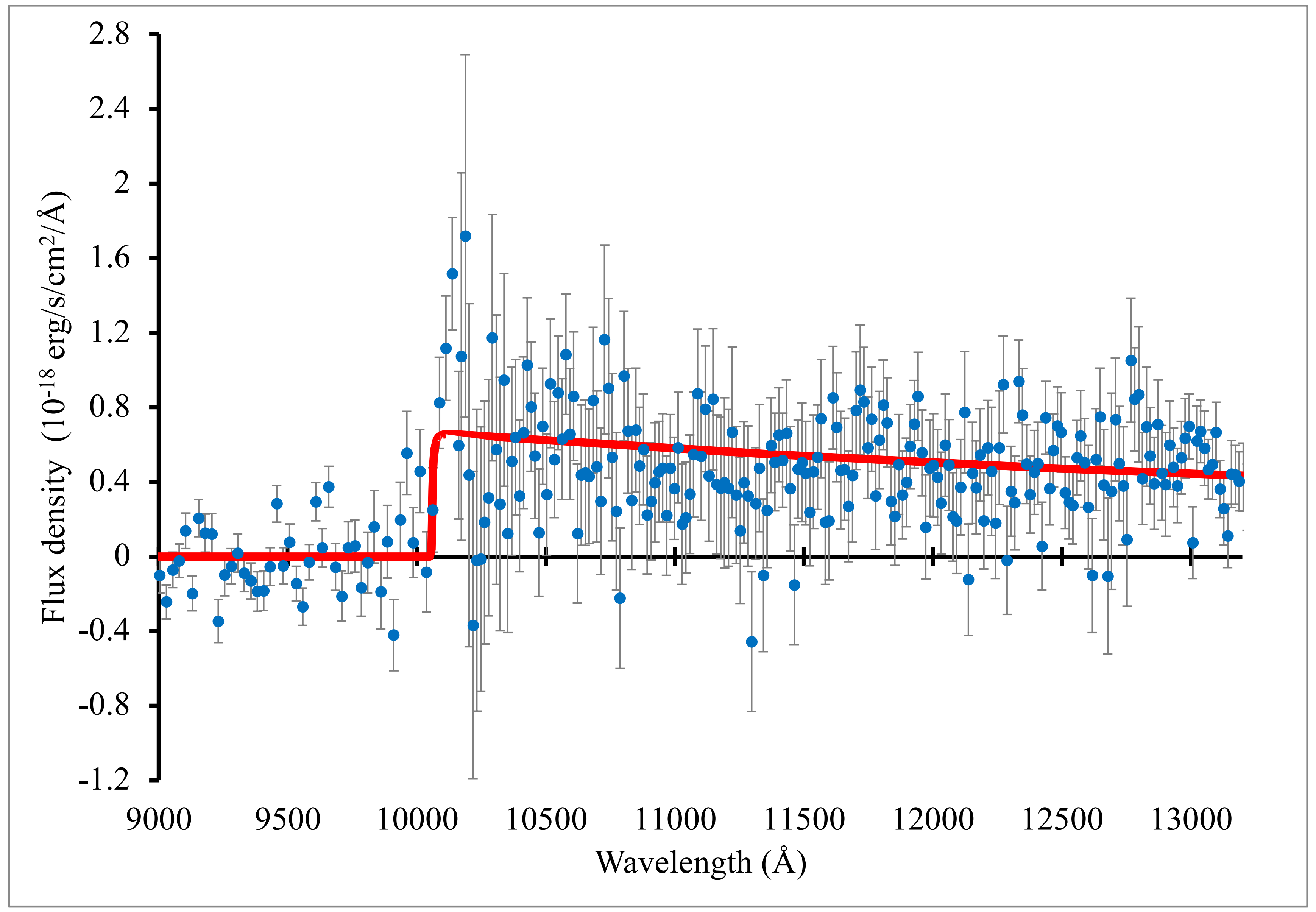

-High performance of VT in quickly identifying a potential high redshift candidate

-Synergy with other space satellites such as *Swift,* EP

-Powerful and successful follow-up with ground-based telescopes e.g. NOT and VLT

High-z GRBs


GRB 130606A
z=5.913
Lya break
Metal lines
GRB 120521C
zph~6
GRB 050904A
z=6.295
Lya break
Metal lines
GRB 210905A
z=6.312
Lya break
Metal lines
GRB 140515A
z=6.327
Lya break
GRB 080913A
z=6.733
Lya break
GRB 240218A
z=6.782
Lya break
Metal lines
GRB 250314A
z~7.3
Lya break
GRB 120923A
z=7.8
Lya break
GRB 100905A
zph~7.88
GRB 090423A
z=8.23
Lya break
GRB 090429B
zph~9.4
Redshift (z)

z = 6.312

Saccardi et al. 2023a
A&A 671, A84

GRB 210905A

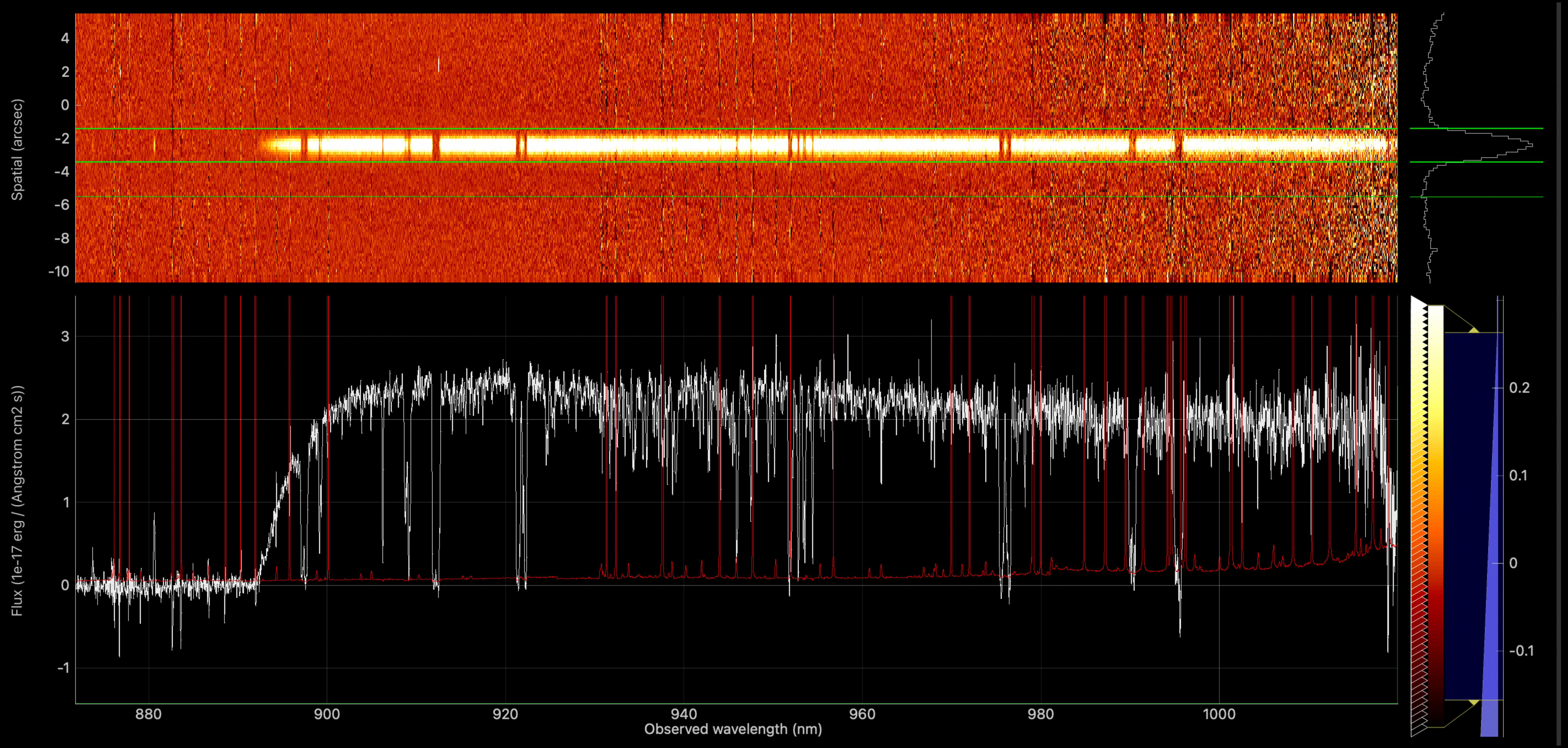

The case of GRB 210905A at z = 6.312

GRB210905A VLT/X-shooter Spectrum

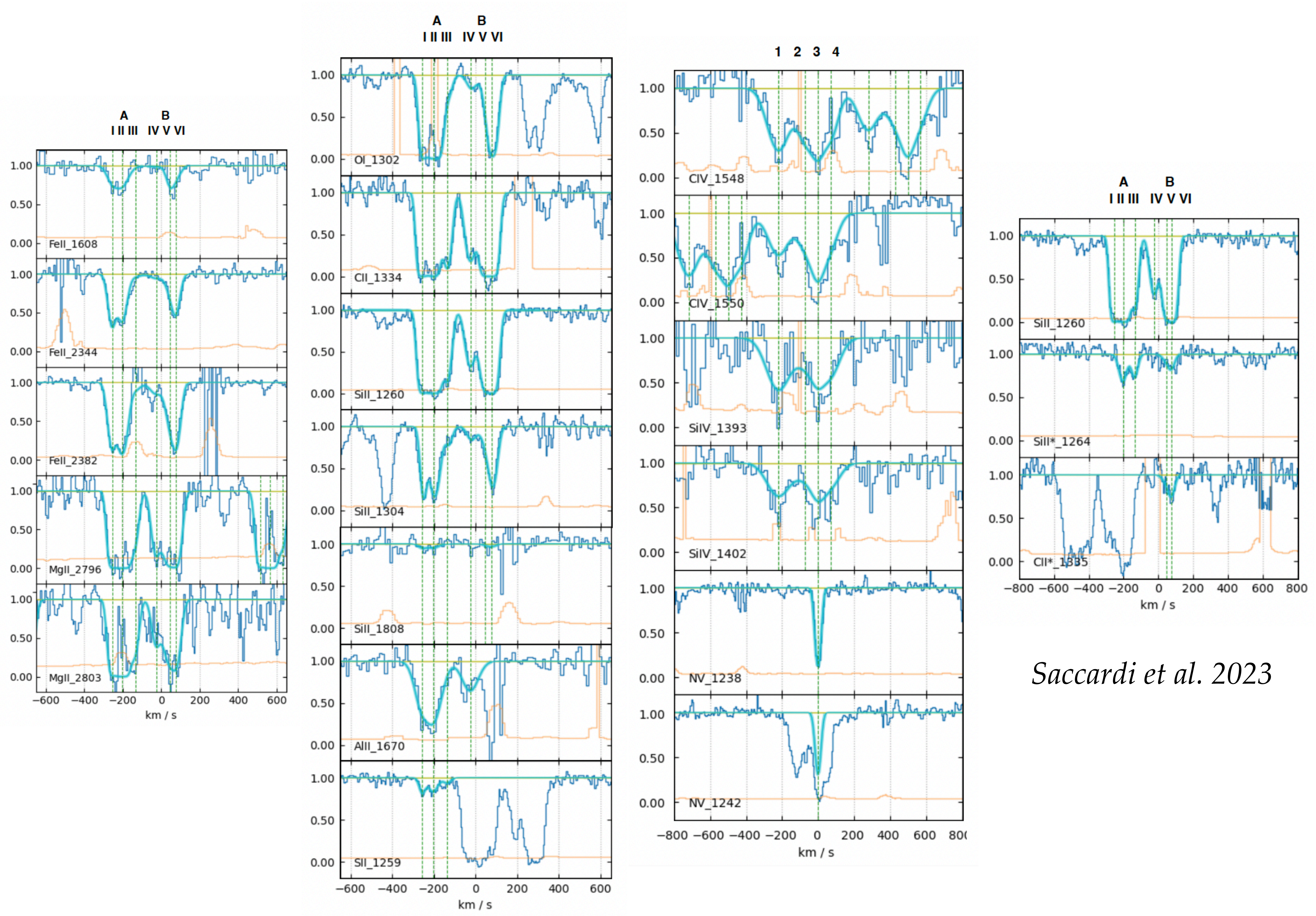

Saccardi et al. 2023

After ~2.53hr (obs frame)

GRB210905A HST/WFC3 Image

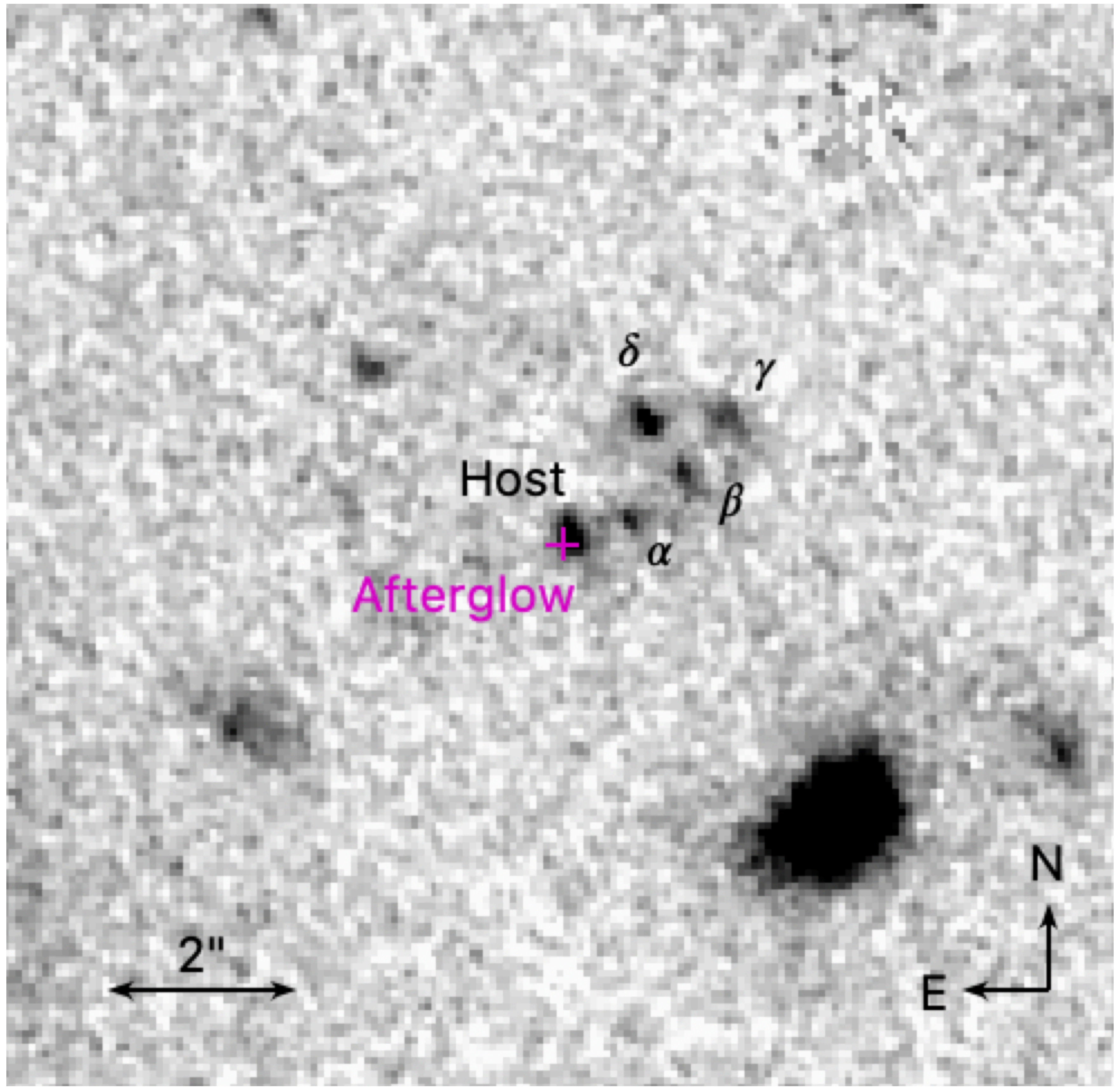

After ~250 days obs frame

ANDREA SACCARDI

The case of GRB 210905A at z = 6.312

We perform a detailed analysis of metallicity, chemical enrichment and dust depletion

The overall host galaxy

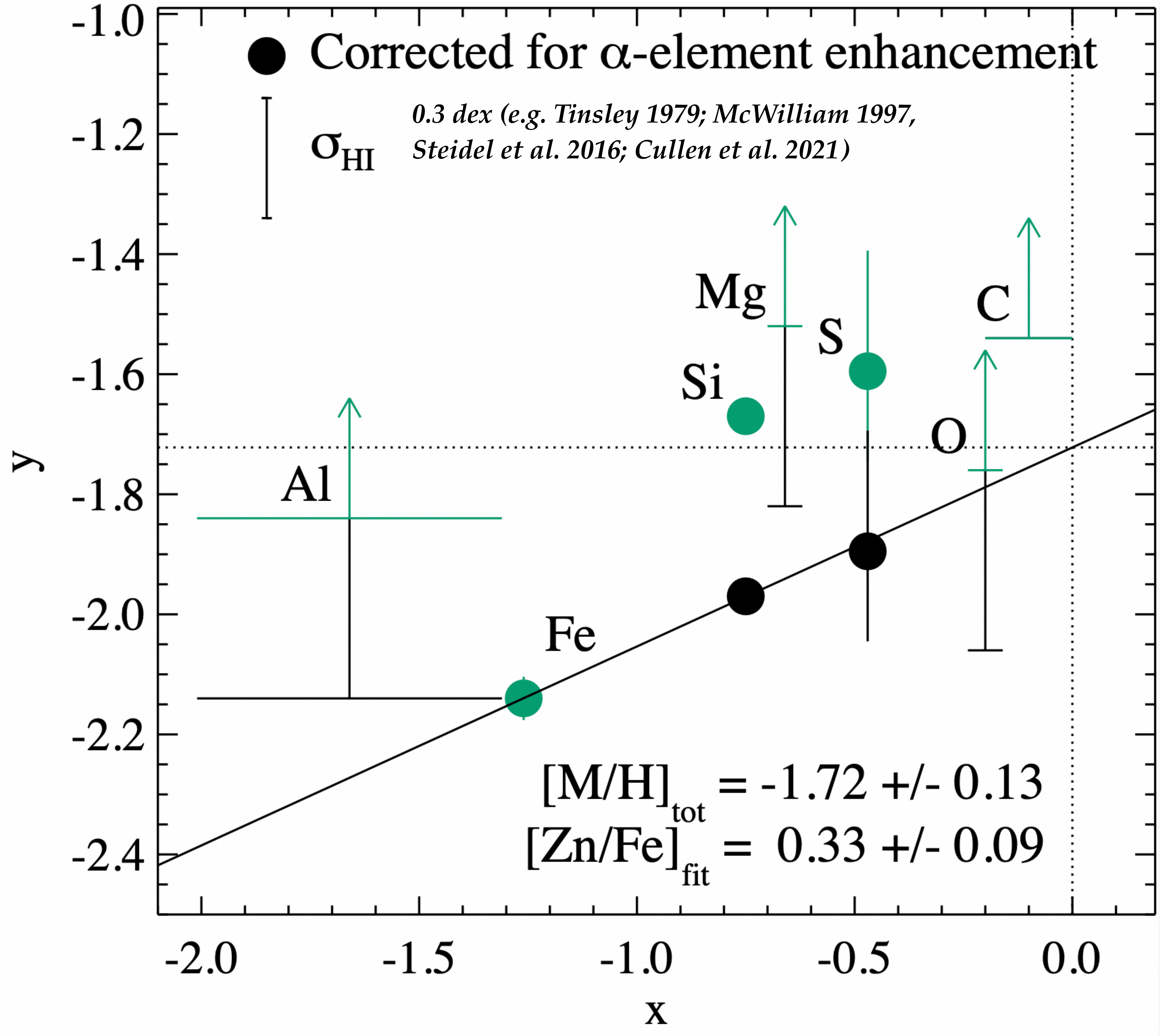

Saccardi et al. 2023

<u>*Following De Cia et al. 2016, De Cia et al. 2021*</u>

AXIS

X = How refractory is an element

Y = Elements abundances

FIT

Slope —> $[Zn/Fe]_{fit}$

Intercept —> $[M/H]_{tot}$

The case of GRB 210905A at z = 6.312

We perform a detailed analysis of metallicity, chemical enrichment and dust depletion

The overall host galaxy

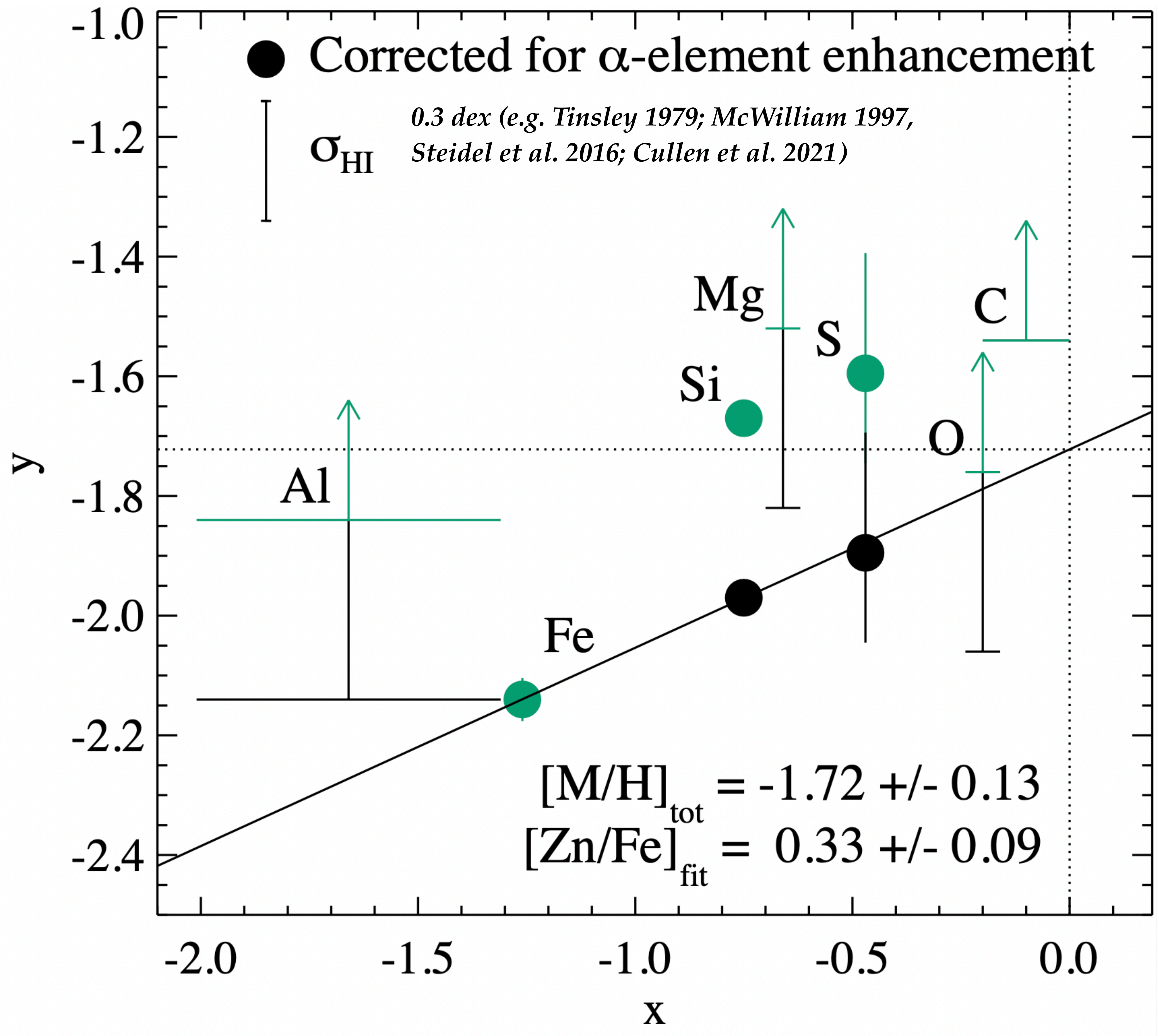

Saccardi et al. 2023

Component-by-component

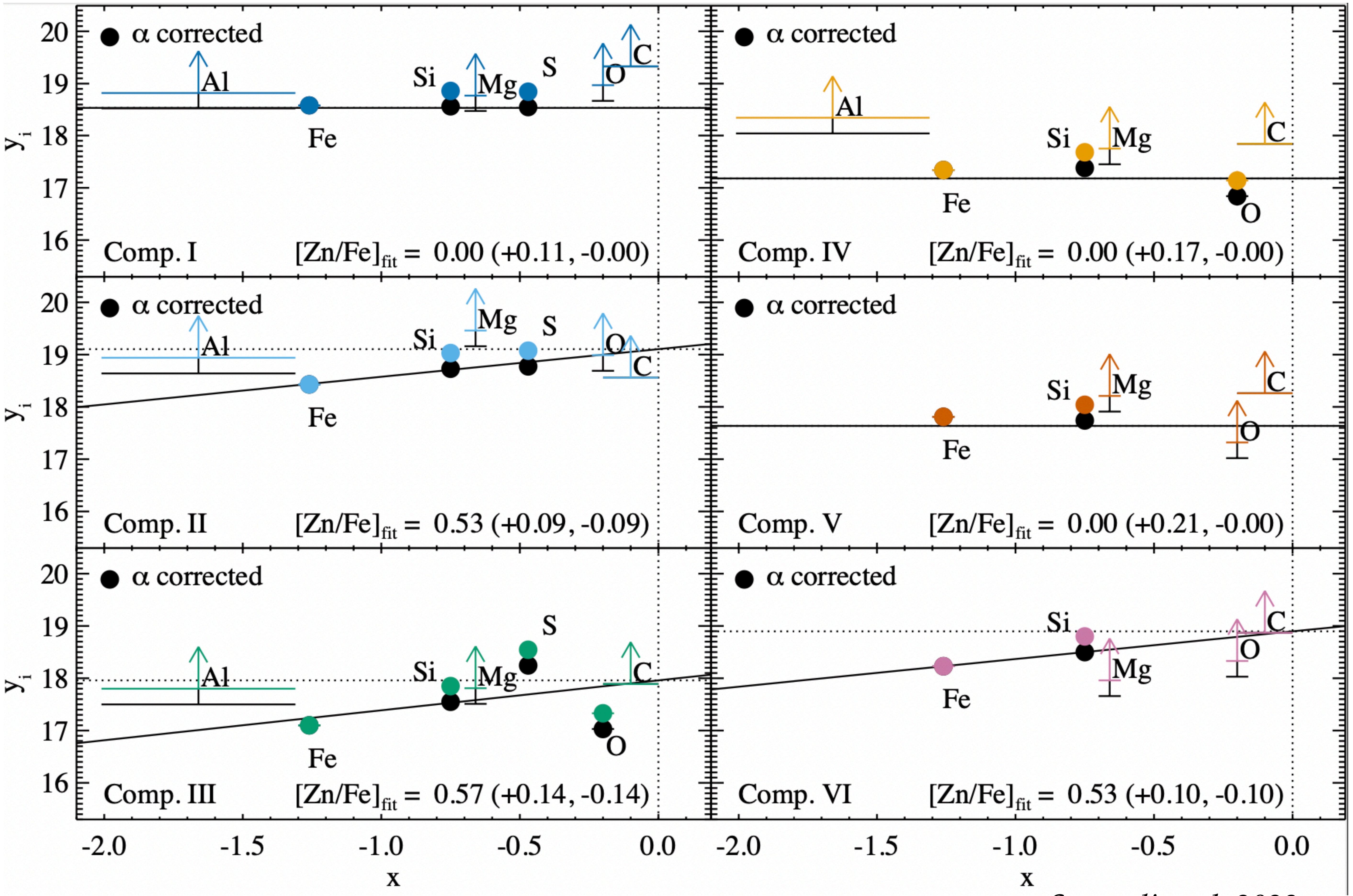

Saccardi et al. 2023

The case of GRB 210905A at z = 6.312

RESULTS

-We find that the dust-corrected metallicity of the GRB host is [M/H] = -1.72 +/- 0.13 and DTM = 0.18 +/- 0.03

-We determine the total abundance pattern and for each component: the abundance ratios, $[X/Fe]_{nucl}$, are due to the effect of nucleosynthesis

Saccardi et al. 2023

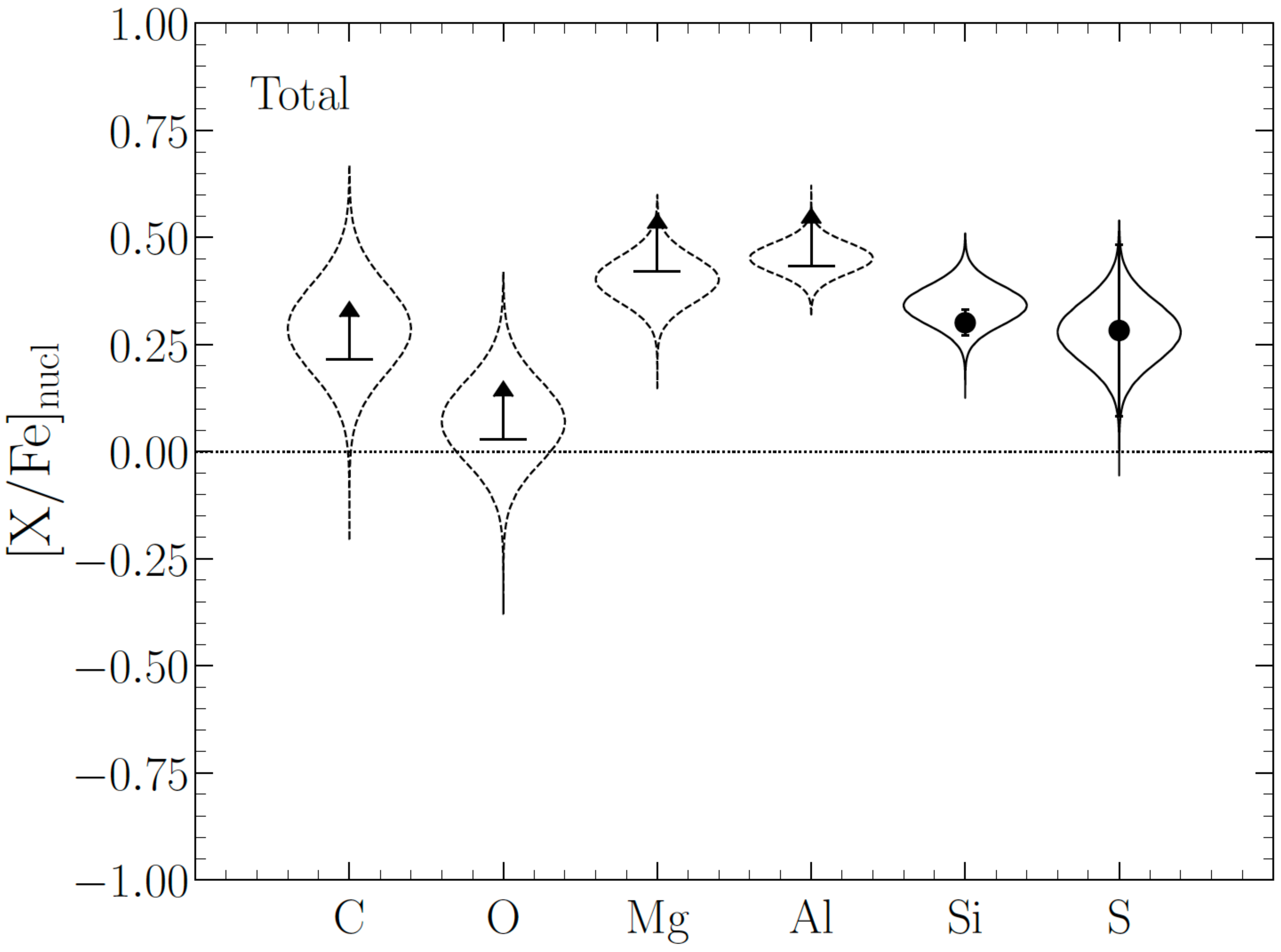

Saccardi et al. 2023

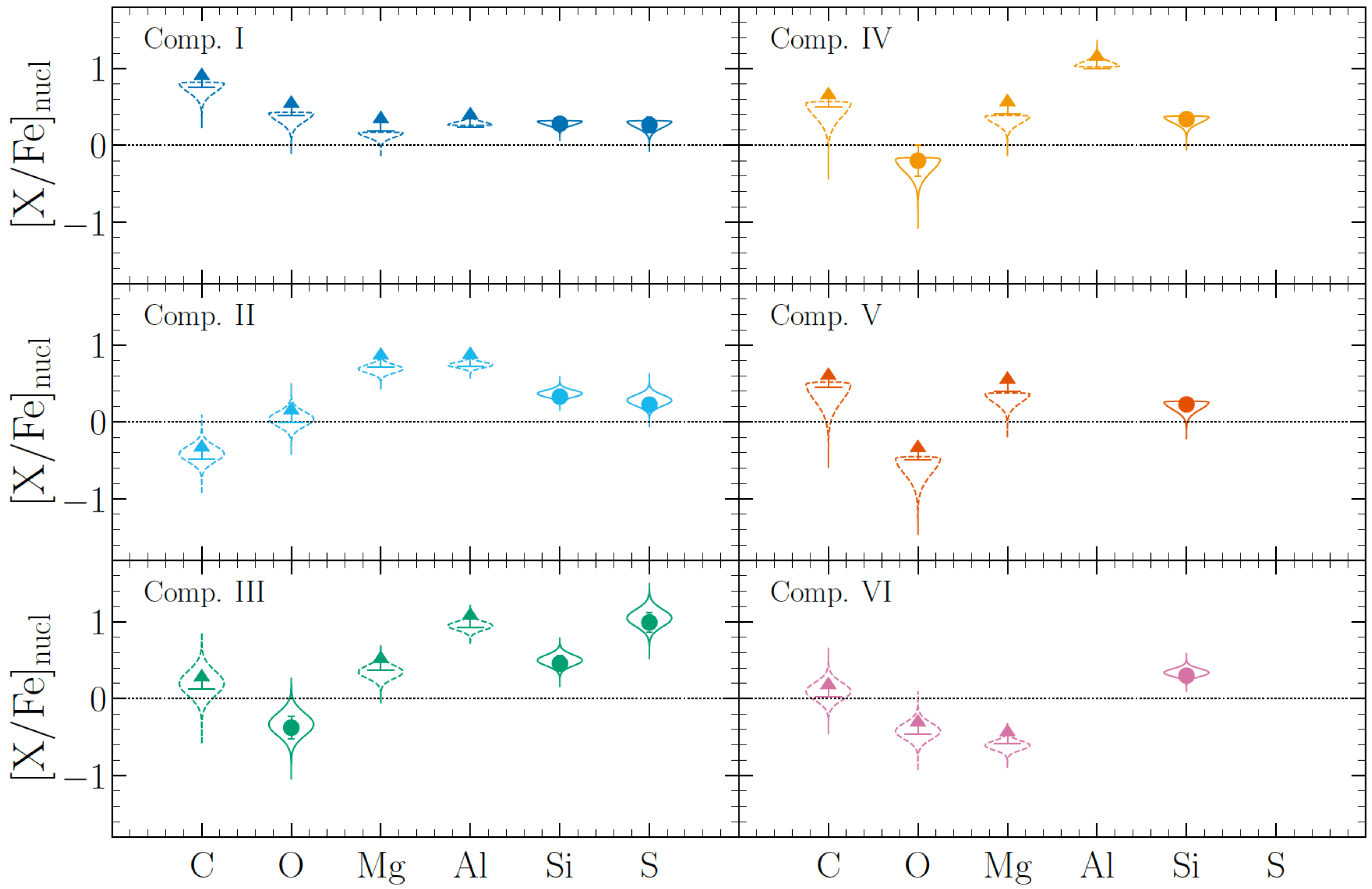

z = 6.782

Saccardi et al. sub.
Arxiv2506.04340

GRB 240218A

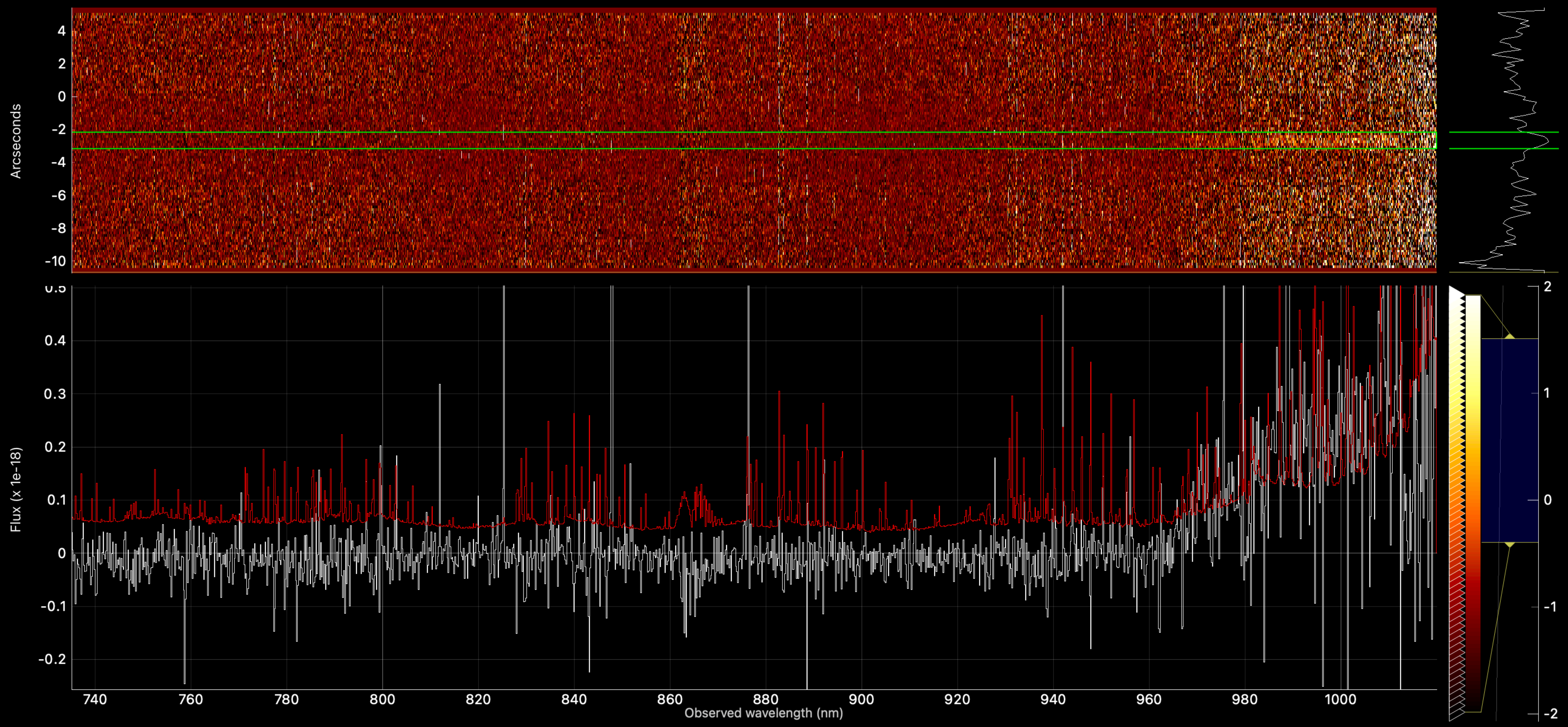

The case of GRB 240218A at z = 6.782

GRB240218A VLT/X-shooter Spectrum

Credits: Saccardi et al. arXiv:2506.04340

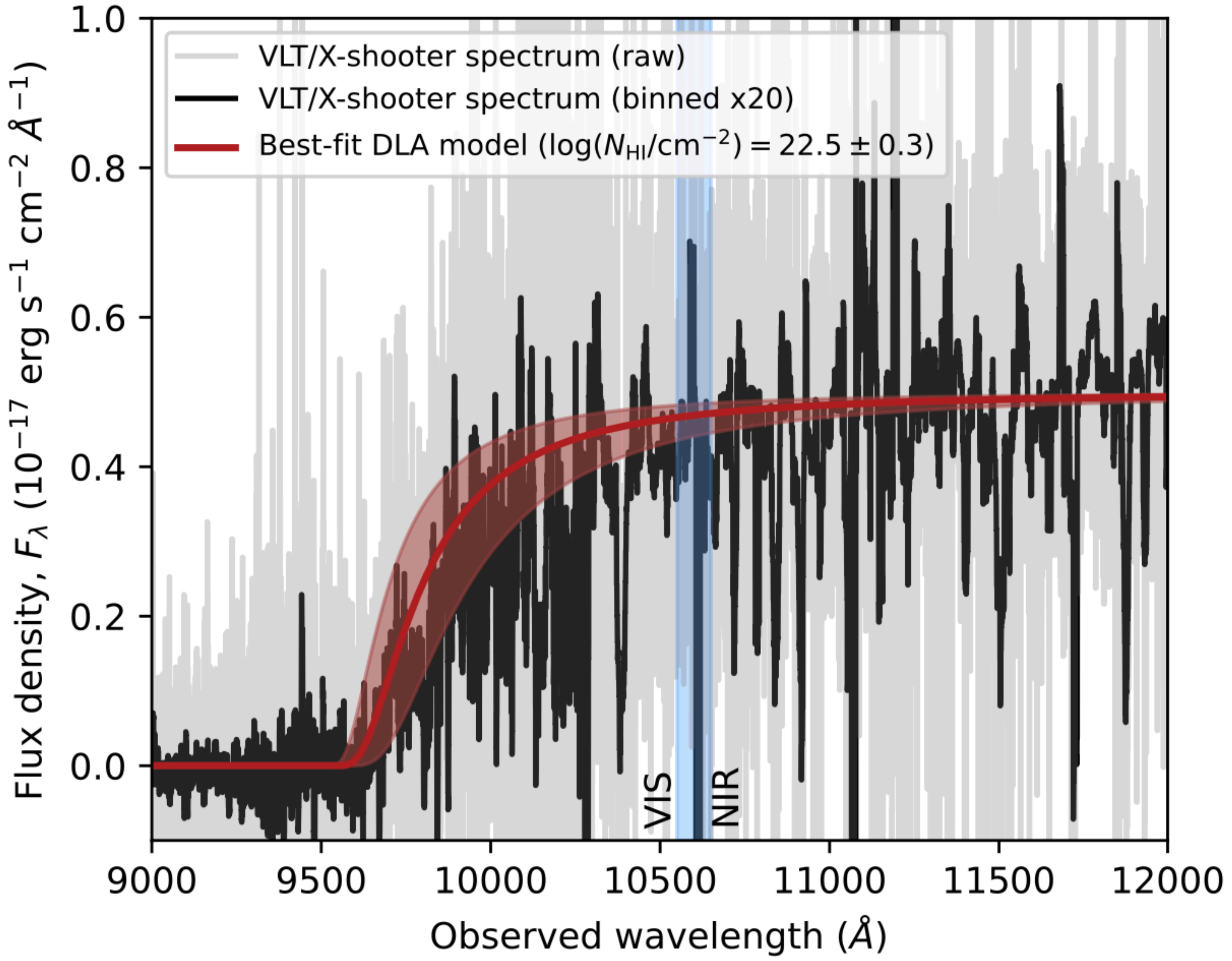

$\log(N_{HI}/cm^{-2}) = 22.5 +/- 0.3$

—-> The highest neutral hydrogen column density at high redshift!

Credits: Saccardi et al. arXiv:2506.04340

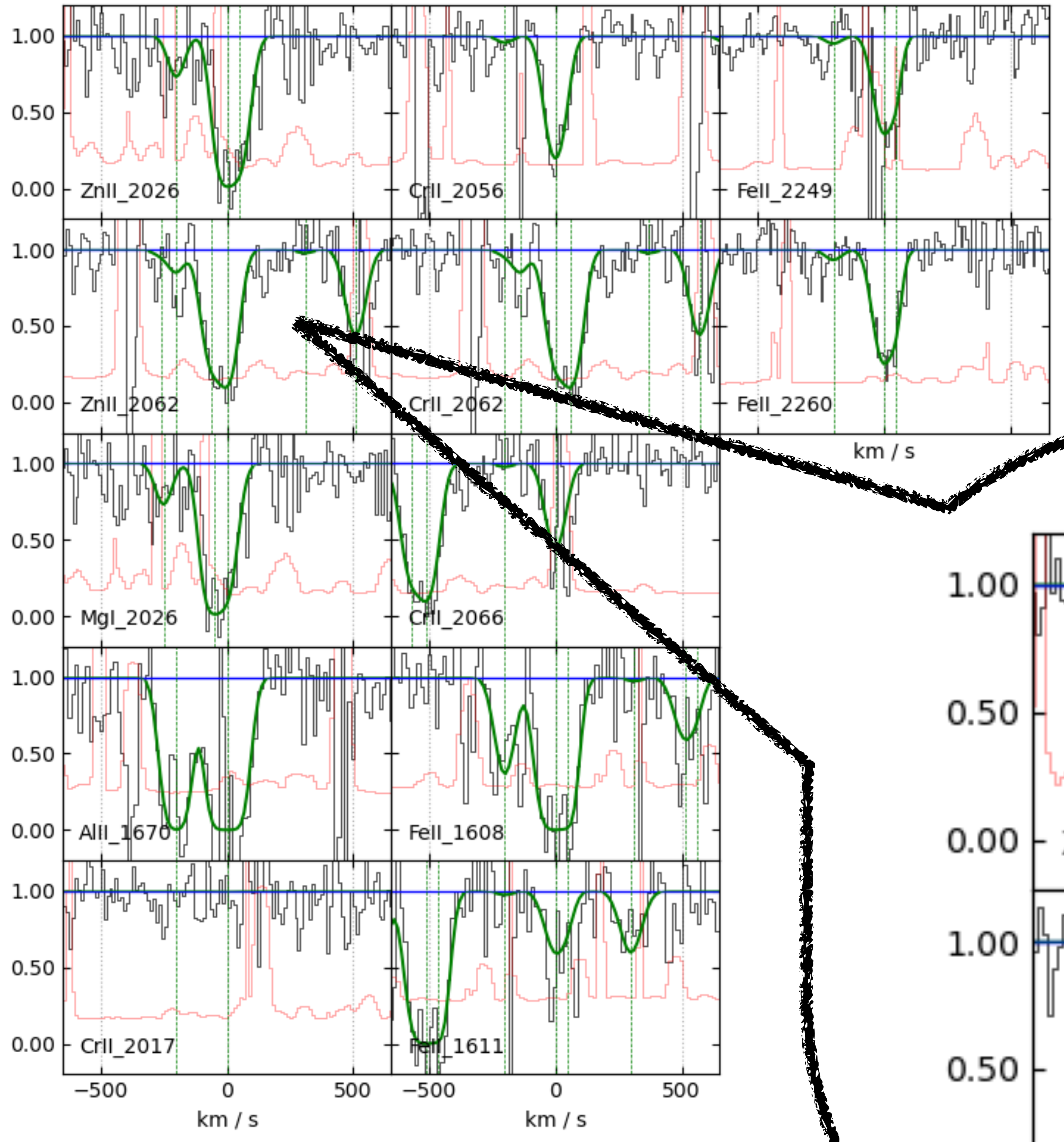

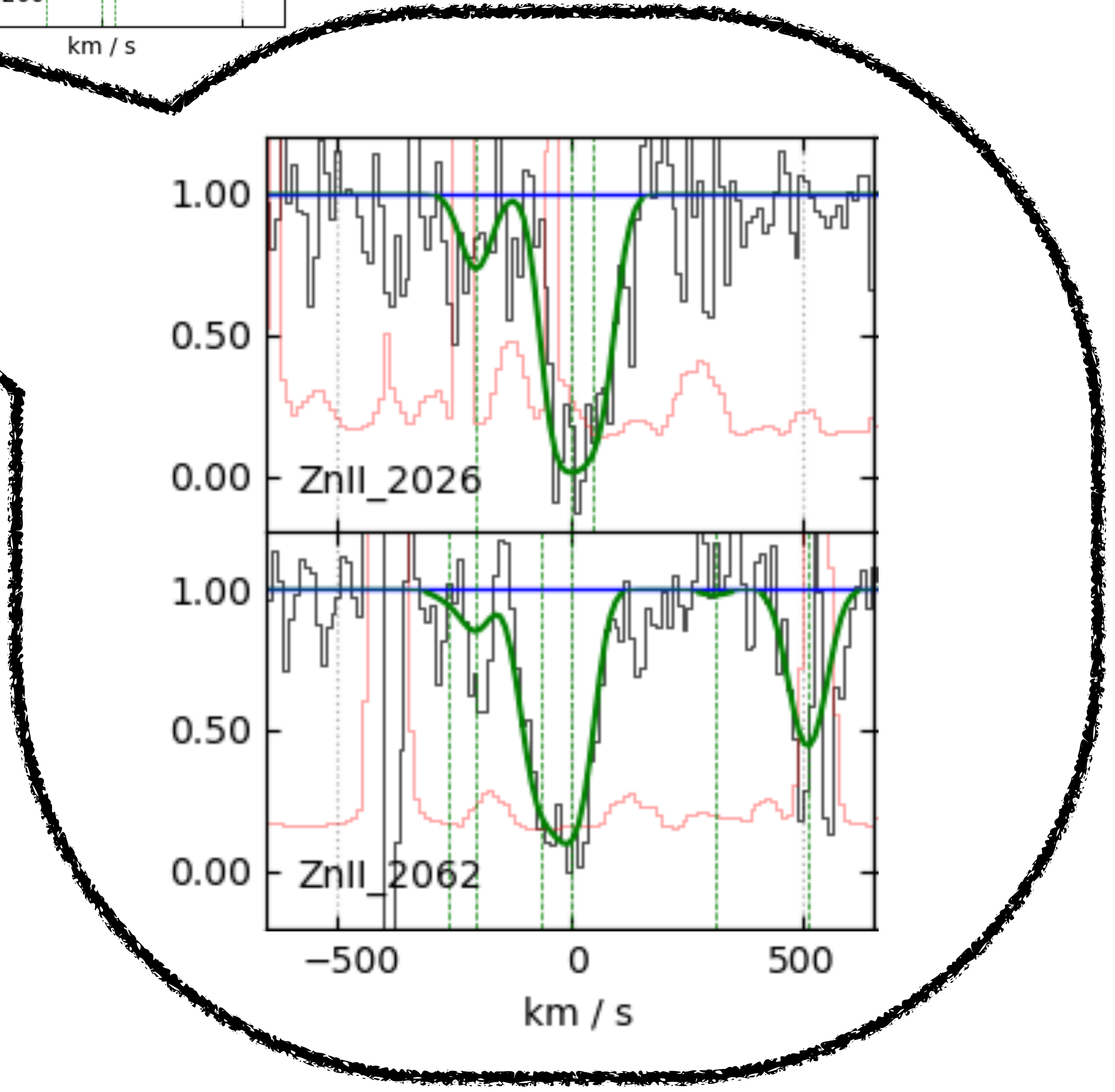

After ~26.47hr (obs frame)

—-> Large EWs!

$[Zn/H]_{obs} > -0.8$

$[Zn/Fe]_{obs} > 0.8$

—-> Significant presence of metals and dust at high redshift !

The case of GRB 240218A at z = 6.782

Credits: Saccardi et al. arXiv:2506.04340

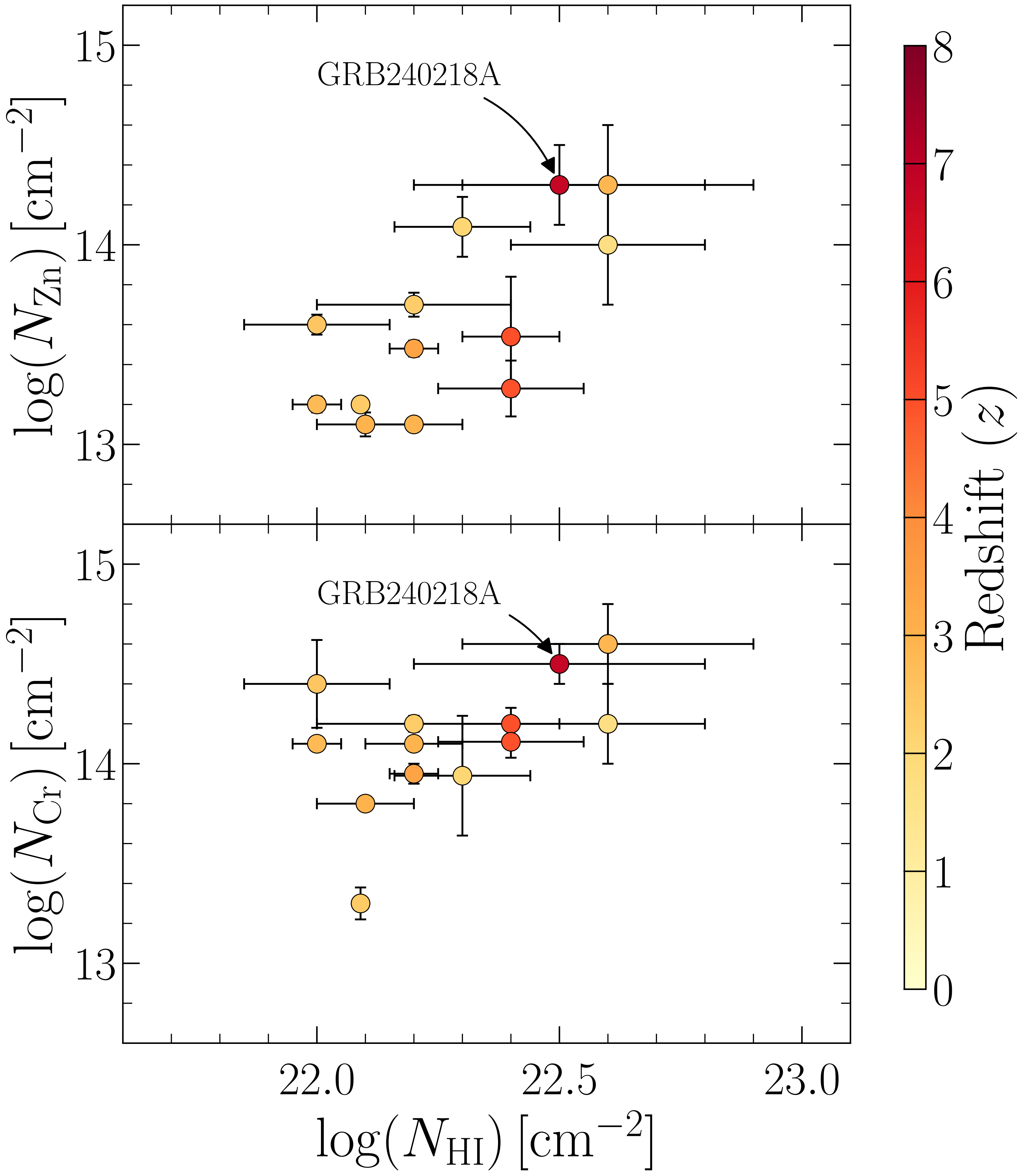

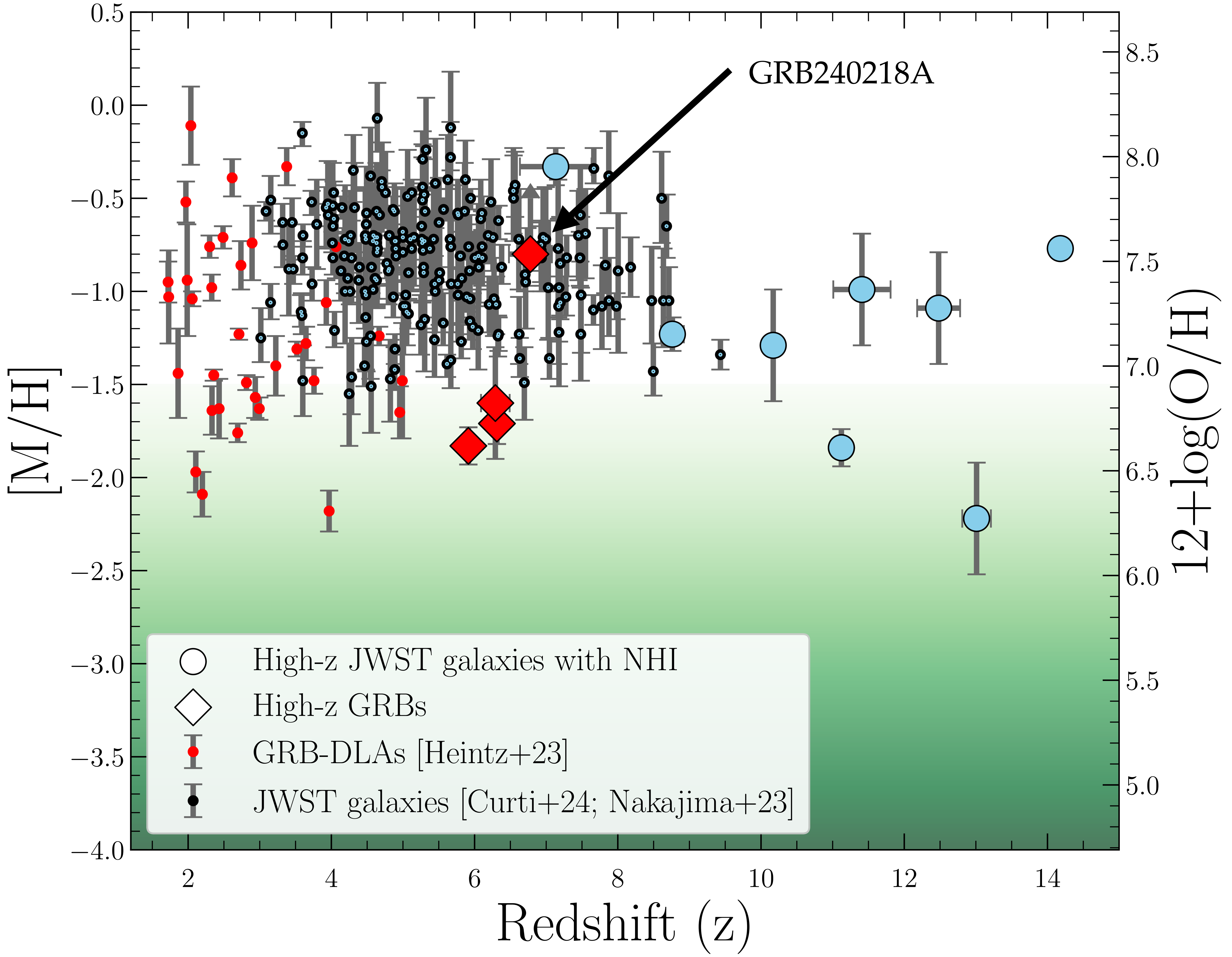

Nearby and Future Perspectives

Adapted from Saccardi et al. 2023

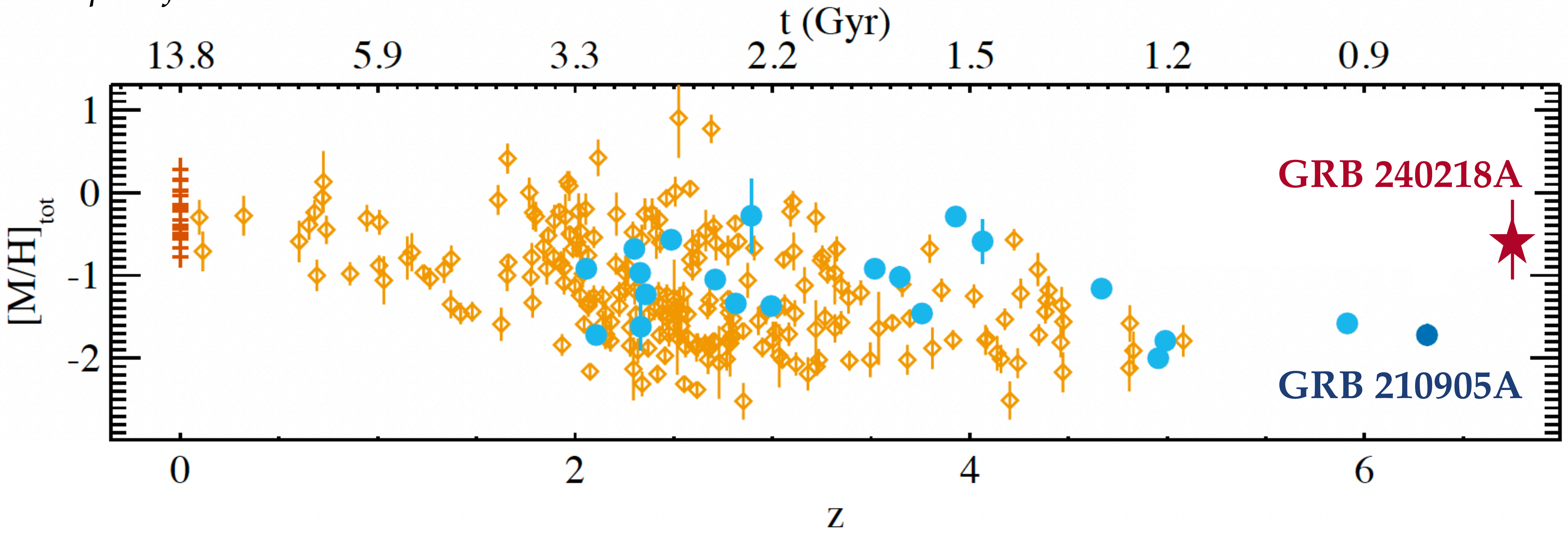

Thanks to GRB afterglow spectroscopy we can reach the high redshift Universe and populate the reionization era (i.e. z>6)

Credits: Ghirlanda et al. 2015

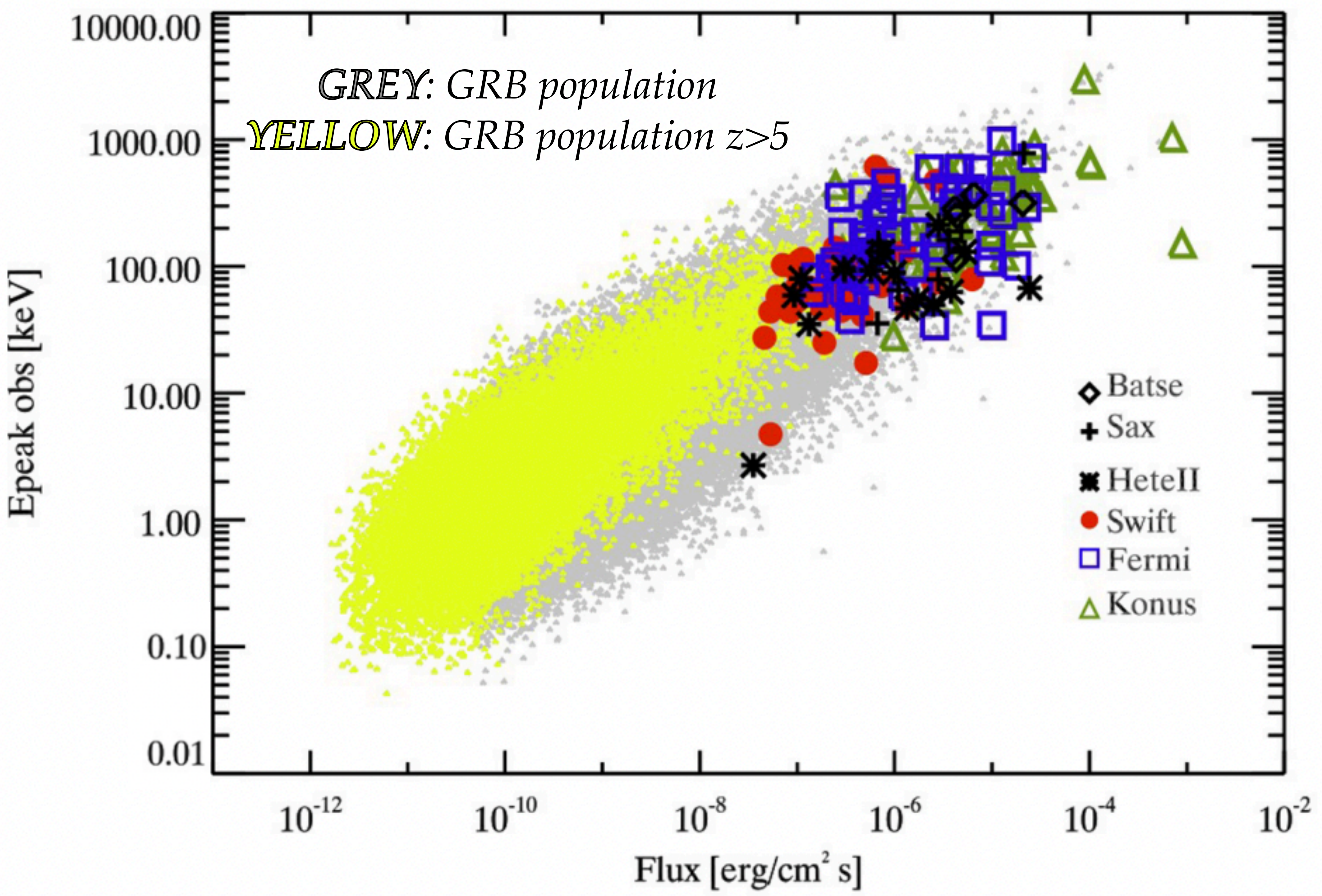

Limitations

(i) poor fraction of GRBs with an optical/NIR afterglow spectrum(20-30%)

(ii) lack of satellites capability to detect high-redshift GRBs

SVOM

SVOM

GOAL: boost to 50/60% the fraction of GRBs with redshift determination and enhance the number of high-z GRBs

-An **energy threshold** of γ-ray detector at 4 keV may enable the detection of **faint soft GRBs** (e.g. high-redshift GRBs)

-**Good sensitivity of the on-board optical telescope:**

(i) detect and localize GRB afterglow
(ii) rapid pinpoint to high-z candidates (r~22.5 (AB) in 300s)

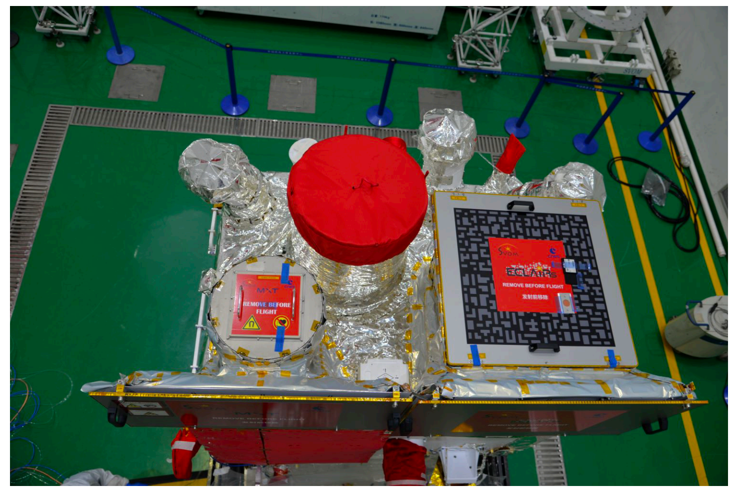

Credits: SVOM

How?

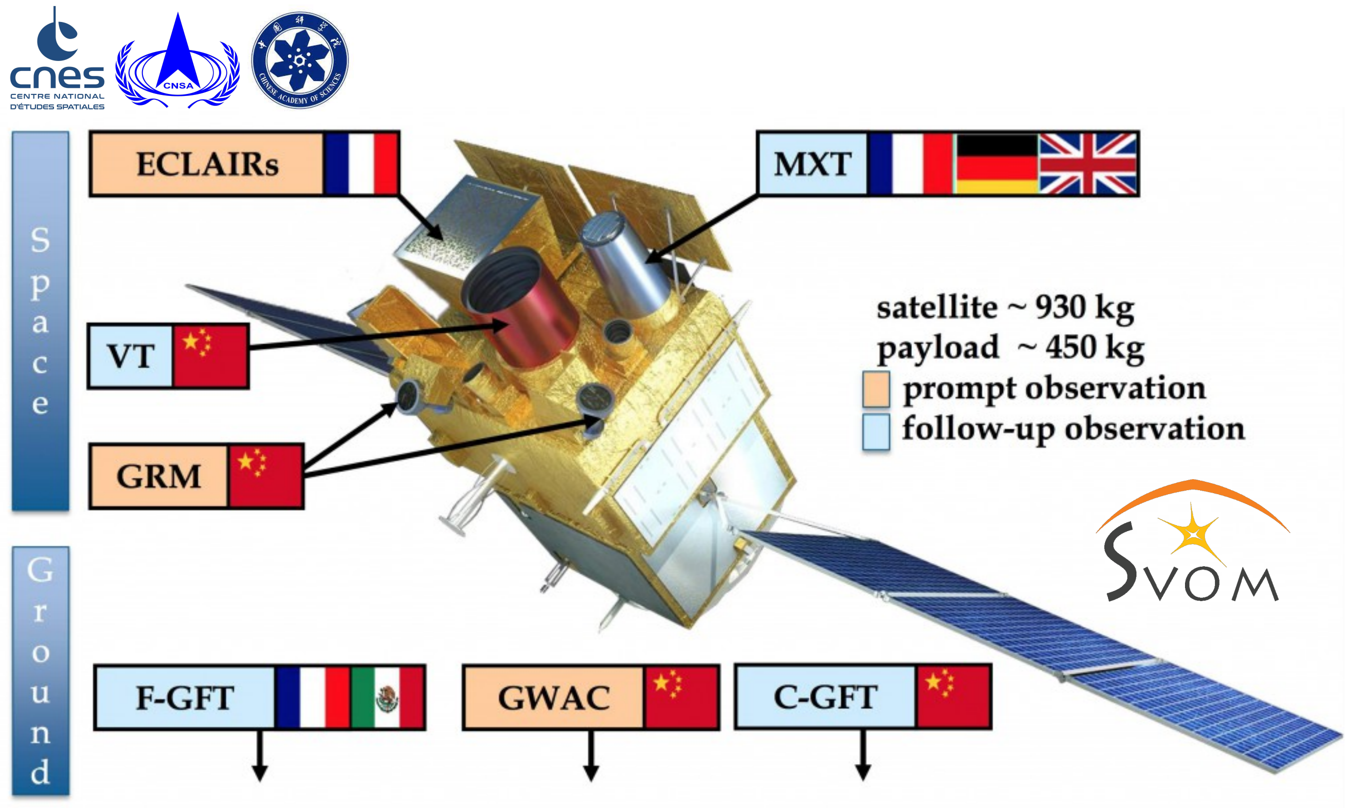

Credits: SVOM

-A near anti-solar pointing ensuring that **SVOM GRBs are observable from earth**

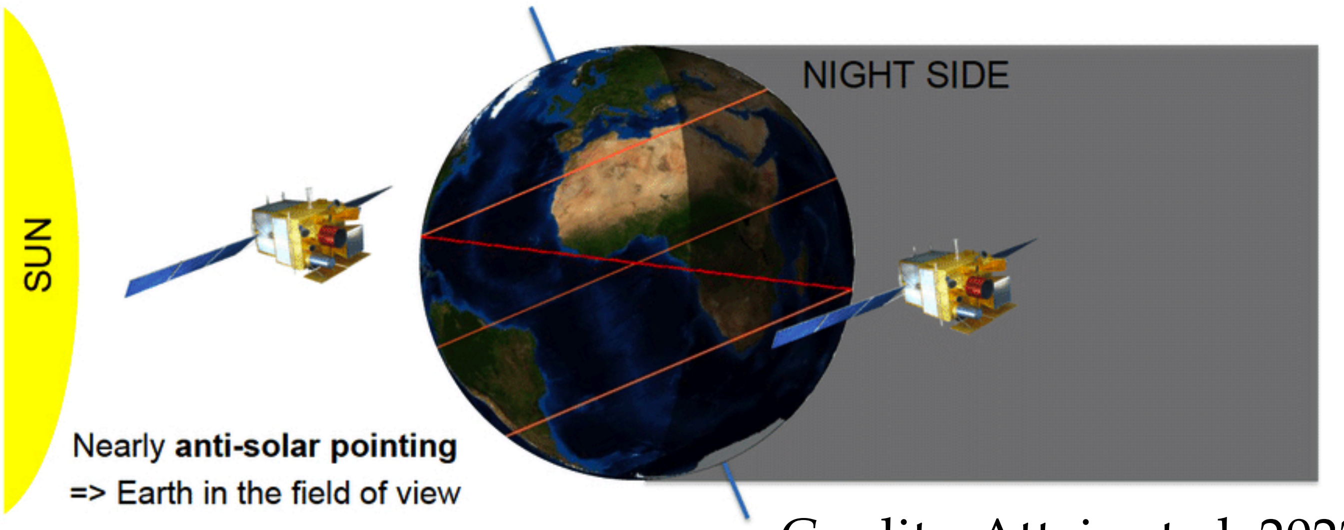

Credits: Atteia et al. 2022, SVOM

Credits: COLIBRI&A. Watson, UNAM

-SVOM F-GFT

localization < 1″
mirror of 1.3 m
FoV of 26′ ×26′
400nm to 1800 nm
r = 22 mag in 300 s

-Dedicated **NIR follow-up on the ground:** i.e. ground based telescopes (SVOM/F-GFT) COLIBRI

-Agreements to obtain the **spectroscopic observations of SVOM-GRB** with large ground-based telescope

Long term Perspectives

THESEUS

Selected for
ESA M7
Phase-A

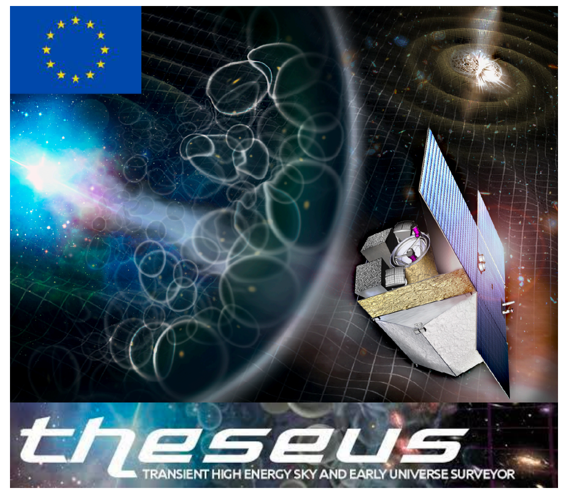

http://www.isdc.unige.ch/theseus

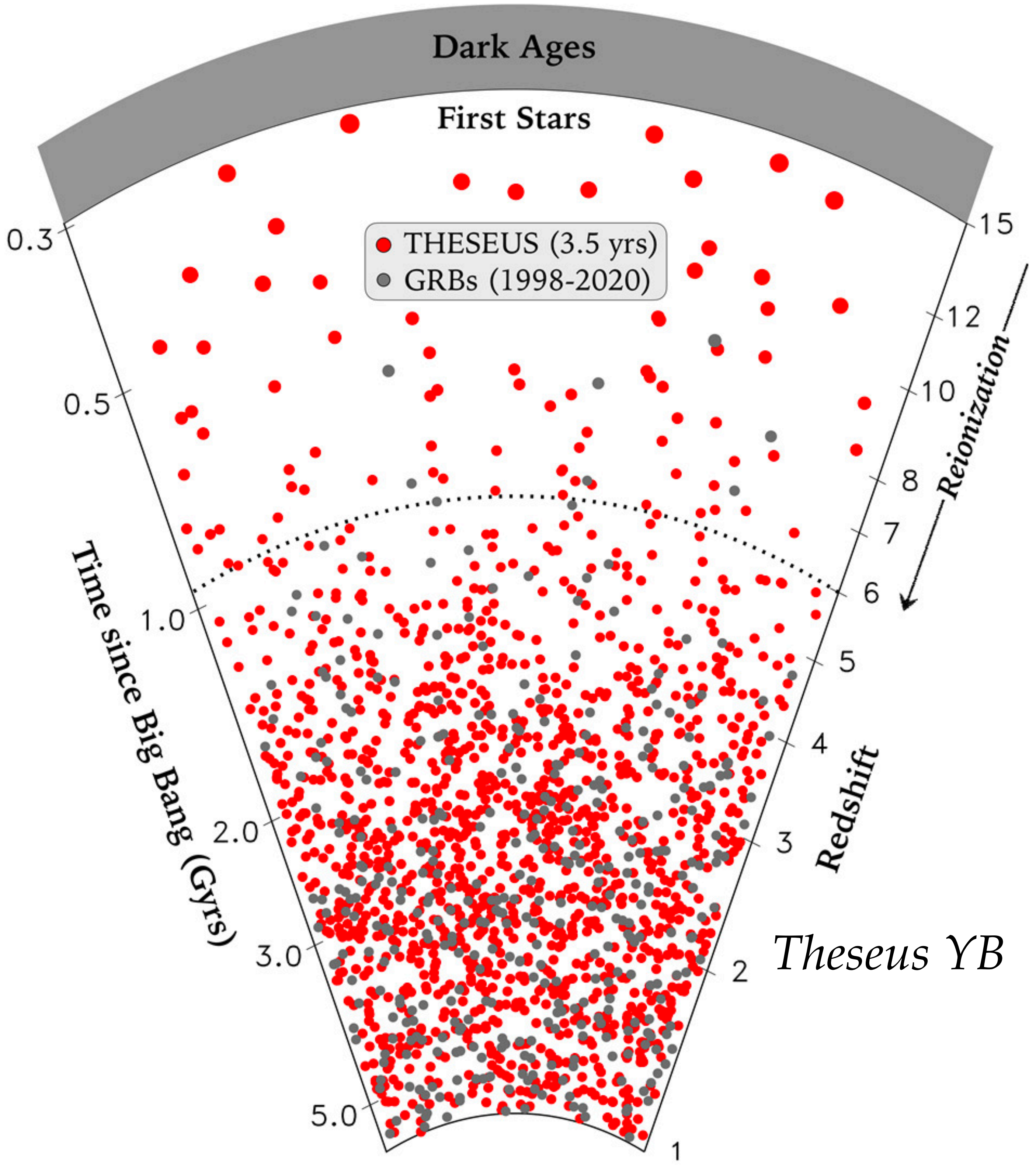

THESEUS Payload
-Soft X-ray Imager
(SXI, 0.3 – 5 keV)

-X-Gamma rays
Imaging Spectrometer
(XGIS, 2 keV – 10 MeV)

-InfraRed Telescope
(IRT, 0.7 – 1.8 μm)

(i) X-ray large FoV (0.5 sr)
(ii) precise source localization (0.5 to 2 arc-min)
(iii) low resolution spectroscopy on-board (R~400)

ANDES

Marconi et al. 2024

-Three fibre-fed spectrographs (UBV, RIZ, YJH)
-Spectral resolution of R~100,000
-Simultaneous wavelength coverage of 0.4-1.8 μm
-Goal of extending to 0.35-2.4 μm
(K band spectrograph)

WG3

Galaxy Formation and Evolution and the Inter-Galactic Medium

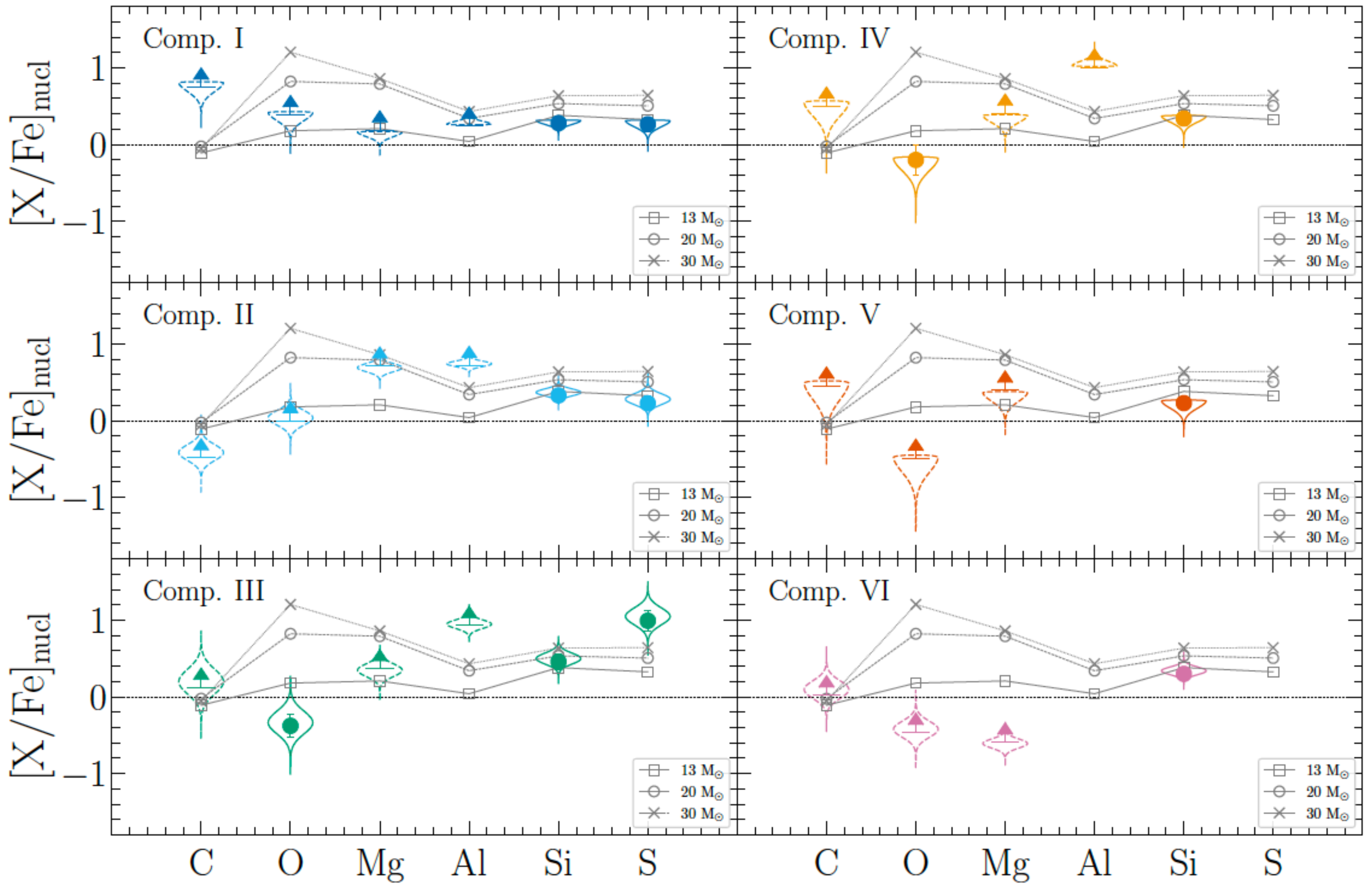

ANDES White Book
(D'Odorico et al. 2024 submitted)
Adapted from Saccardi et al. 2023a

(i) reach the SNR levels needed to study the faint high-z sources

(ii) resolve narrow absorption lines

(iii) constrain key elements column density

(iv) study relative abundances in individual gas components

ANDREA SACCARDI
CNES Postdoctoral Fellow
@CEA/Irfu/DAp - AIM

-Unveiling galaxies at the highest redshifts and studying their chemical properties is a key objective in modern astrophysics

-Bright background sources are needed to study in detail the properties of the neutral gas

-GRBs are very powerful tools to probe the ISM of high-redshift galaxies and their metal and dust content

-Thanks to GRB 210905A and GRB 240218A we were able to obtain unique and detailed information of the neutral gas and its chemical composition

-The future is bright thanks to new space missions such as SVOM, Einstein Probe and hopefully THESEUS in synergy with ground-based observations (e.g. SOXS, ELT/ANDES)

Action Thématique des Phénomènes Extrêmes et Multi-Messagers

Backup Slides

Backup Slides

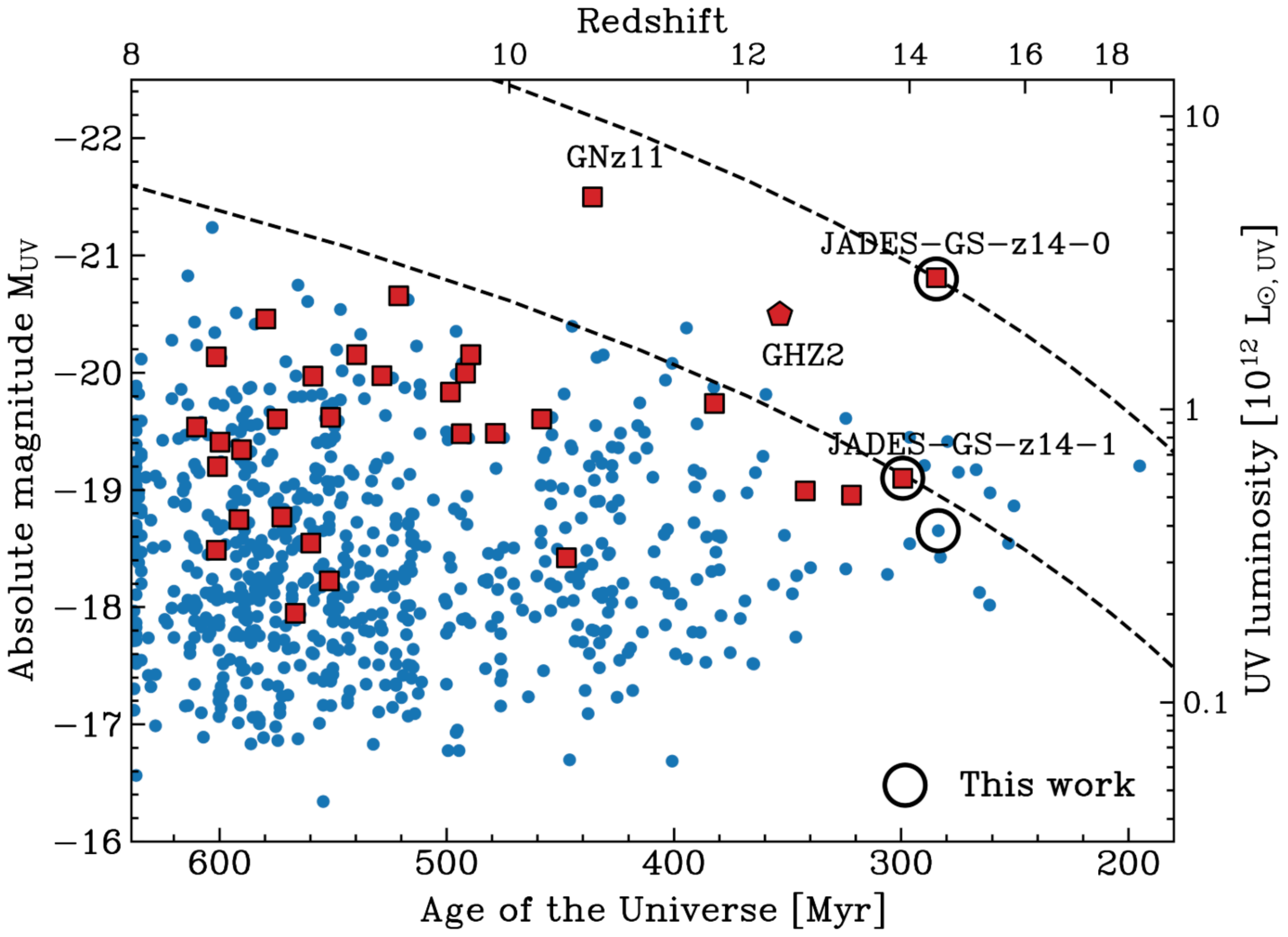

Credits: Carniani et al. 2024

Backup Slides

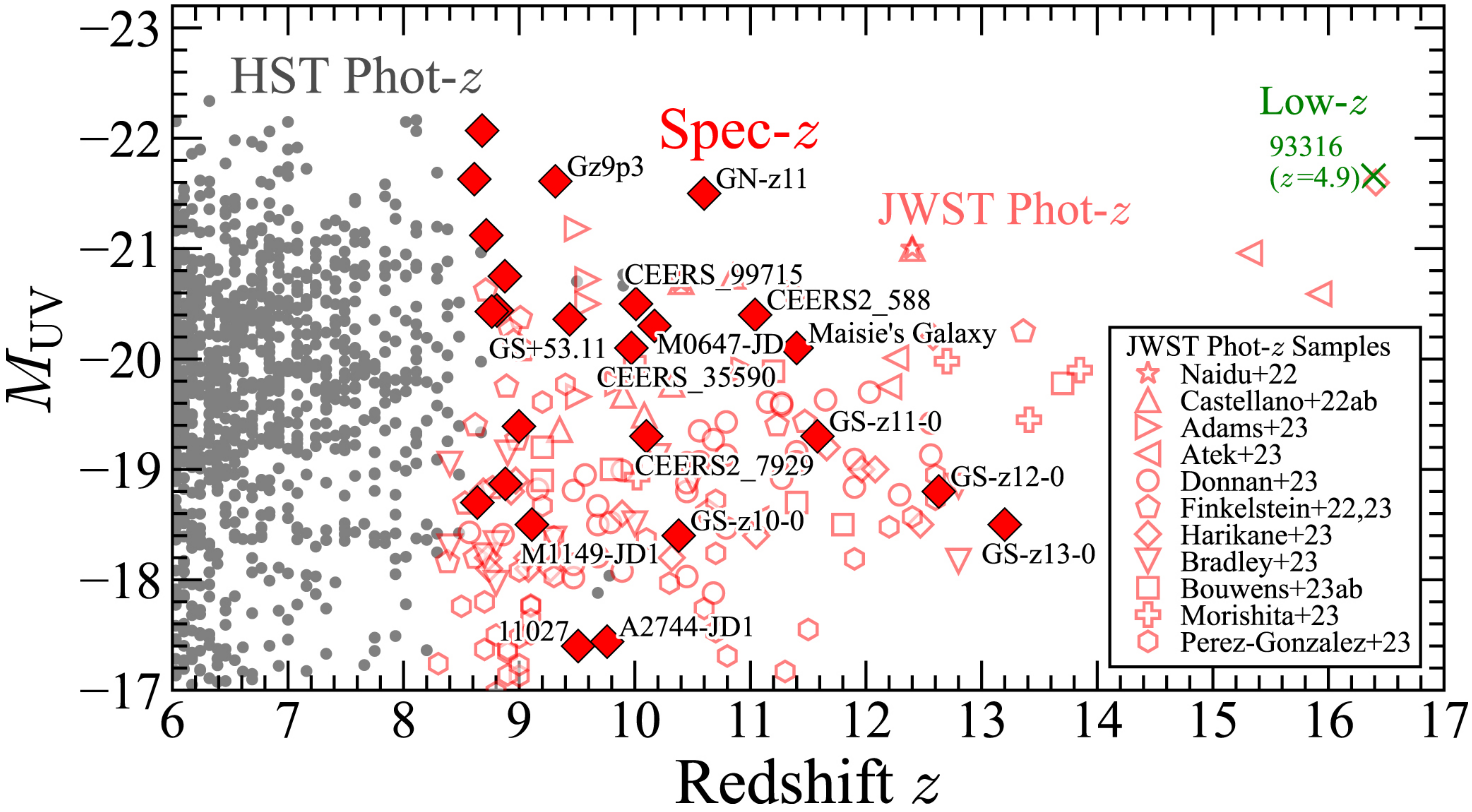

Credits: Harikane et al. 2024

Backup Slides

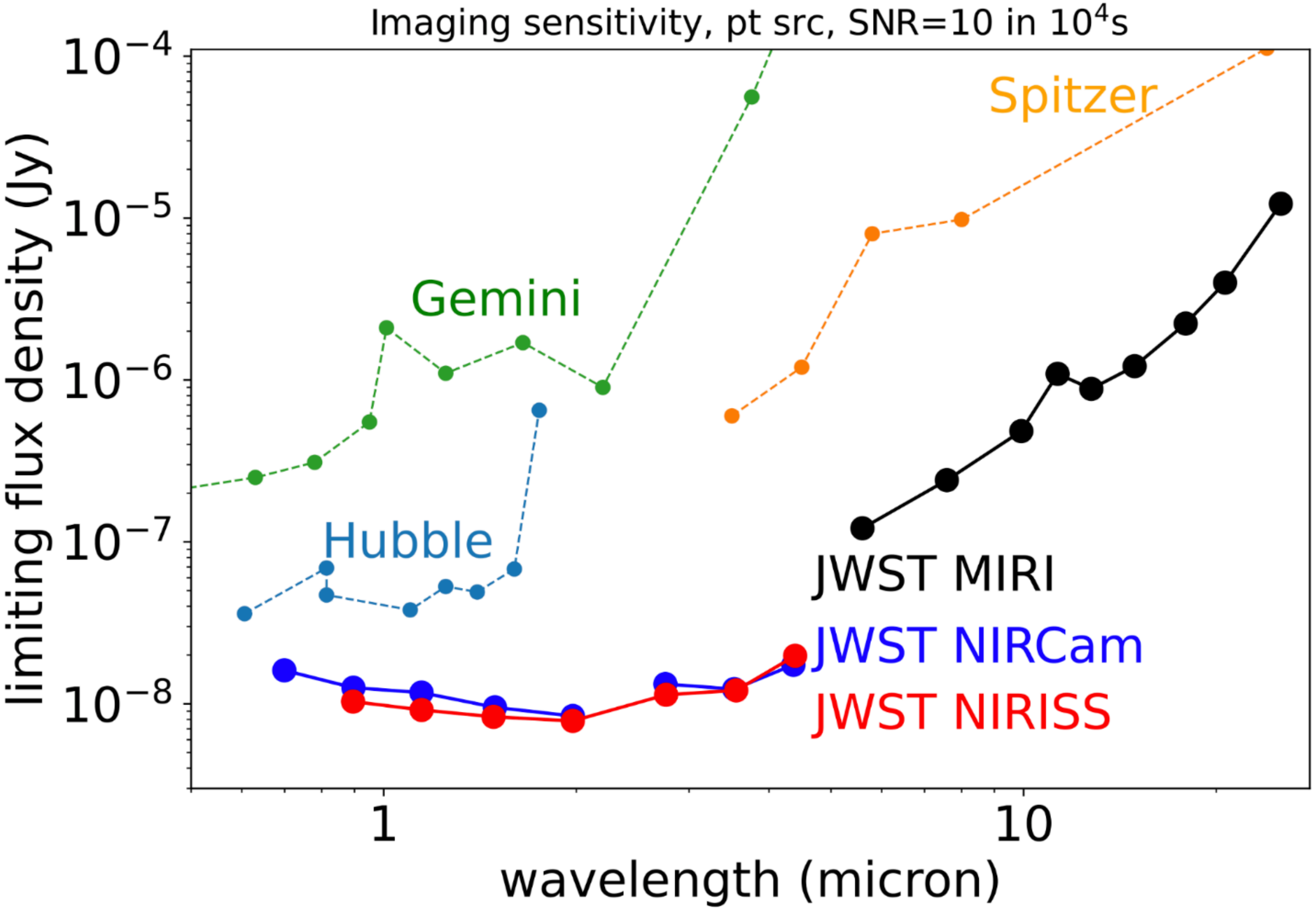

Credits: JWST Consortium

Backup Slides

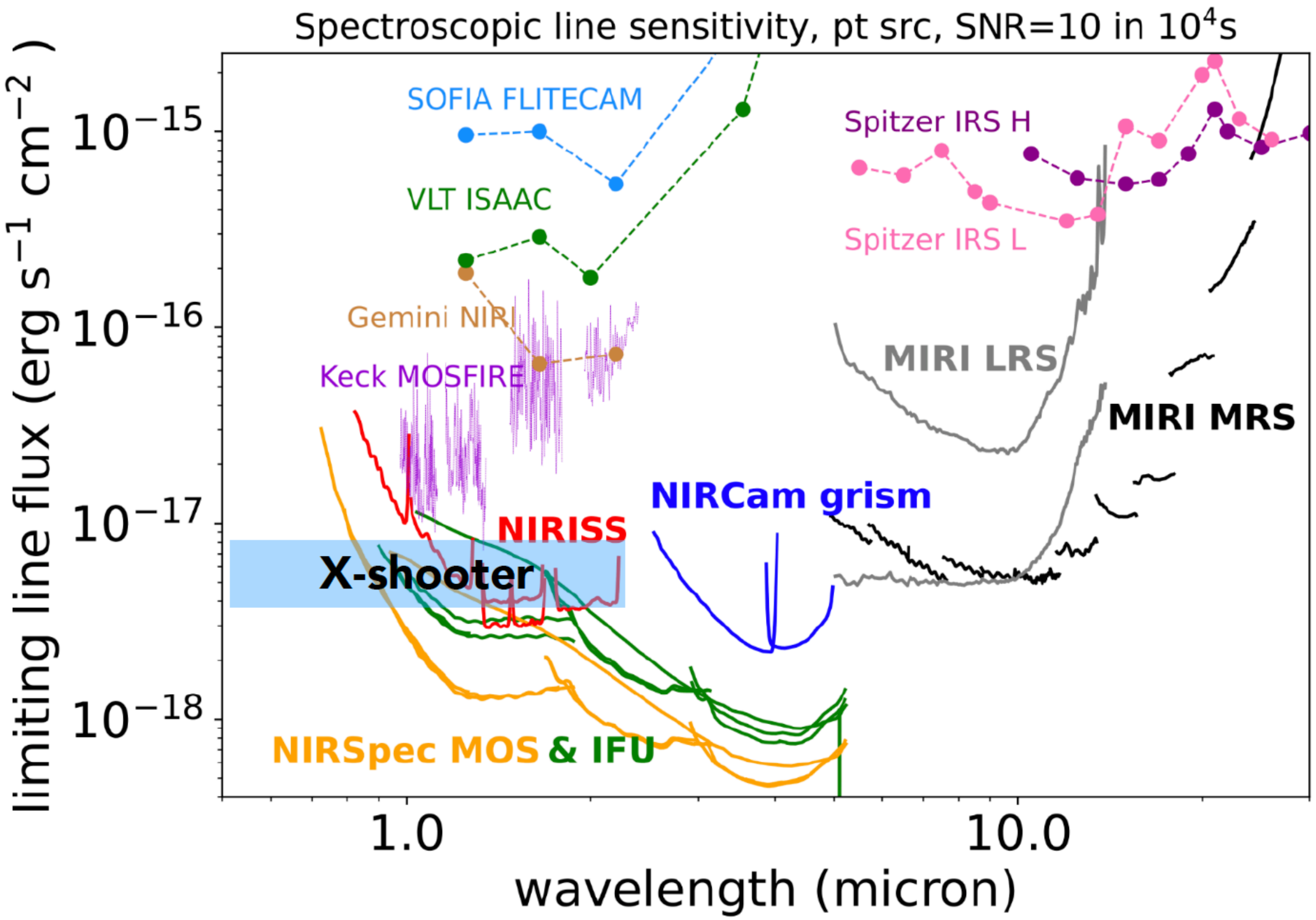

Credits: JWST Consortium

Backup Slides

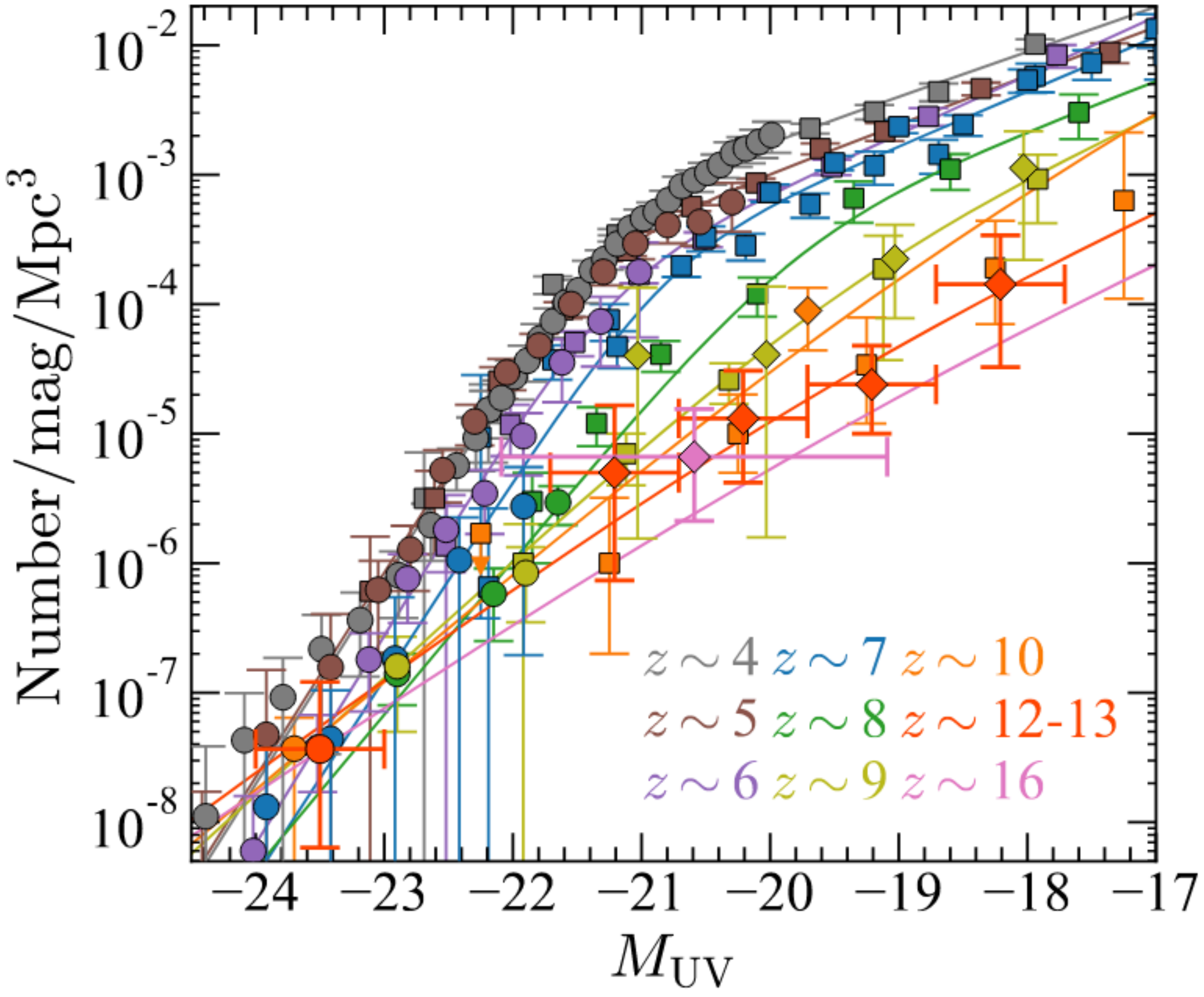

Credits: Harikane et al. 2022

Backup Slides

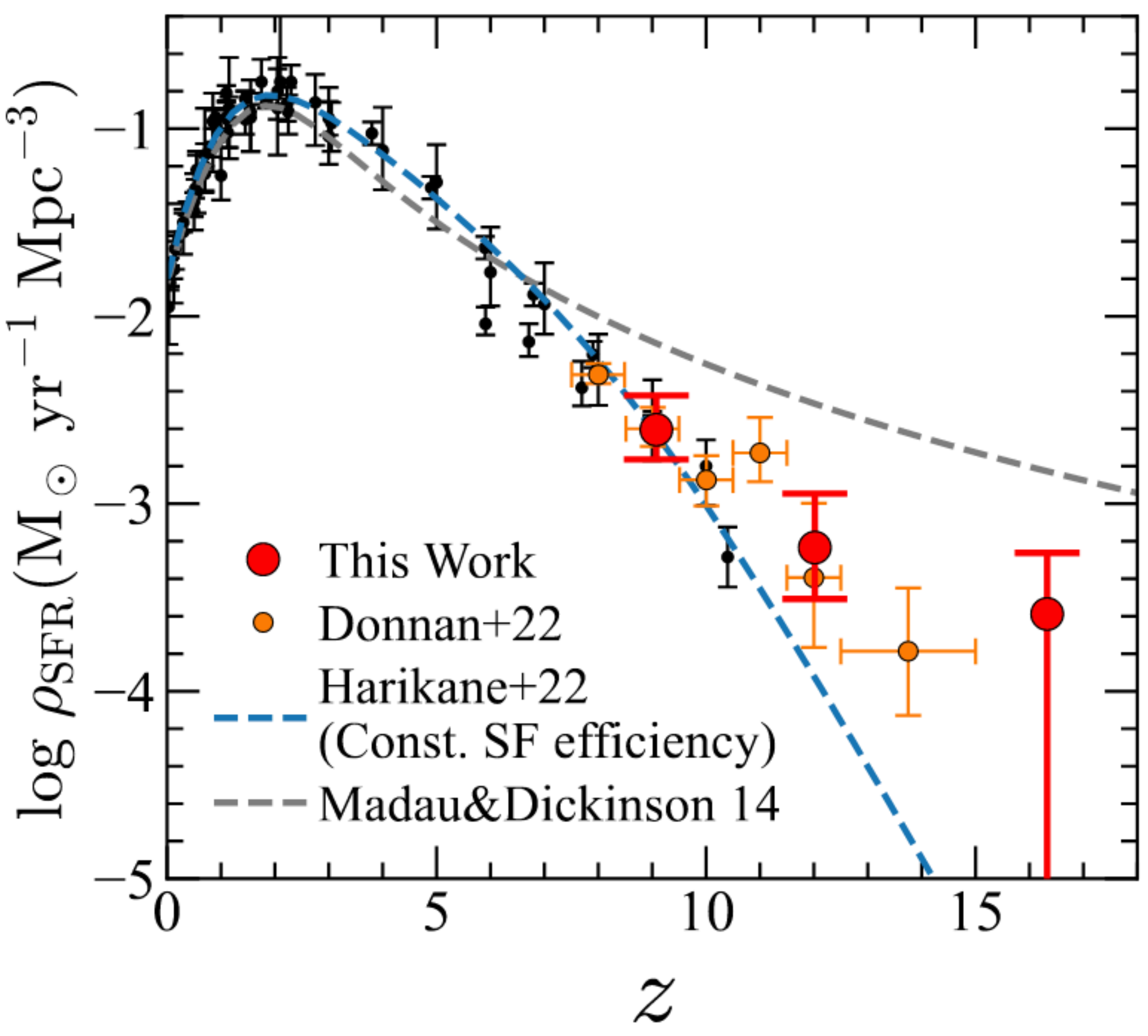

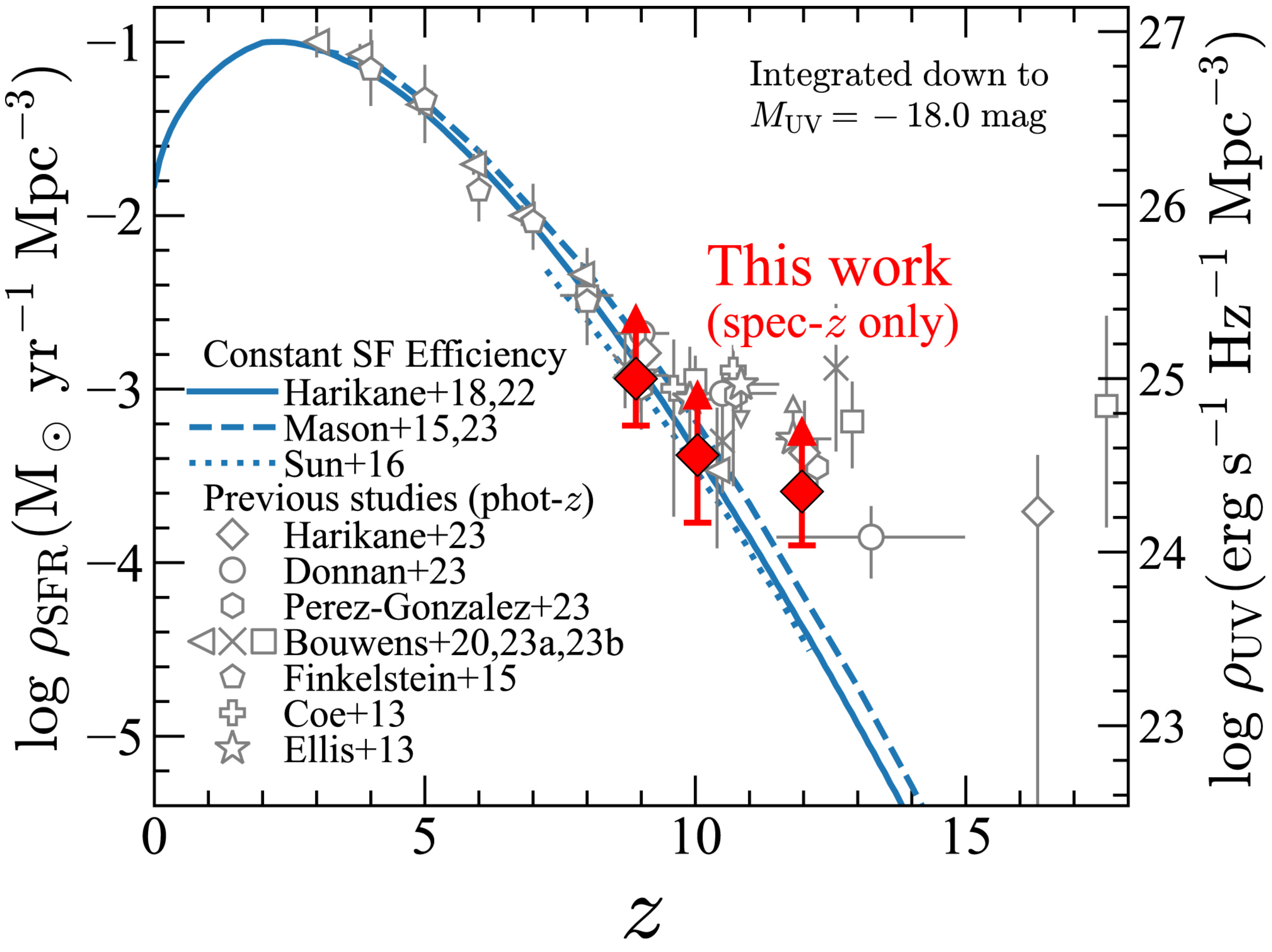

Credits: Harikane et al. 2022

Backup Slides

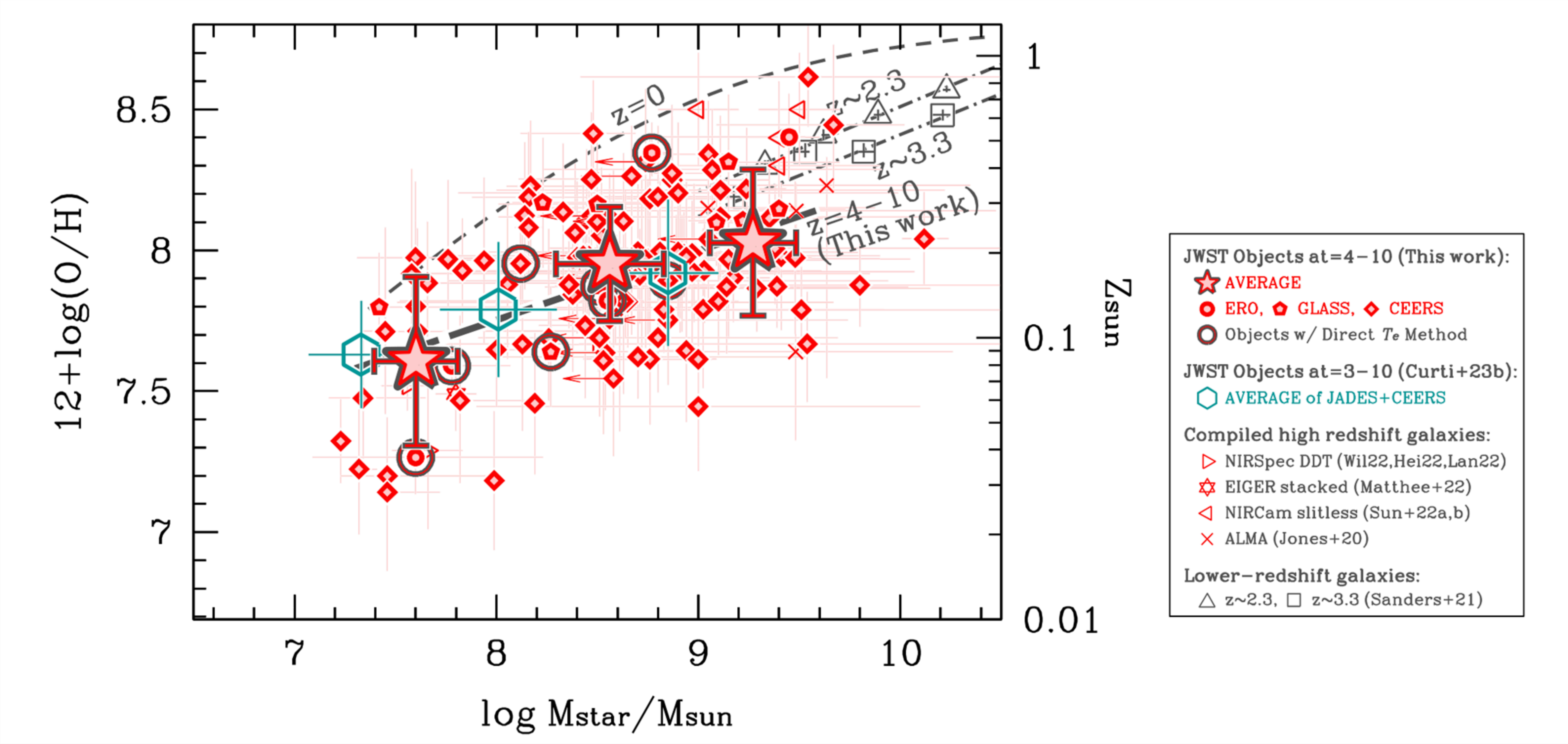

Backup Slides

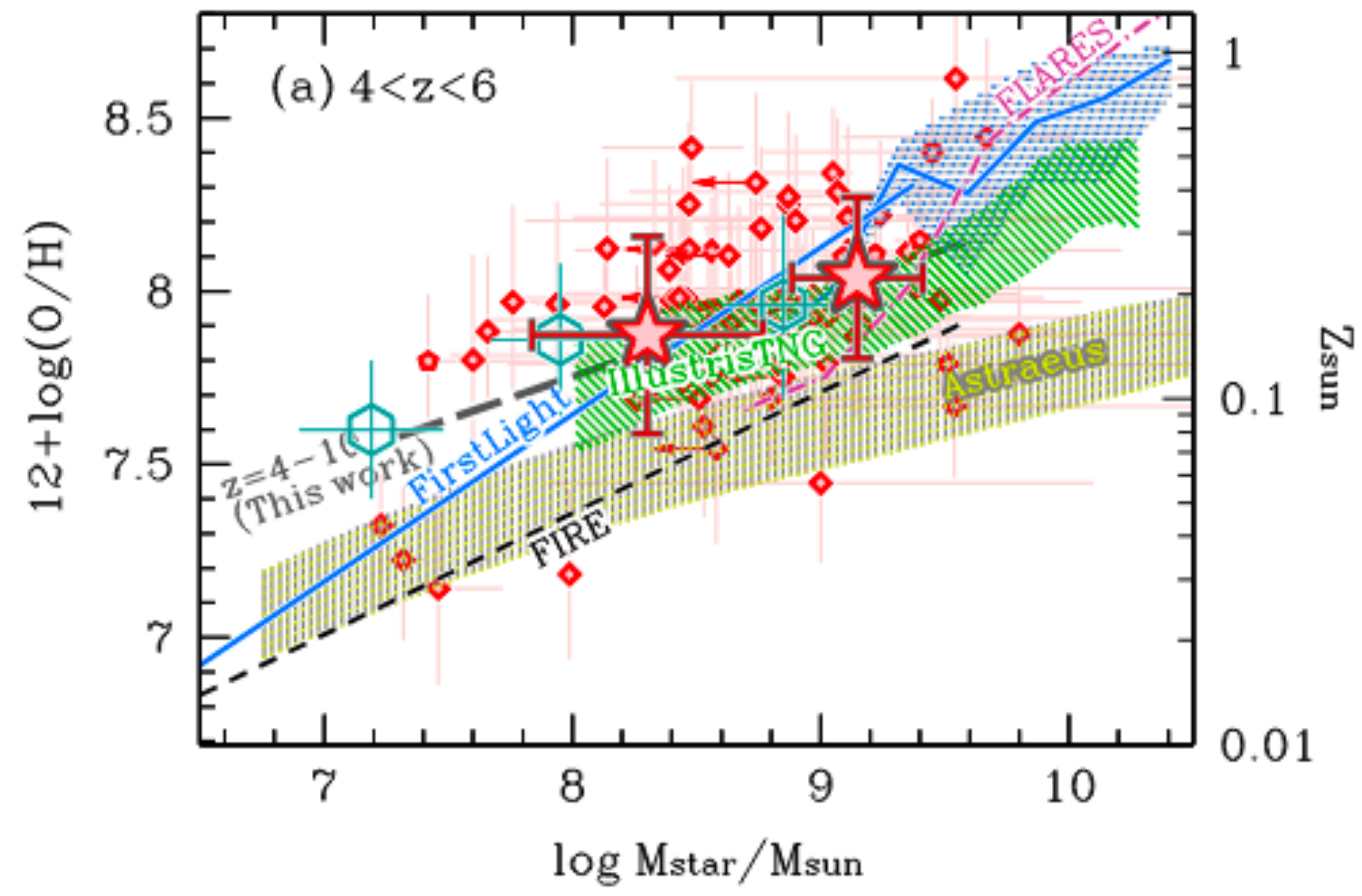

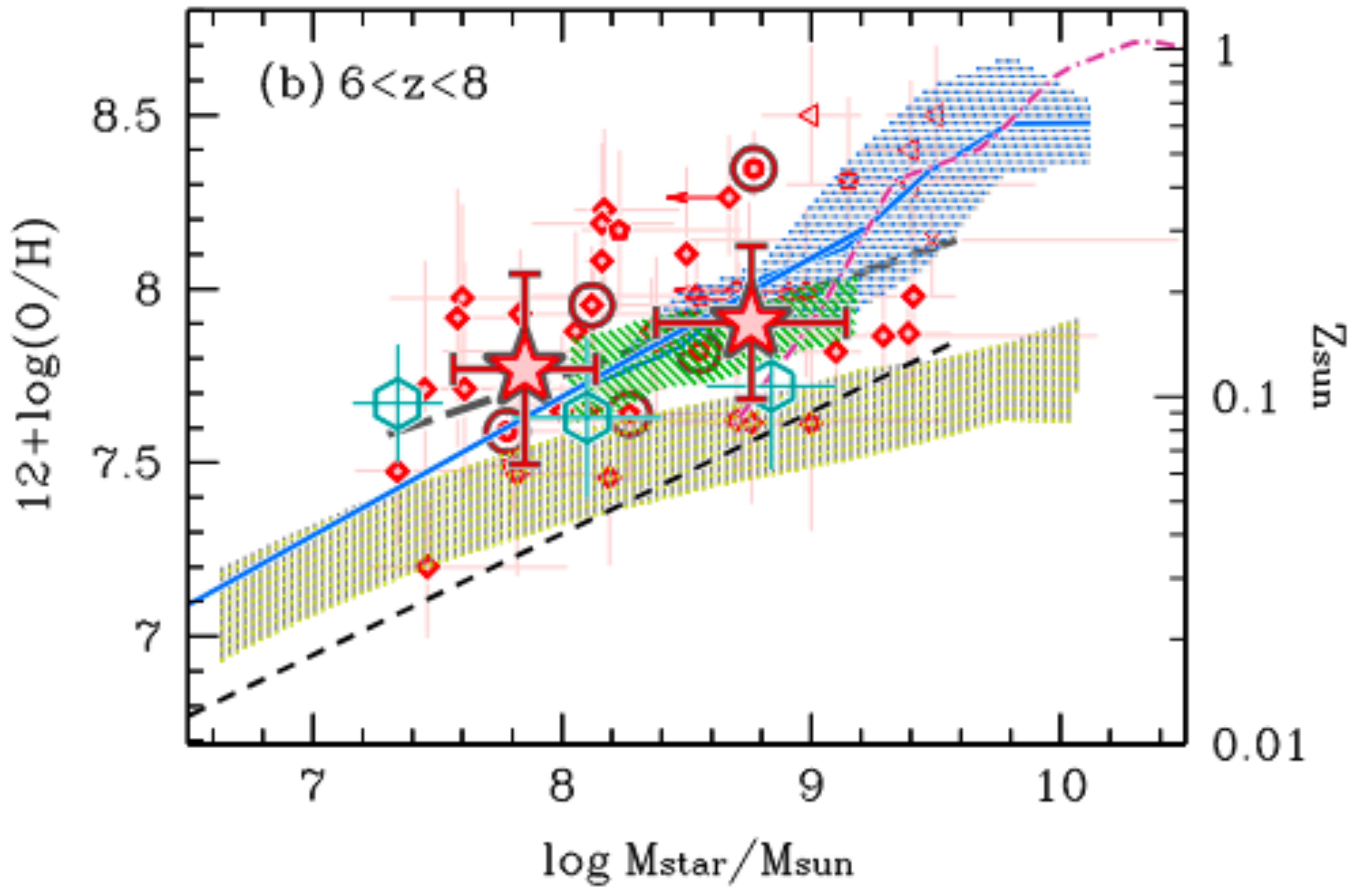

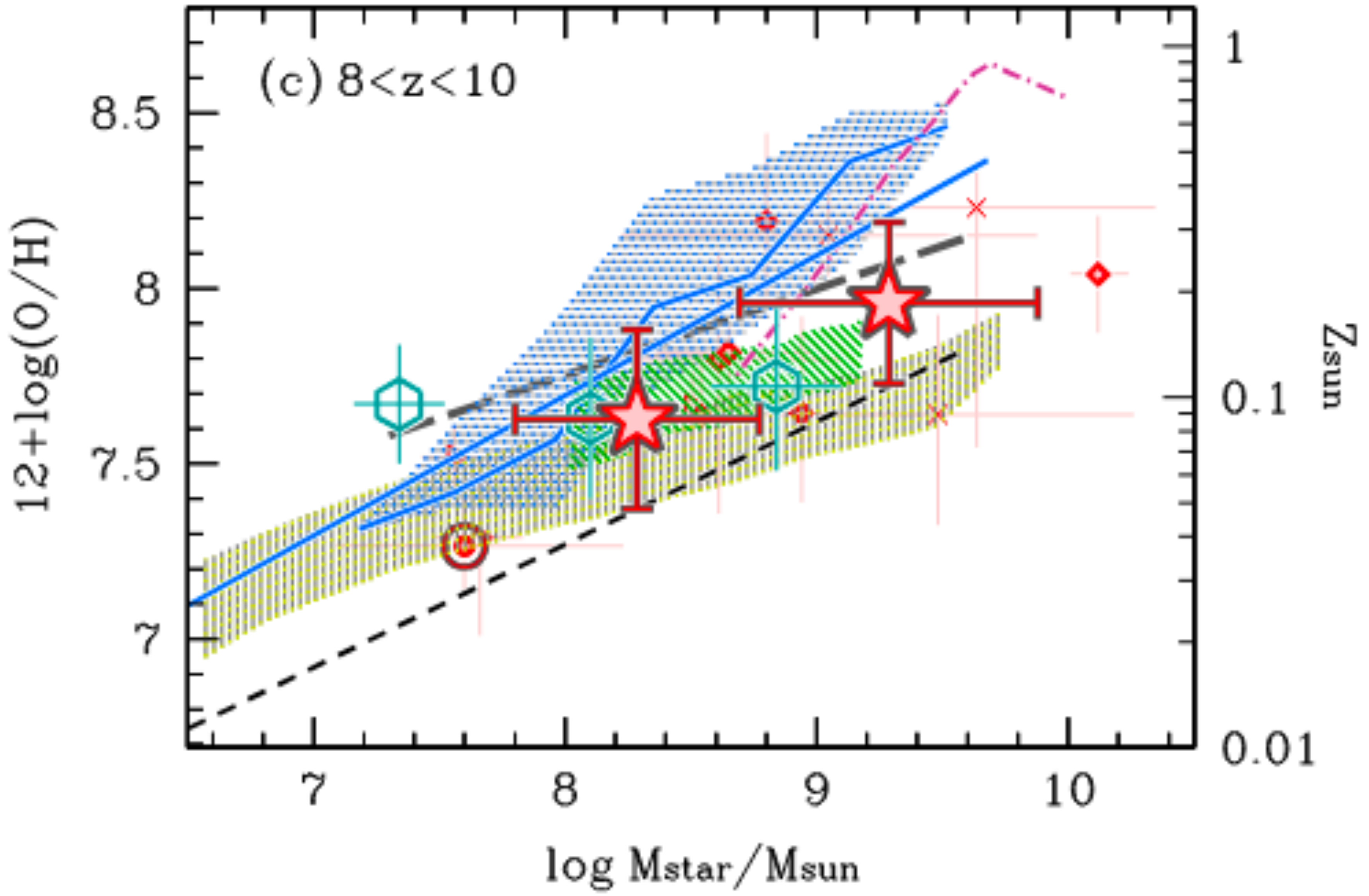

Figure 11. The MZ relation in three different redshift bins: (a) $z = 4$–6, (b) $z = 6$–8, and (c) $z = 8$–10. The red symbols and the best-fit function (Eq. 1) are as shown in Figure 10. The large stars represent the average MZ relations re-derived in each redshift bin, by splitting the sample into two groups based on stellar mass to have the equal numbers of galaxies. For the JADES+CEERS relations (Curti et al. 2023b in emerald green), we plot their $z = 3 - 6$ sub-sample's relations in Panel (a), while adopt the $z = 6 - 10$ relations in Panels (b) and (c). In addition, the cosmological simulation results at $z = 5$, 7, and 9 are displayed in Panel (a), (b), and (c), respectively; FIRE in black (Ma et al. 2016), IllustrisTNG in green (Torrey et al. 2019), FirstLight in blue (Langan et al. 2020 in the low-mass regime with solid curves, and Nakazato et al. 2023 in the high-mass regime with shades), Astraeus in yellow (Ucci et al. 2021), and FLARES in magenta (Wilkins et al. 2022). Some extrapolations are applied, as detailed in the text.

Backup Slides

Study high-redshift gaseous environments to look for the <u>signatures of the first stars</u> and explore the <u>chemical evolution of galaxies</u>

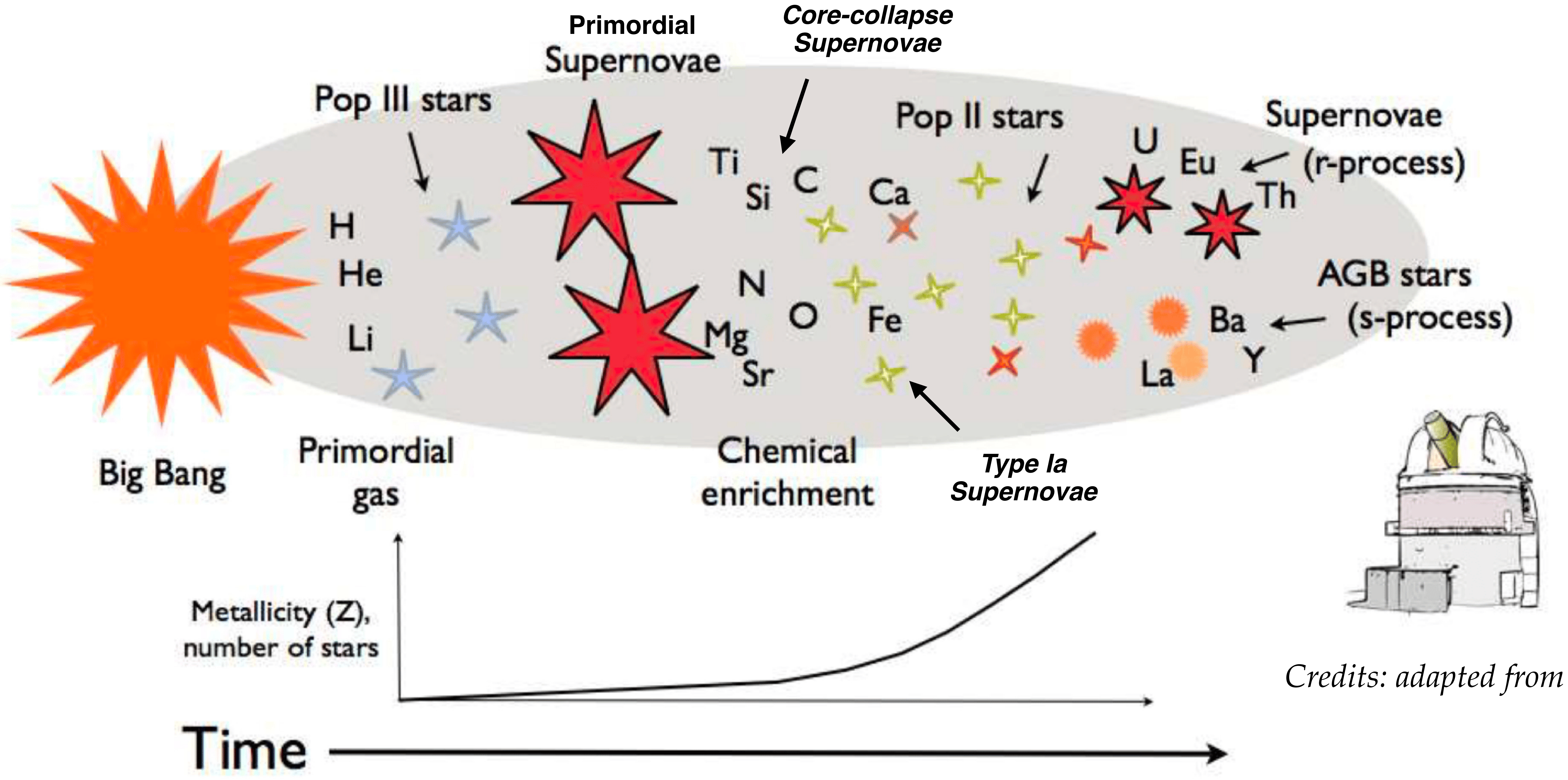

Credits: adapted from Tito & Pavlov 2020

Few Constrains on THE NEUTRAL GAS

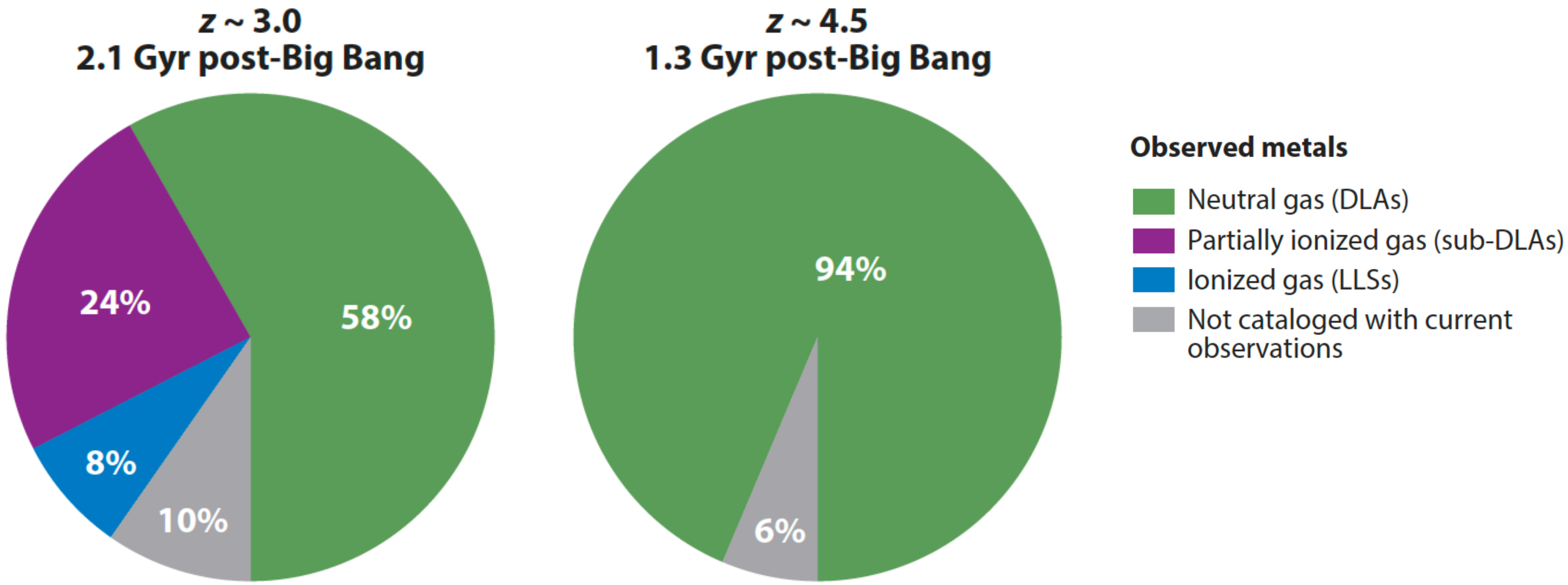

Credits: adapted from Péroux & Howk 2020

Backup Slides

A

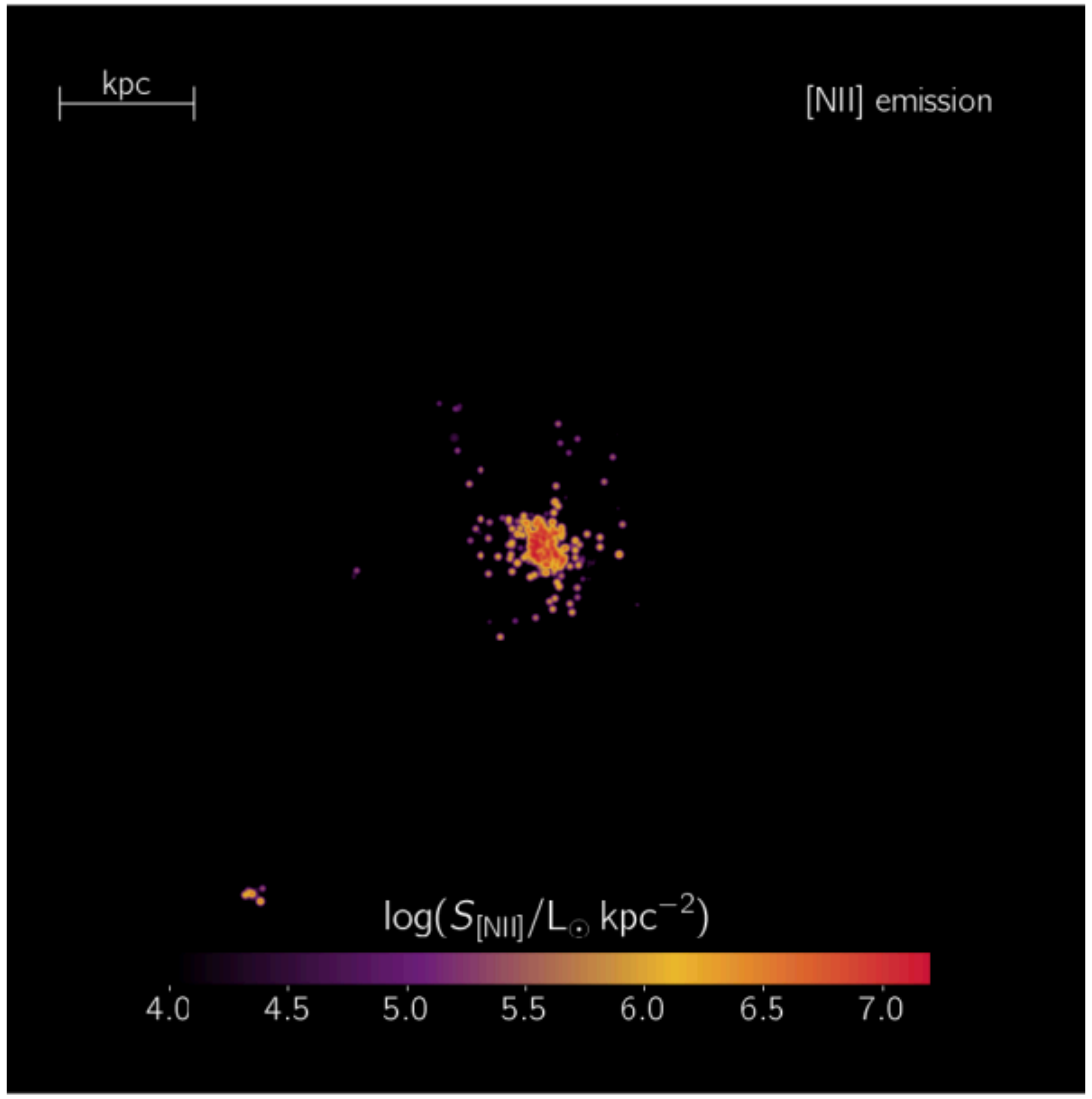

B

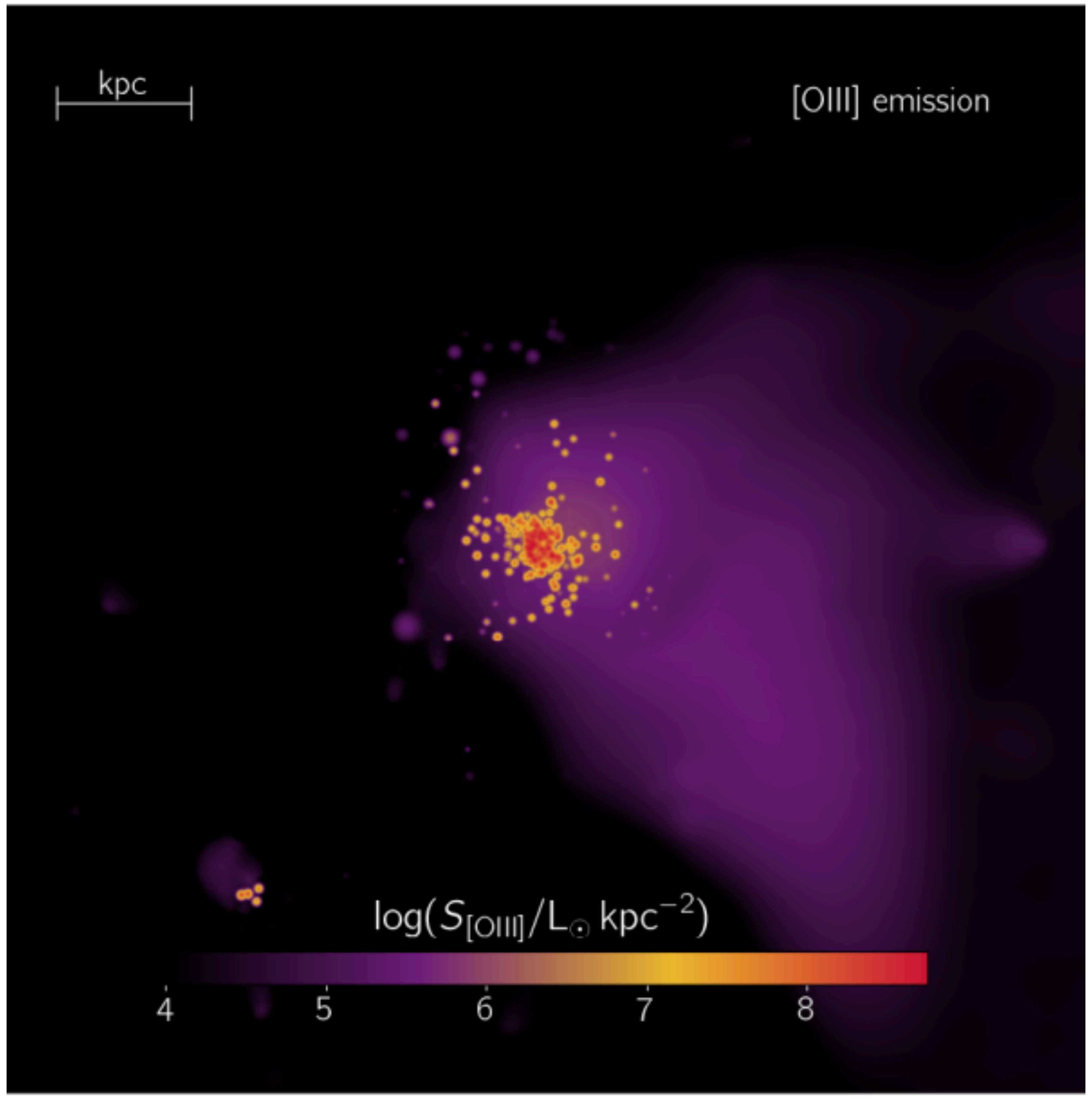

C

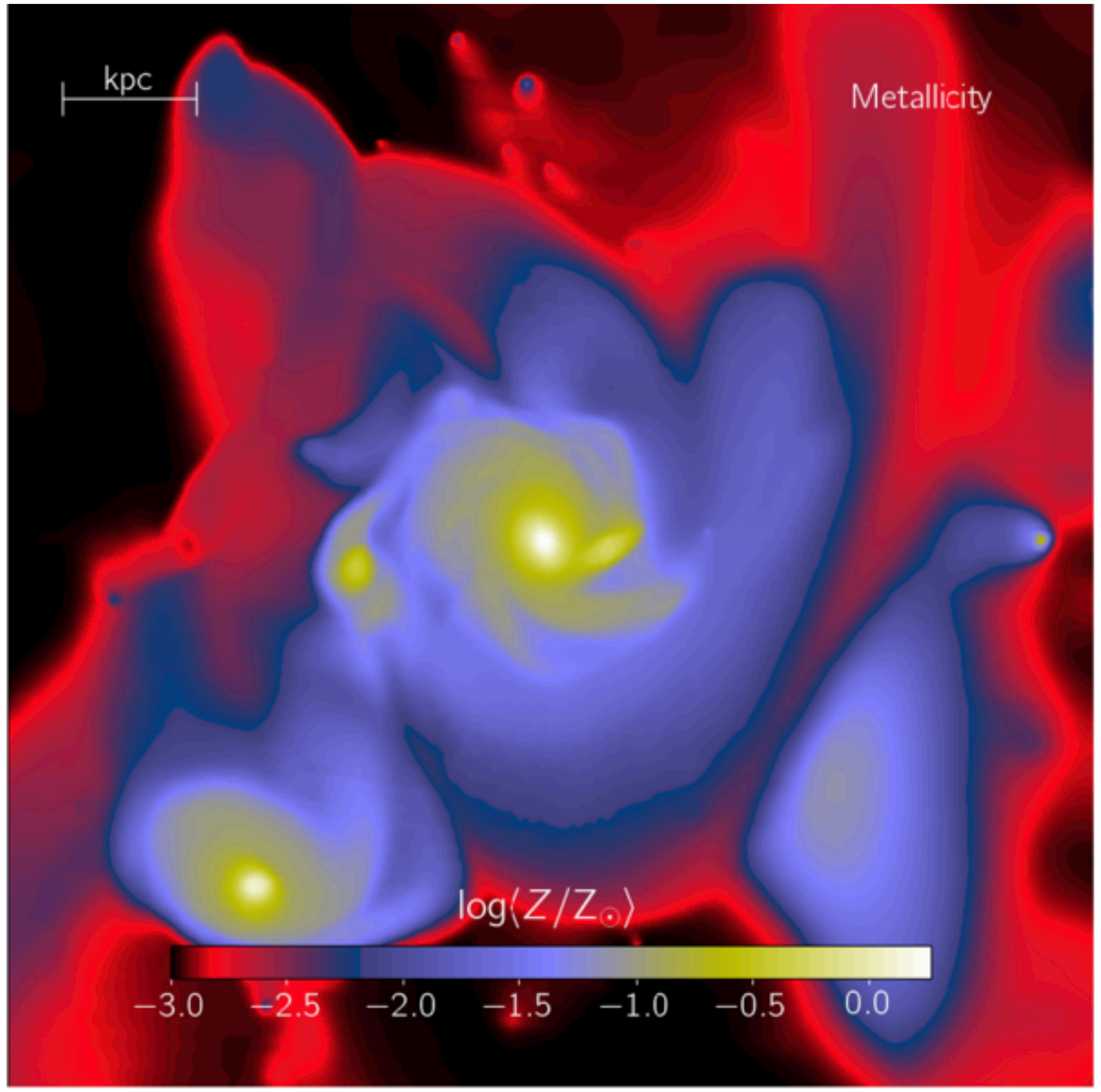

Credits: adapted from Pallottini et al. 2019

GRB

Backup Slides

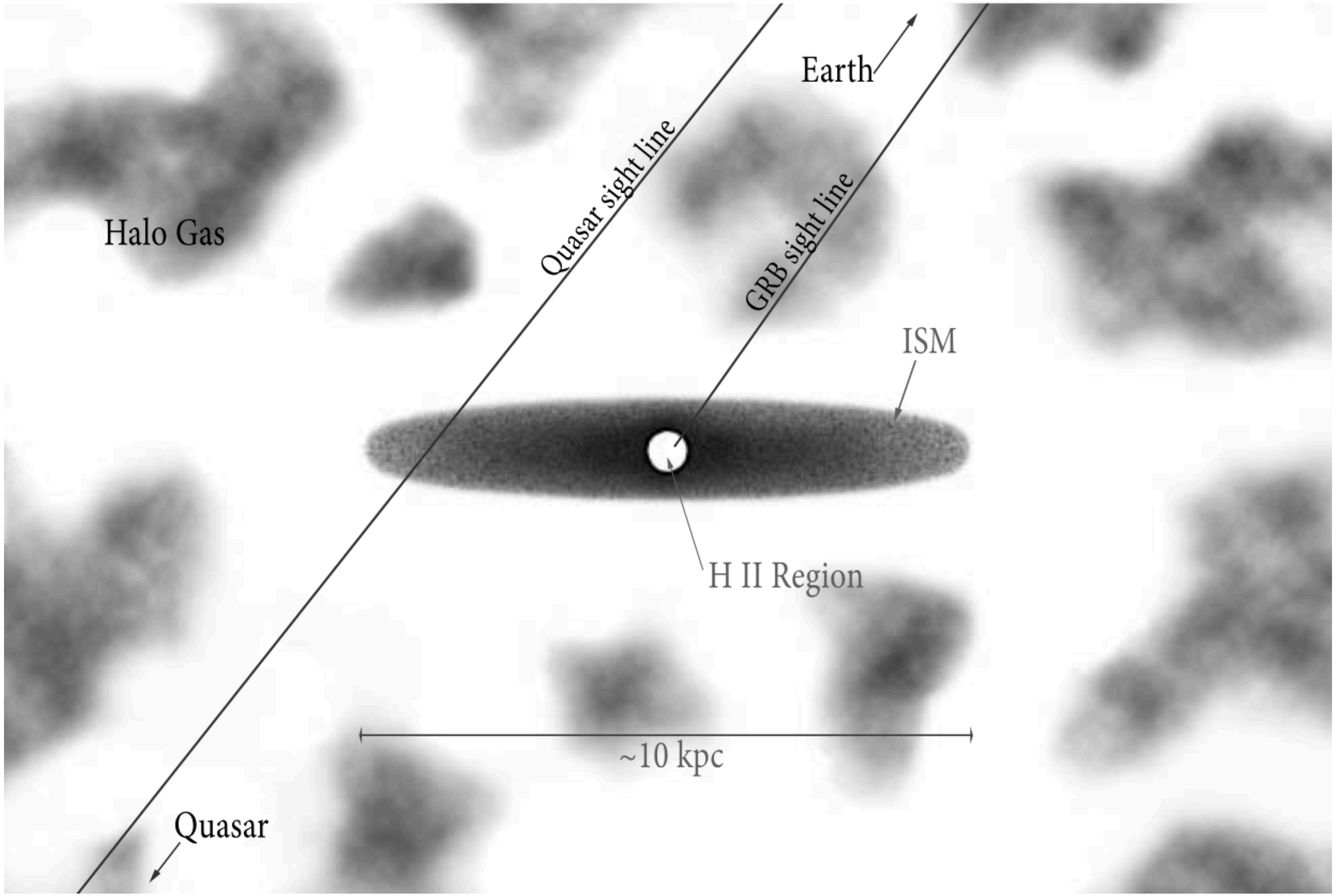

Credits: Prochaska et al. 2008

Backup Slides

Stargate Collaboration

PIs: N. Tanvir, S.D. Vergani, D. Malesani

ESO Large Programme

GRBs Follow-up with optical-NIR telescopes

Alert

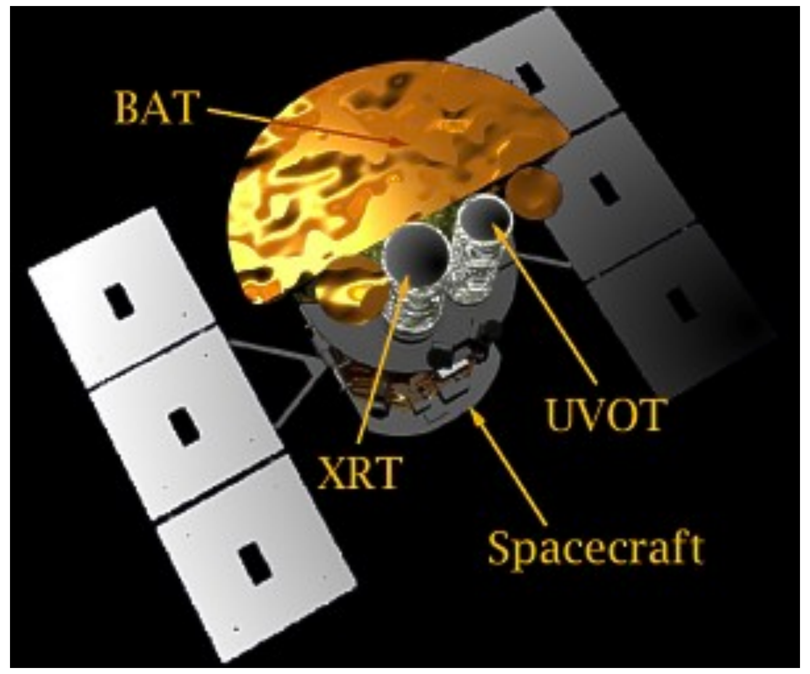

Credits: Neil Gehrels Swift Observatory

Robotic

Seconds

+

Hours

ToO mode

Observations

Credits: ESO/M. Claro

Quick Analysis

GCN

General Coordinates Network

Time-Domain and Multimessenger Alert System

Backup Slides

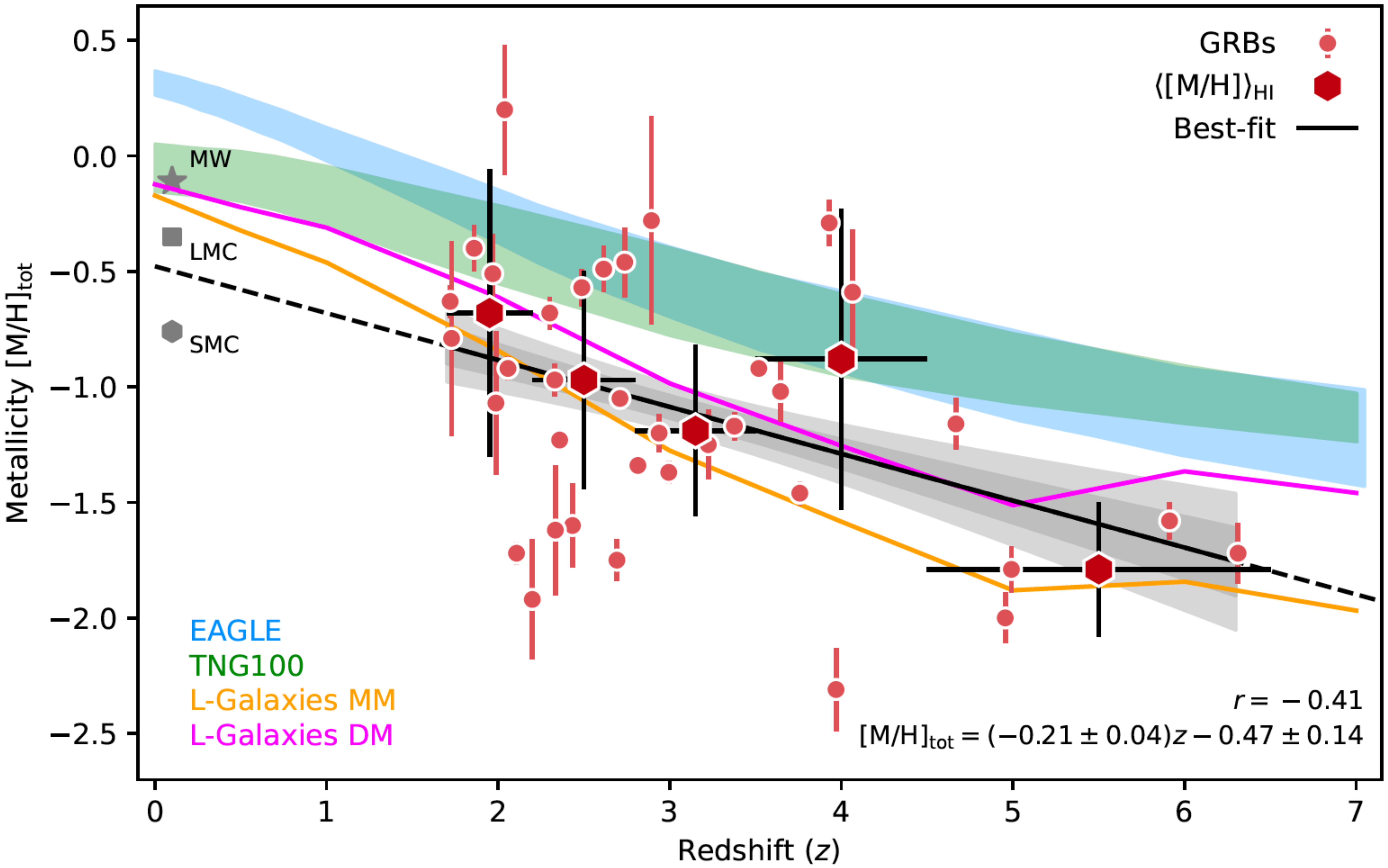

Backup Slides

- **[M/H]** — ***Total metallicity, related to solar, corrected for dust depletion***

$$[X/H]_{tot} = [X/H] - \delta_X$$

- **DTM** — **The mass of the elements X_i in the dust phase relative to the total metal mass in the line of sight**

$$DTM = M_{dust}/M_{metals} = \frac{\sum_{X_i} (1 - 10^{\delta_{X_i}}) \times 10^{[X_i/H]_\odot} \times W_{X_i}}{\sum_{X_i} (10^{[X_i/H]_\odot} \times W_{X_i})}$$

- ***[Zn/Fe]*** — *Dust tracer*

Backup Slides

Abundance patterns: ISM metallicities

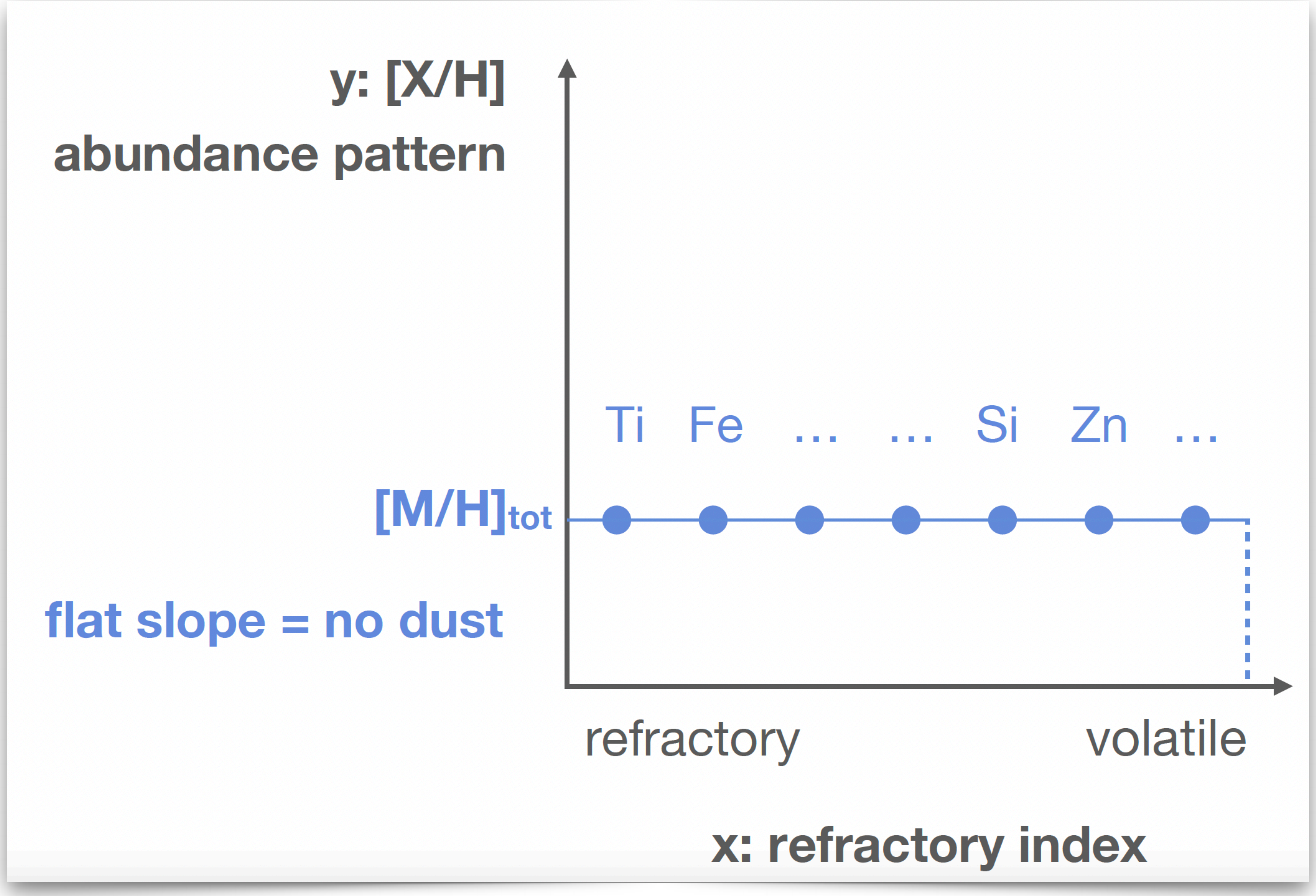

Courtesy of A. De Cia

__Following De Cia et al. 2016, De Cia et al. 2021__

AXIS

X = How refractory is an element

Y = Elements abundances

FIT

Slope —> $[Zn/Fe]_{fit}$

Intercept —> $[M/H]_{tot}$

Backup Slides

Abundance patterns: ISM metallicities + Dust

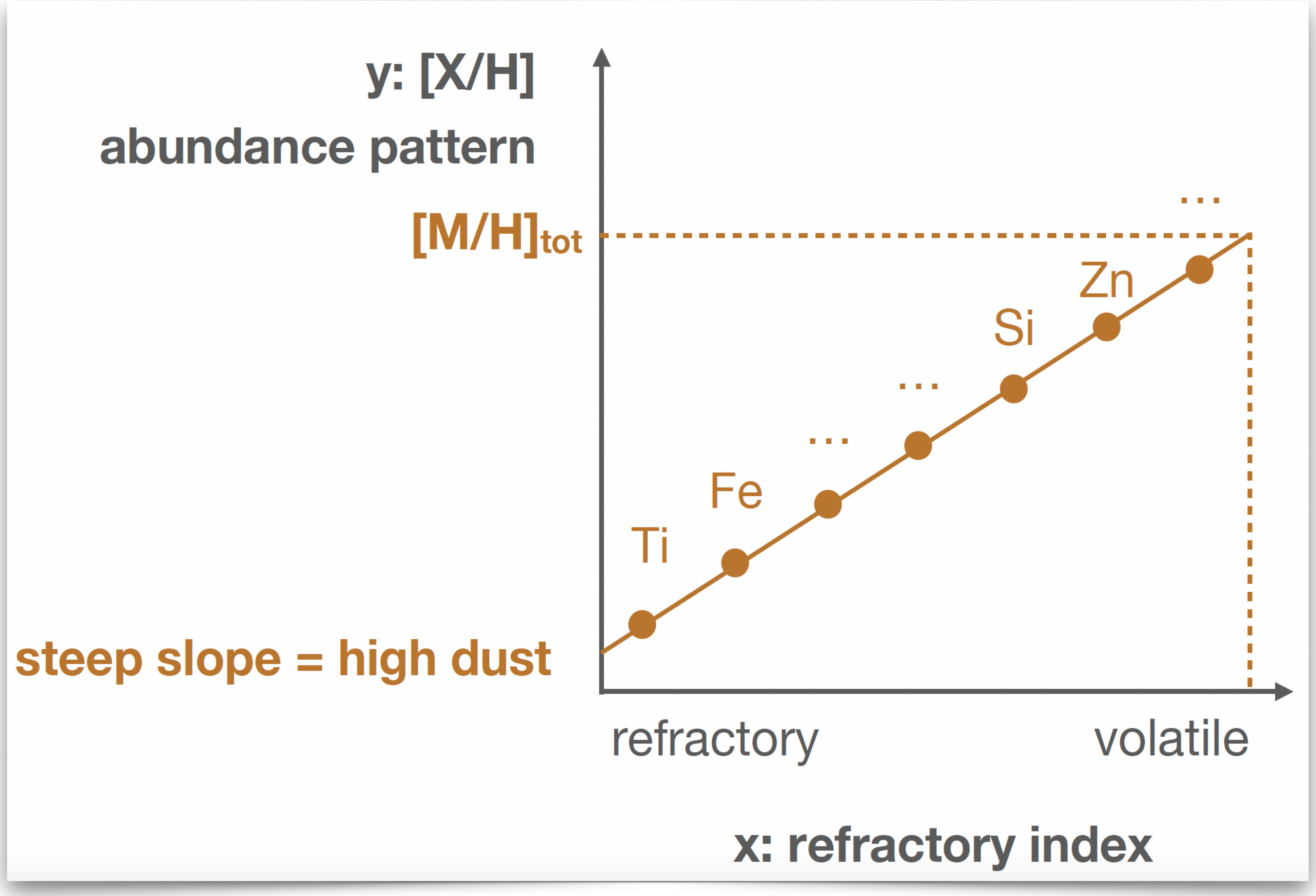

Courtesy of A. De Cia

Following De Cia et al. 2016, De Cia et al. 2021

AXIS

X = How refractory is an element

Y = Elements abundances

FIT

Slope —> $[Zn/Fe]_{fit}$

Intercept —> $[M/H]_{tot}$

Backup Slides

Abundance patterns: ISM metallicities + Dust + α-element enhancements

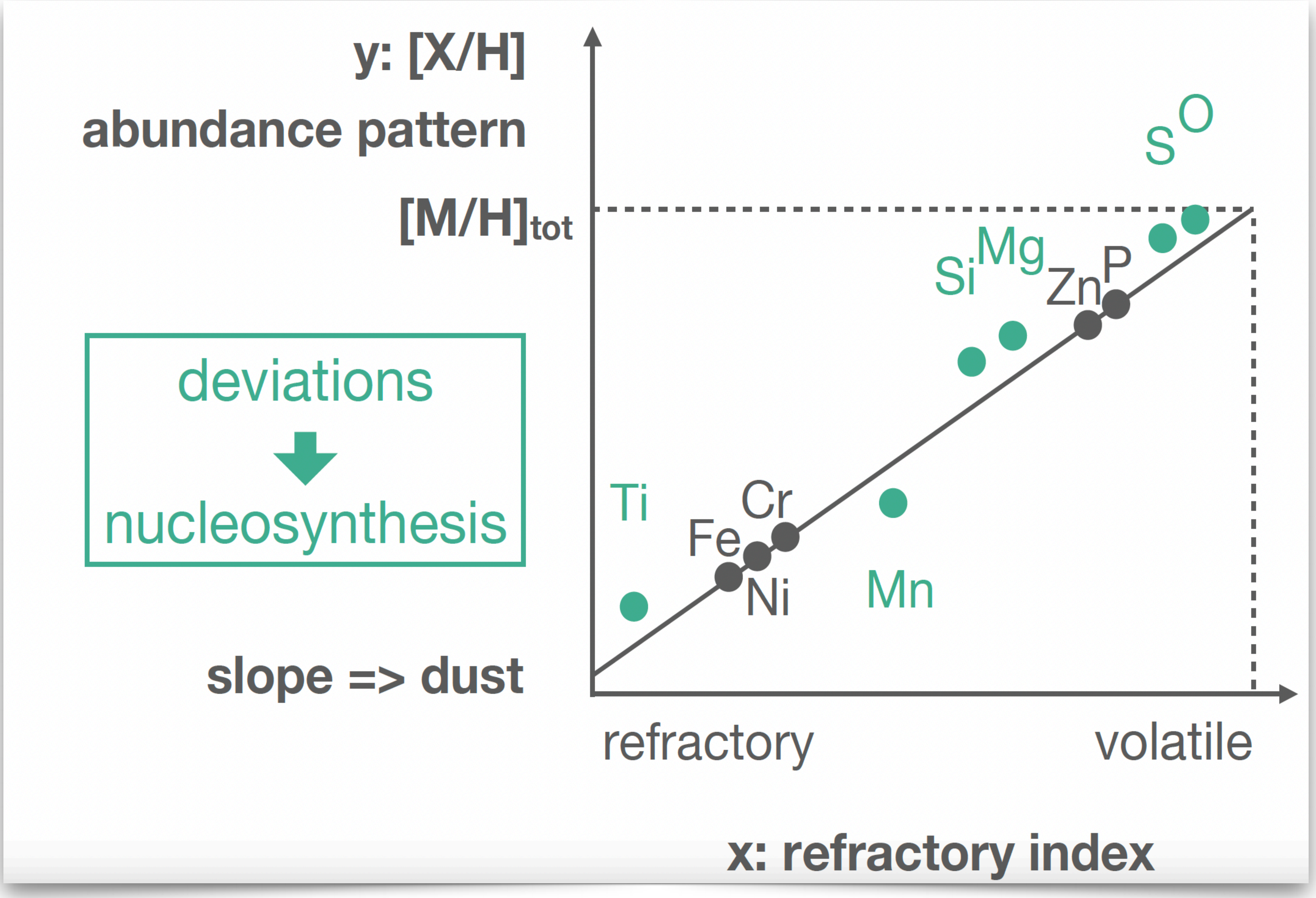

Courtesy of A. De Cia

Following De Cia et al. 2016, De Cia et al. 2021

AXIS

X = How refractory is an element

Y = Elements abundances

FIT

Slope —> $[Zn/Fe]_{fit}$

Intercept —> $[M/H]_{tot}$

Backup Slides

Credits: De Cia et al. 2024

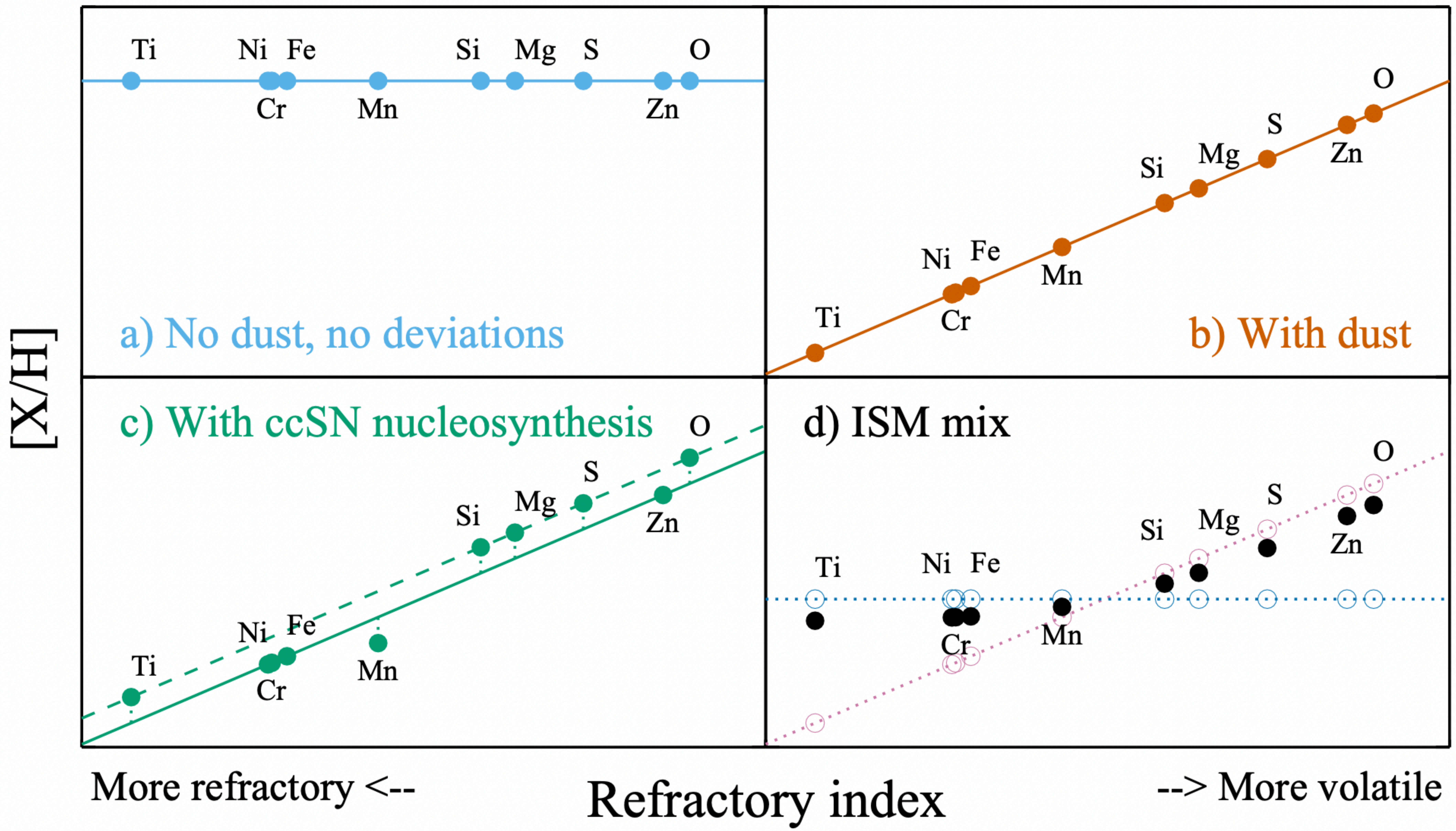

Backup Slides

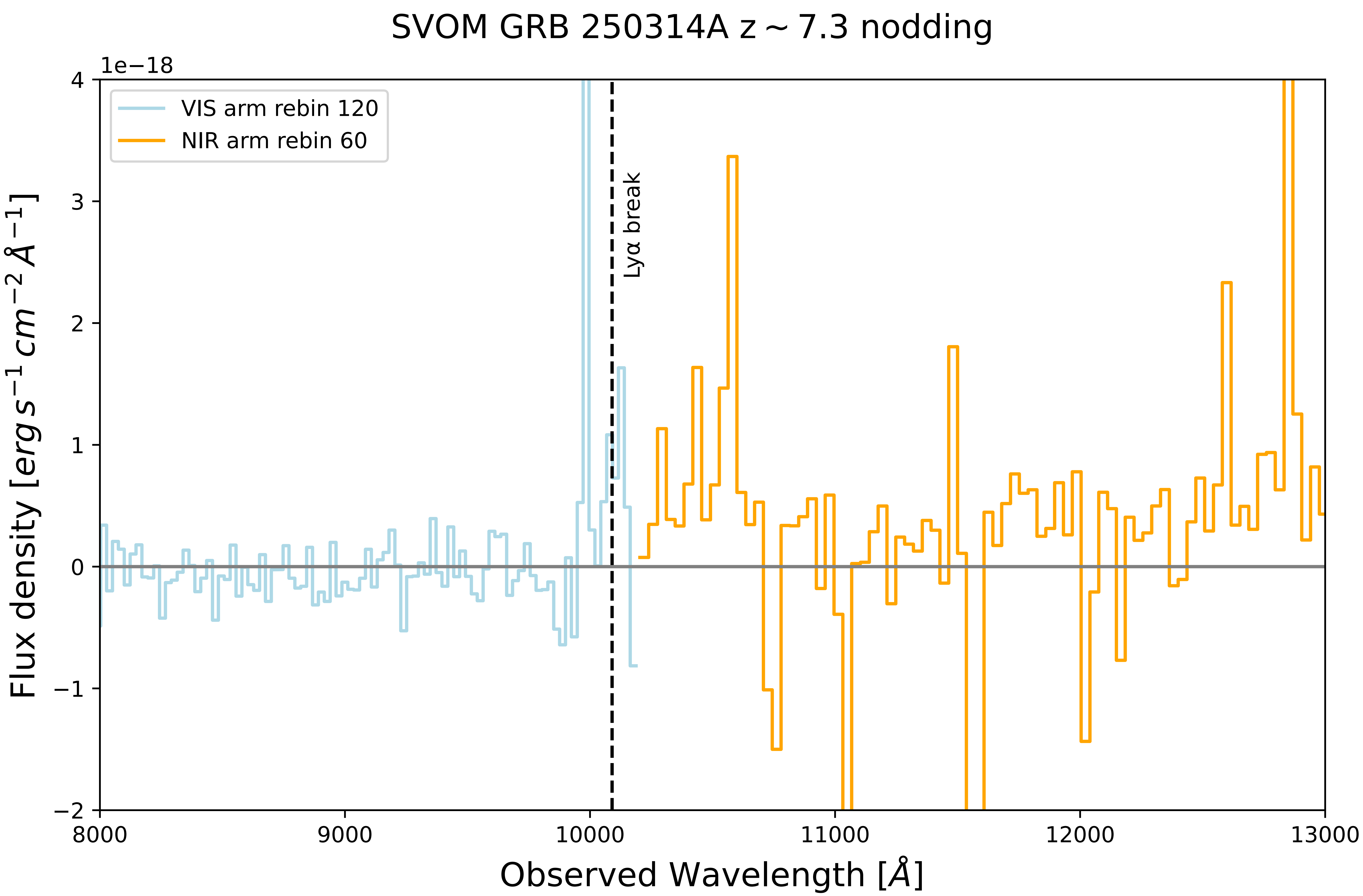

Backup Slides

GRB 210905A J~18.9 (~2.5hr) REM/REMIR
GRB 240218A J~20.51 (~25.9hr) LBT/LUCI
GRB 250314A J~22.4 (~16.8hr) GTC/OSIRIS

Backup Slides

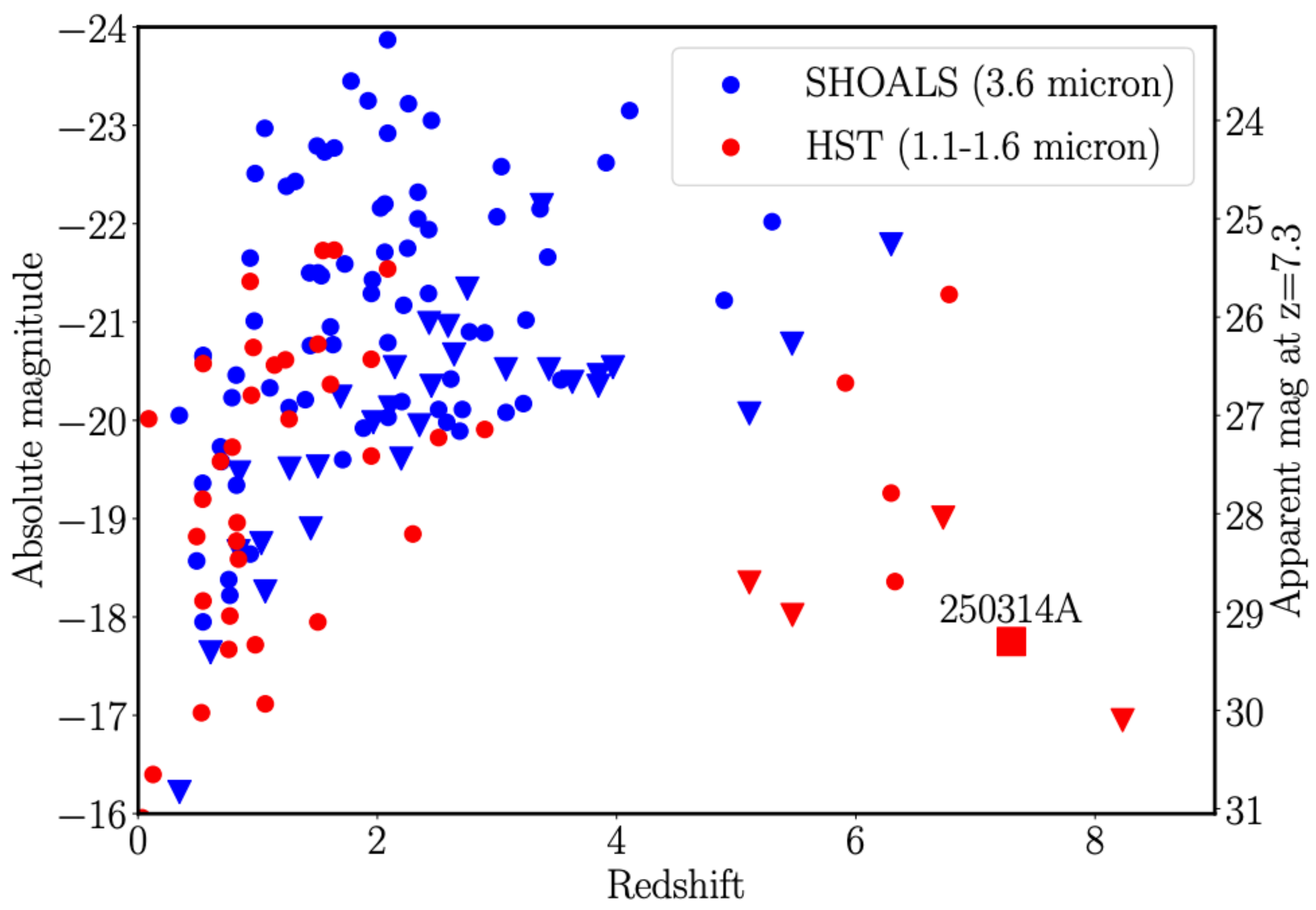

Fig. C.1: Comparison of GRB host galaxy absolute magnitudes (or upper limits) from the SHOALS sample at 3.6 microns (Perley et al. 2016), and from various *HST* observations at 1.1-1.6 microns (Tanvir et al. 2012; McGuire et al. 2016; Lyman et al. 2017) (note that these are in a fixed observed band, and so substantially different rest-frame band at different redshifts). Under the assumption that the host of GRB 250314A dominates the emission in the F150W2 band, the observations are consistent with other GRB hosts at high-*z*.

GRB 210905A

Backup Slides

Detailed analysis of metallicity, chemical enrichment and dust depletion

The overall host galaxy

Component-by-component

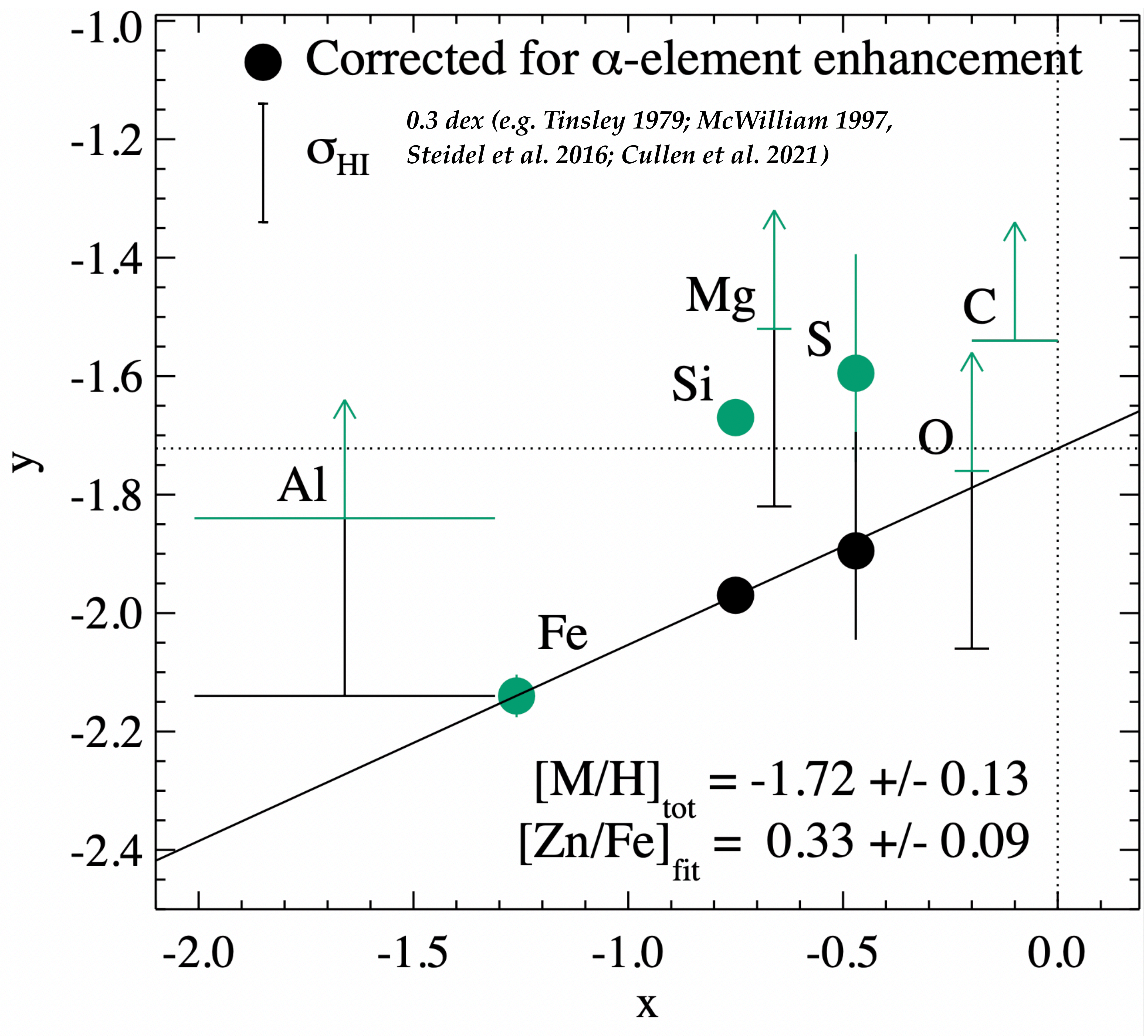

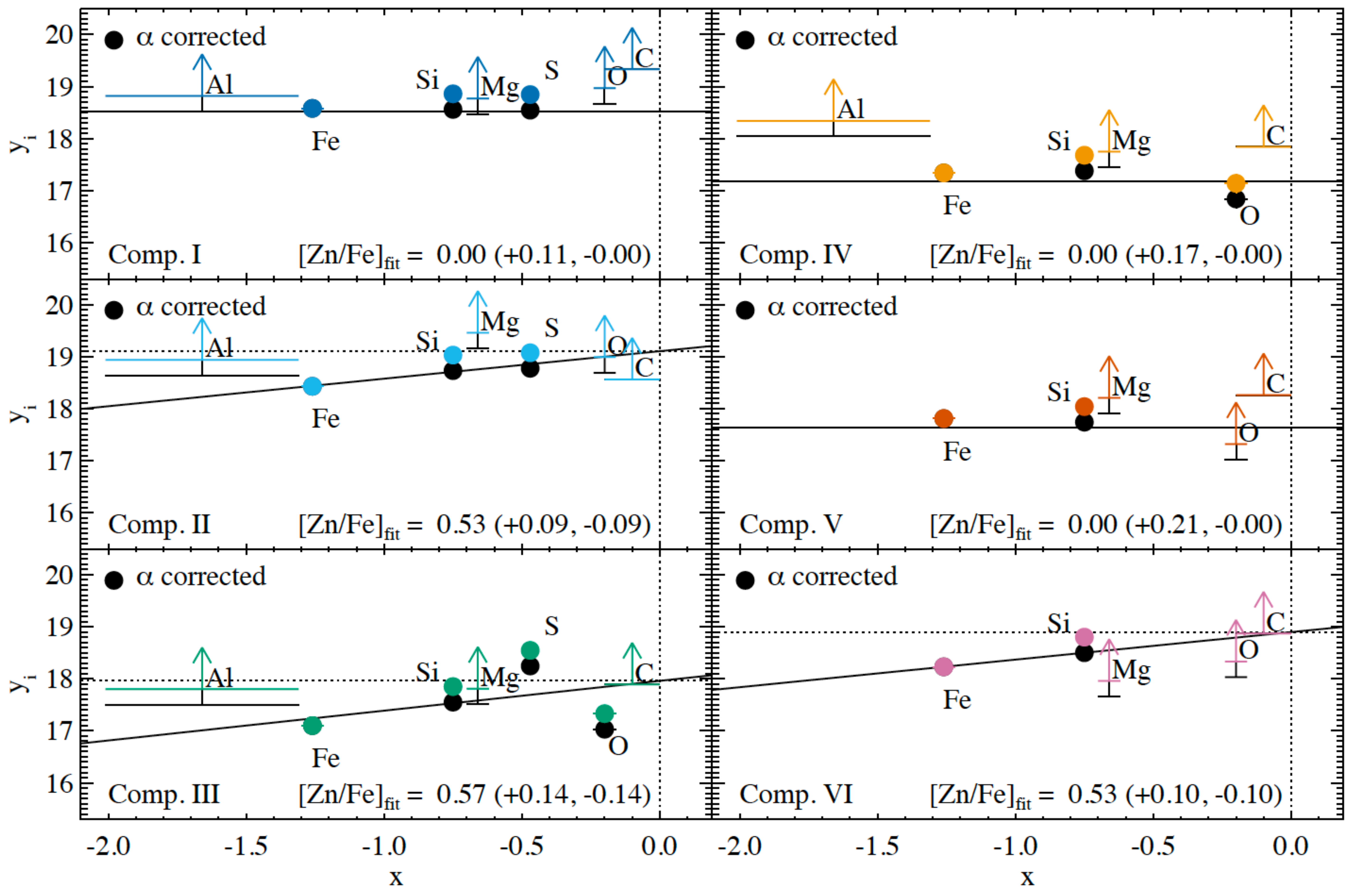

A. Saccardi, S.D. Vergani, A. De Cia et al. 2023

Backup Slides

RESULTS

-We find that the dust-corrected metallicity of the GRB host is [M/H] = -1.72 +/- 0.13 and DTM = 0.18 +/- 0.03

-We determine the total abundance pattern and for each component: the abundance ratios, $[X/Fe]_{nucl}$, are due to the effect of nucleosynthesis

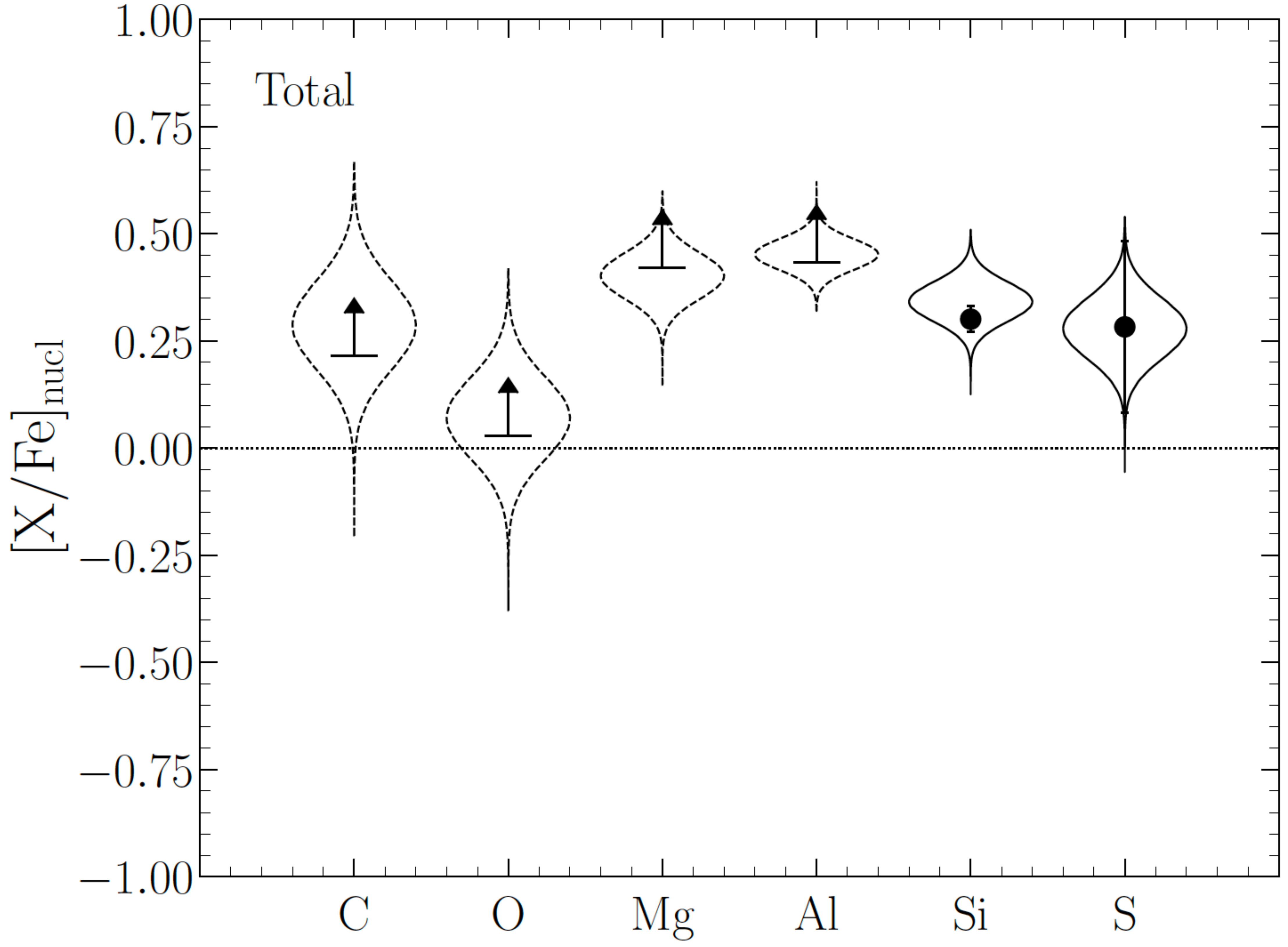

A. Saccardi, S.D. Vergani, A. De Cia et al. 2023

-Alpha element enhancement

-Nucleosynthesis due to core-collapse SNe and massive (S-)AGB stars.

(e.g., Masseron et al. 2020)

Backup Slides

RESULTS

-We find that the dust-corrected metallicity of the GRB host is [M/H] = -1.72 +/- 0.13 and DTM = 0.18 +/- 0.03

-We determine the total abundance pattern and for each component: the abundance ratios, $[X/Fe]_{nucl}$, are due to the effect of nucleosynthesis

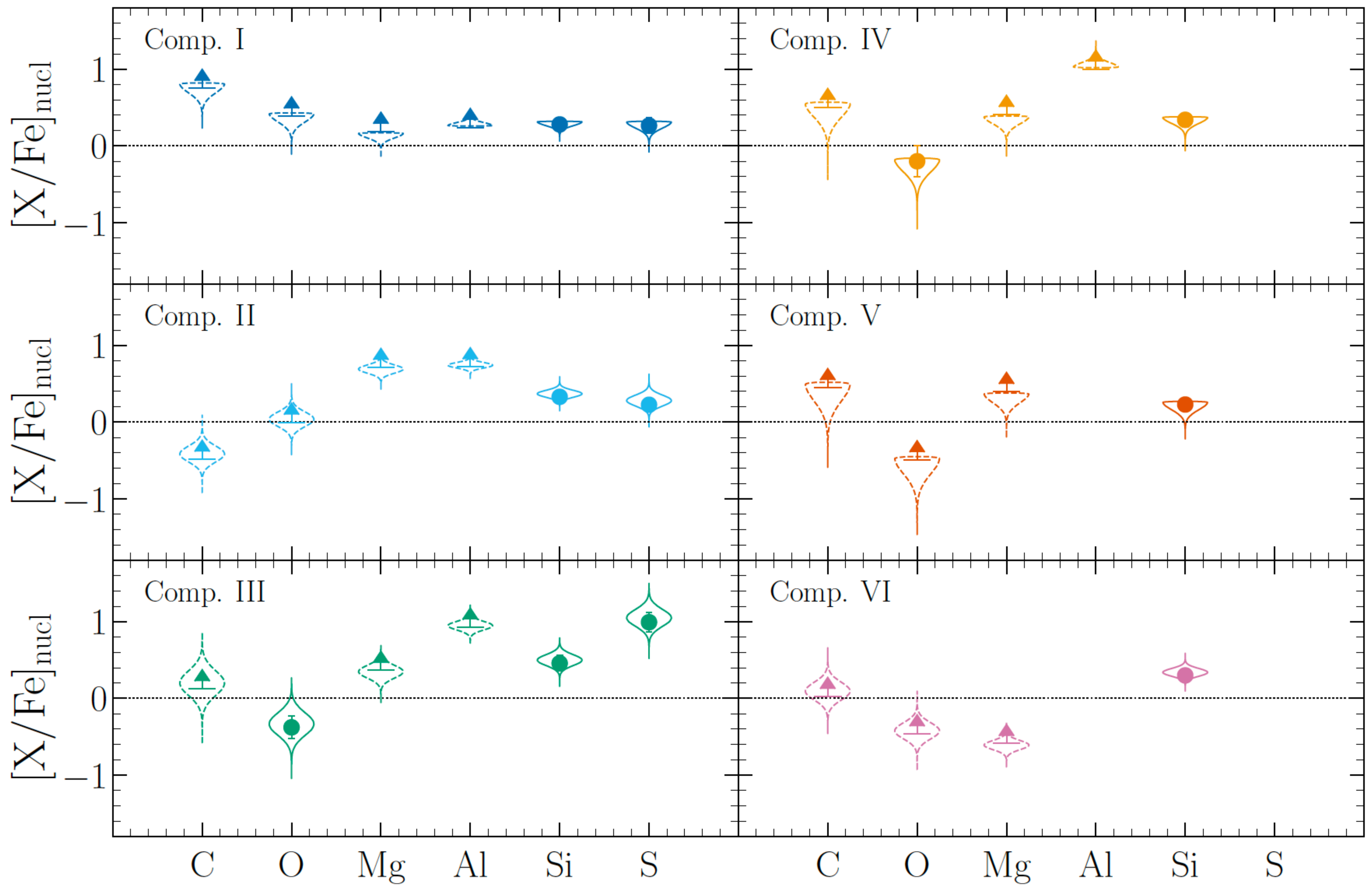

A. Saccardi, S.D. Vergani, A. De Cia et al. 2023

Over-abundance of aluminium
Under-abundance of oxygen:

-typical of some stars found in globular clusters and dwarf galaxies

-the best candidates are massive AGB stars and fast rotating massive stars

(e.g., Prantzos et al. 2007; Fulbright et al. 2007; Alves-Brito et al. 2010)

Backup Slides

The dust-corrected (total of gas and dust) abundances can defined as

$$[X/\mathrm{H}]_{\mathrm{tot}} = [X/\mathrm{H}] - \delta_X,$$

where [X/H] is the observed abundance of metal X and δ_X is its depletion in dust

A dust tracer can be [Zn/Fe].
Assuming a certain slope for the expected depletion:

$$\delta_X = A2_X + B2_X \times [\mathrm{Zn/Fe}],$$

$$y = a + bx,$$

$$a = [\mathrm{M/H}]_{\mathrm{tot}},$$

$$b = [\mathrm{Zn/Fe}]_{\mathrm{fit}},$$

$$x = B2_X,$$

$$y = \log N(X) - X_{\odot} + 12. - A2_X - \log N(\mathrm{H})$$

Backup Slides

We derive the dust-to-metal mass ratio (DTM), that is the ratio between the mass of dust and the total mass of the metals, as follows:

$$DTM = \frac{\Sigma_X(1 - 10^{\delta_X}) \times 10^{[X/H]_\odot} \times W_X}{\Sigma_X(10^{[X/H]_\odot} \times W_X)} \quad (1)$$

where the metal depletions δ_X are derived from the $[Zn/Fe]_{fit}$ following De Cia et al. (2016), $[X/H]_\odot$ are the solar abundances $X_\odot$ - 12, W_X are the atomic weights of the metals considered. In practice, we include all the elements with an elemental abundance above 3 (in the scale where H has an abundance of 12, Asplund et al. 2009), in the same way as Konstantopoulou et al. (2022).

Backup Slides

Table A.3: [X/Fe] residuals of the depletion pattern fitting (see Figs. 7, A.4 and A.5). The values and uncertainties are obtained including MC simulations to take into account the dust depletion errors. We stress that the impact of dust depletion on the nuclear abundances is correlated between elements; i.e., a higher dust depletion correction lowers all [X/Fe] values except for [Al/Fe] which it raises, and vice-versa.

With α-element corr.	I	II	III	IV	V	VI	Tot
[C/Fe]	$0.73^{+0.06}_{-0.09}$	$-0.41^{+0.10}_{-0.10}$	$0.20^{+0.16}_{-0.16}$	$0.44^{+0.09}_{-0.14}$	$0.36^{+0.12}_{-0.18}$	$0.10^{+0.12}_{-0.12}$	$0.29^{+0.10}_{-0.10}$
[O/Fe]	$0.35^{+0.06}_{-0.09}$	$0.04^{+0.09}_{-0.10}$	$-0.33^{+0.15}_{-0.15}$	$-0.28^{+0.09}_{-0.13}$	$-0.60^{+0.11}_{-0.16}$	$-0.42^{+0.11}_{-0.11}$	$0.07^{+0.09}_{-0.09}$
[Mg/Fe]	$0.13^{+0.03}_{-0.05}$	$0.69^{+0.05}_{-0.05}$	$0.35^{+0.08}_{-0.08}$	$0.32^{+0.05}_{-0.07}$	$0.30^{+0.06}_{-0.09}$	$-0.61^{+0.06}_{-0.06}$	$0.40^{+0.05}_{-0.05}$
[Al/Fe]	$0.29^{+0.03}_{-0.02}$	$0.74^{+0.04}_{-0.04}$	$0.95^{+0.06}_{-0.06}$	$1.07^{+0.05}_{-0.03}$			$0.45^{+0.04}_{-0.04}$
[Si/Fe]	$0.28^{+0.03}_{-0.04}$	$0.37^{+0.05}_{-0.05}$	$0.50^{+0.07}_{-0.07}$	$0.32^{+0.04}_{-0.06}$	$0.20^{+0.05}_{-0.08}$	$0.34^{+0.05}_{-0.05}$	$0.34^{+0.05}_{-0.05}$
[S/Fe]	$0.26^{+0.04}_{-0.06}$	$0.28^{+0.07}_{-0.07}$	$1.05^{+0.11}_{-0.11}$				$0.28^{+0.07}_{-0.07}$
Without α-element corr.	I	II	III	IV	V	VI	Tot
[C/Fe]	$0.31^{+0.13}_{-0.13}$	$-0.97^{+0.13}_{-0.13}$	$-0.24^{+0.17}_{-0.17}$	$0.29^{+0.16}_{-0.18}$	$0.00^{+0.21}_{-0.22}$	$-0.59^{+0.16}_{-0.16}$	$-0.36^{+0.14}_{-0.14}$
[O/Fe]	$-0.04^{+0.12}_{-0.12}$	$-0.47^{+0.12}_{-0.12}$	$-0.74^{+0.16}_{-0.16}$	$-0.42^{+0.15}_{-0.17}$	$-0.93^{+0.20}_{-0.20}$	$-1.05^{+0.15}_{-0.15}$	$-0.52^{+0.13}_{-0.13}$
[Mg/Fe]	$-0.09^{+0.07}_{-0.07}$	$0.40^{+0.07}_{-0.07}$	$0.12^{+0.09}_{-0.09}$	$0.25^{+0.08}_{-0.10}$	$0.11^{+0.11}_{-0.11}$	$-0.96^{+0.08}_{-0.08}$	$0.07^{+0.07}_{-0.07}$
[Al/Fe]	$0.44^{+0.04}_{-0.04}$	$0.93^{+0.04}_{-0.04}$	$1.10^{+0.06}_{-0.06}$	$1.12^{+0.06}_{-0.06}$			$0.68^{+0.05}_{-0.05}$
[Si/Fe]	$0.10^{+0.06}_{-0.06}$	$0.12^{+0.06}_{-0.06}$	$0.31^{+0.08}_{-0.08}$	$0.26^{+0.07}_{-0.08}$	$0.04^{+0.09}_{-0.10}$	$0.04^{+0.07}_{-0.07}$	$0.06^{+0.06}_{-0.06}$
[S/Fe]	$-0.03^{+0.09}_{-0.09}$	$-0.10^{+0.09}_{-0.09}$	$0.75^{+0.12}_{-0.12}$				$-0.16^{+0.09}_{-0.09}$

Backup Slides

Table 6: Properties derived from the total metal abundances and component by component. The total metallicity ($[M/H]_{tot}$), dust depletion $[Zn/Fe]_{fit}$ and dust-to-metal ratio (DTM) are reported for the analysis performed taking α-element enhancement into account.

With α-element corr.	*I*	*II*	*III*	*IV*	*V*	*VI*	Tot
$[M/H]_{tot}$							-1.72 ± 0.13
$[Zn/Fe]_{fit}$	$0.00^{+0.11}_{-0.00}$	$0.53^{+0.09}_{-0.09}$	$0.57^{+0.14}_{-0.14}$	$0.00^{+0.17}_{-0.00}$	$0.00^{+0.21}_{-0.00}$	$0.53^{+0.10}_{-0.10}$	0.33 ± 0.09
DTM	$0.00^{+0.04}_{-0.00}$	$0.26^{+0.03}_{-0.03}$	$0.27^{+0.04}_{-0.04}$	$0.00^{+0.06}_{-0.00}$	$0.00^{+0.07}_{-0.00}$	$0.26^{+0.03}_{-0.03}$	0.18 ± 0.03

Backup Slides

Table A.1: Properties derived from the total metal abundances and component by component. The total metallicity ($[M/H]_{tot}$), dust depletion $[Zn/Fe]_{fit}$, dust-to-metal ratio (DTM) and dust extinction (A_V (mag)) are reported for the analysis performed not taking α-element enhancement into account.

Without α-element corr.	I	II	III	IV	V	VI	Tot
$[M/H]_{tot}$							-1.01 ± 0.14
$[Zn/Fe]_{fit}$	$0.44^{+0.11}_{-0.11}$	$1.01^{+0.11}_{-0.11}$	$0.95^{+0.15}_{-0.15}$	$0.22^{+0.17}_{-0.17}$	$0.45^{+0.19}_{-0.19}$	$1.12^{+0.14}_{-0.14}$	0.89 ± 0.12
DTM	$0.23^{+0.03}_{-0.03}$	$0.38^{+0.04}_{-0.04}$	$0.37^{+0.04}_{-0.04}$	$0.13^{+0.04}_{-0.04}$	$0.23^{+0.04}_{-0.04}$	$0.41^{+0.05}_{-0.05}$	0.36 ± 0.04
A_V (mag)							0.04 ± 0.02

Backup Slides

Table 5: Metal abundances. For each element (first column), the total column density (second column), the ratio over iron (third column) and the metallicity are reported.

X	$\log(N/\mathrm{cm}^{-2})$	$[X/\mathrm{Fe}]$	[X/H]
C	> 16.02	> 0.66	> -1.5
O	> 16.03	> 0.41	> -1.8
Mg	> 15.13	> 0.61	> -1.6
Al	> 13.69	> 0.31	> -1.8
Si	14.90 ± 0.02	0.46 ± 0.04	-1.71 ± 0.11
S	> 14.50	> 0.45	> -1.7
Fe	14.43 ± 0.02		-2.17 ± 0.11

Backup Slides

$\log N_{HI} = 21.10 +/- 0.1$

Table 2: Column density of low ionization lines. The velocity shift of the components with respect to the N v line is indicated. The last row reports the Doppler parameter b of each component as resolved by the X-shooter observations.

Species	*I*	*II*	*III*	*IV*	*V*	*VI*
Velocity	$-255\,\mathrm{km\,s^{-1}}$	$-203\,\mathrm{km\,s^{-1}}$	$-136\,\mathrm{km\,s^{-1}}$	$-25\,\mathrm{km\,s^{-1}}$	$+46\,\mathrm{km\,s^{-1}}$	$+75\,\mathrm{km\,s^{-1}}$
C II $\lambda1334$	> 15.79	> 15.02	> 14.35	> 14.30	> 14.72	> 15.33
C II* $\lambda1335$					13.16 ± 0.17	13.43 ± 0.09
O I $\lambda1302$	> 15.66	> 15.68	14.02 ± 0.12	13.83 ± 0.18	> 14.01	> 15.02
Mg II $\lambda2796$, $\lambda2803^{§}$	> 14.32	> 15.01	> 13.36	> 13.30	> 13.76	> 13.51
Al II $\lambda1670^{‡}$	> 13.25	> 13.37	> 12.23	> 12.77		
Si II $\lambda1260$, $\lambda1304$, $\lambda1808$	14.33 ± 0.04	14.50 ± 0.03	13.32 ± 0.05	13.15 ± 0.03	13.51 ± 0.07	14.27 ± 0.02
Si II* $\lambda1264$		12.76 ± 0.04	12.49 ± 0.08		12.02 ± 0.09	12.44 ± 0.07
S II $\lambda1259^{†}$	13.99 ± 0.09	14.22 ± 0.09	13.69 ± 0.09			
Fe II $\lambda1608$, $\lambda2344$, $\lambda2382$	14.03 ± 0.04	13.88 ± 0.02	12.55 ± 0.09	12.79 ± 0.09	13.26 ± 0.04	13.68 ± 0.02
$b\,(\mathrm{km\,s^{-1}})$	15.6	27.7	21.7	28.4	29.6	23.2

§ Mg II lines are particularly uncertain because they are found in a very noisy region at the end of the NIR arm spectrum.

‡ The *V*, *VI* (and partially *IV*) components of Al II are strongly affected by a sky line and could not be determined.

† The *IV*, *V*, *VI* components of S II are blended with the Si II $\lambda1260$ Å absorption.

Table 3: Column density of high ionization lines. The velocity shift of the components with respect to the N v line are indicated. The last row reports the Doppler parameter b used of each component as resolved by the X-shooter observations.

Species	1	2	3	4
Velocity	$-220\,\mathrm{km\,s^{-1}}$	$-72\,\mathrm{km\,s^{-1}}$	$0\,\mathrm{km\,s^{-1}}$	$+71\,\mathrm{km\,s^{-1}}$
C IV $\lambda1548$,$\lambda1550$	> 14.36	> 14.13	> 16.2	> 14.08
N V $\lambda1238$, $\lambda1242$			> 14.25	
Si IV $\lambda1393$,$\lambda1402$	> 13.89	> 13.41	> 13.82	> 13.63
$b\,(\mathrm{km\,s^{-1}})$	56.2	46.0	15.5	31.2

Backup Slides

F140W magnitude is 25.66 ± 0.05 mag (AB), corresponding to $SFR_{UV} \sim 20\ M_{\odot}\ yr^{-1}$
(Rossi et al. 2022)

A. Saccardi, S.D. Vergani, A. De Cia et al. 2023

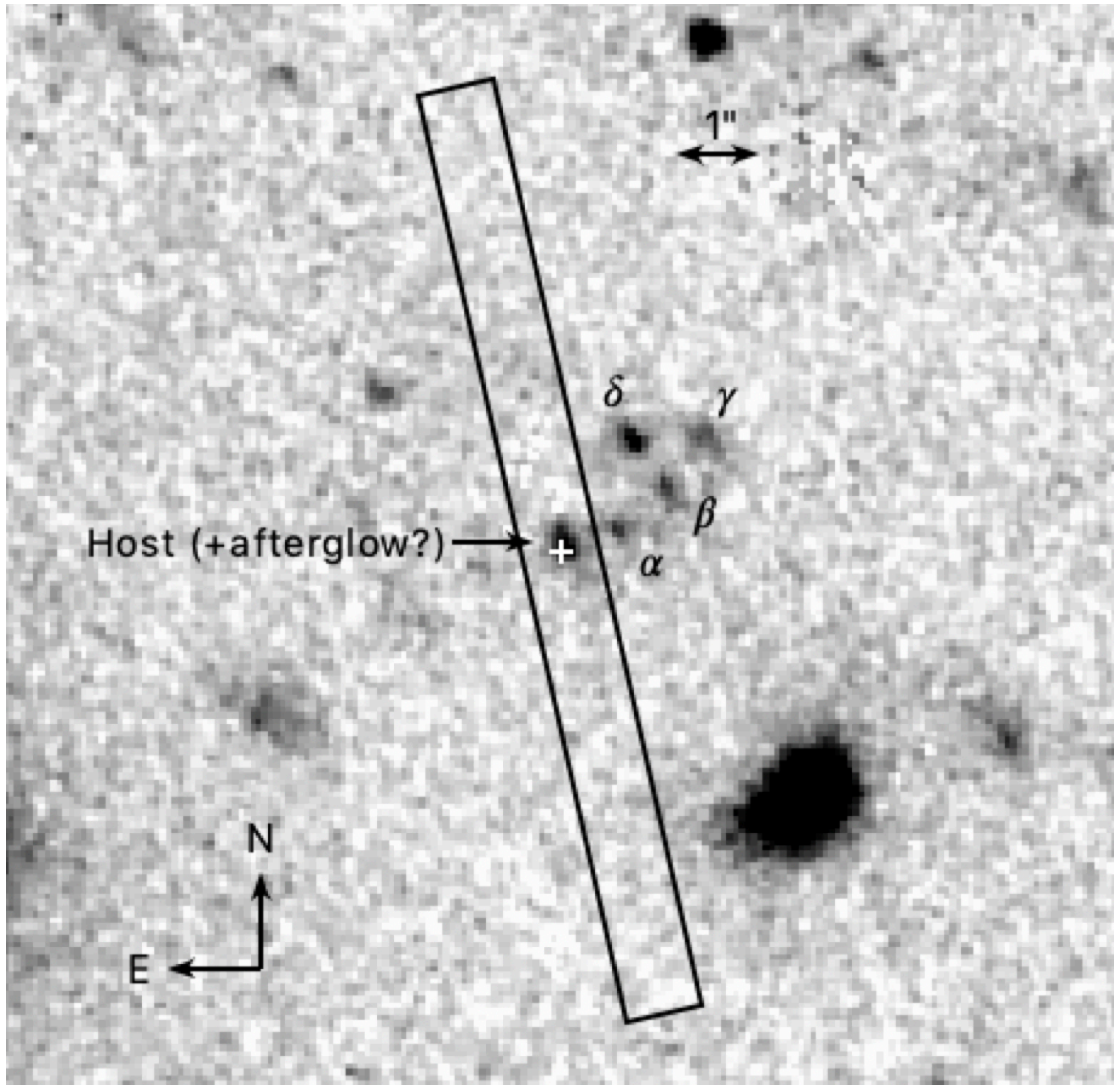

HST/F140W Image

	Projected Distance	**Distance z=6.3118**	**F140W mag (AB)**
α	**0.73″**	**4.14kpc**	**26.46 ± 0.07**
β	**1.43″**	**8.14kpc**	**26.38 ± 0.06**
γ	**1.53″**	**8.67kpc**	**26.34 ± 0.06**
δ	**2.13″**	**12.08kpc**	**25.98 ± 0.05**

$E_{iso} = 1.27 \times 10^{54}$ erg

$\log L_{iso} = 1.86 \times 10^{53}$ erg s^{-1}

Backup Slides

Rest-frame UV spectroscopy

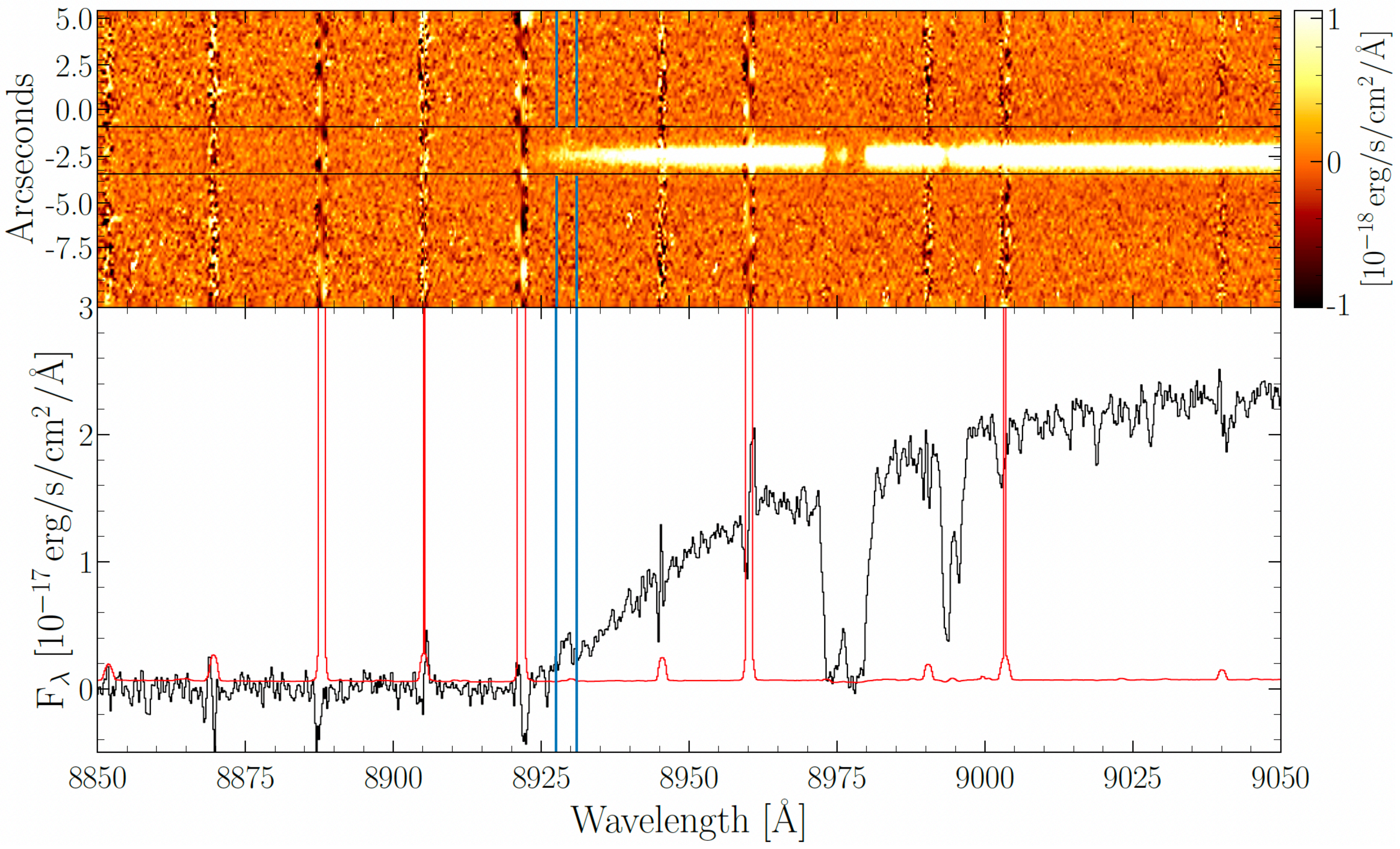

A. Saccardi, S.D. Vergani, A. De Cia et al. 2023

Tentative detection of an emission line at λ 8929Å (observer frame).

$F_{Ly\alpha} = (3.1\pm0.6)\times10^{-18}$ erg s^{-1} cm^{-2}

We tentatively associate it with extended Ly-α emission (covers ~ 2.5″) at z = 6.3449, i.e. ~ 1200 km s^{-1} redward of the DLA

High shift:
Lyα line peak is usually found shifted from the redshift of the host galaxy systemic emission

-Spectroscopic observations revealed Lyα emission at ~ 800 km s^{-1} from the UV galaxy emission lines
(e.g. Hashimoto et al. 2019)

-A shift of a few 100 km s^{-1} is often found between GRB afterglow absorption and emission lines
(e.g. Friis et al. 2015; Vielfaure et al. 2020)

Backup Slides

UV-Pumping

↓

Excite the absorber atoms and ions to a principal quantum number above the fundamental

↓

By a spontaneous emission, the fine structure lines of the fundamental state are populated

Photoionization code

INPUT:
-INCIDENCE FLUX
-INITIAL COLUMN DENSITIES

↓

OUTPUT:
-DISTANCE

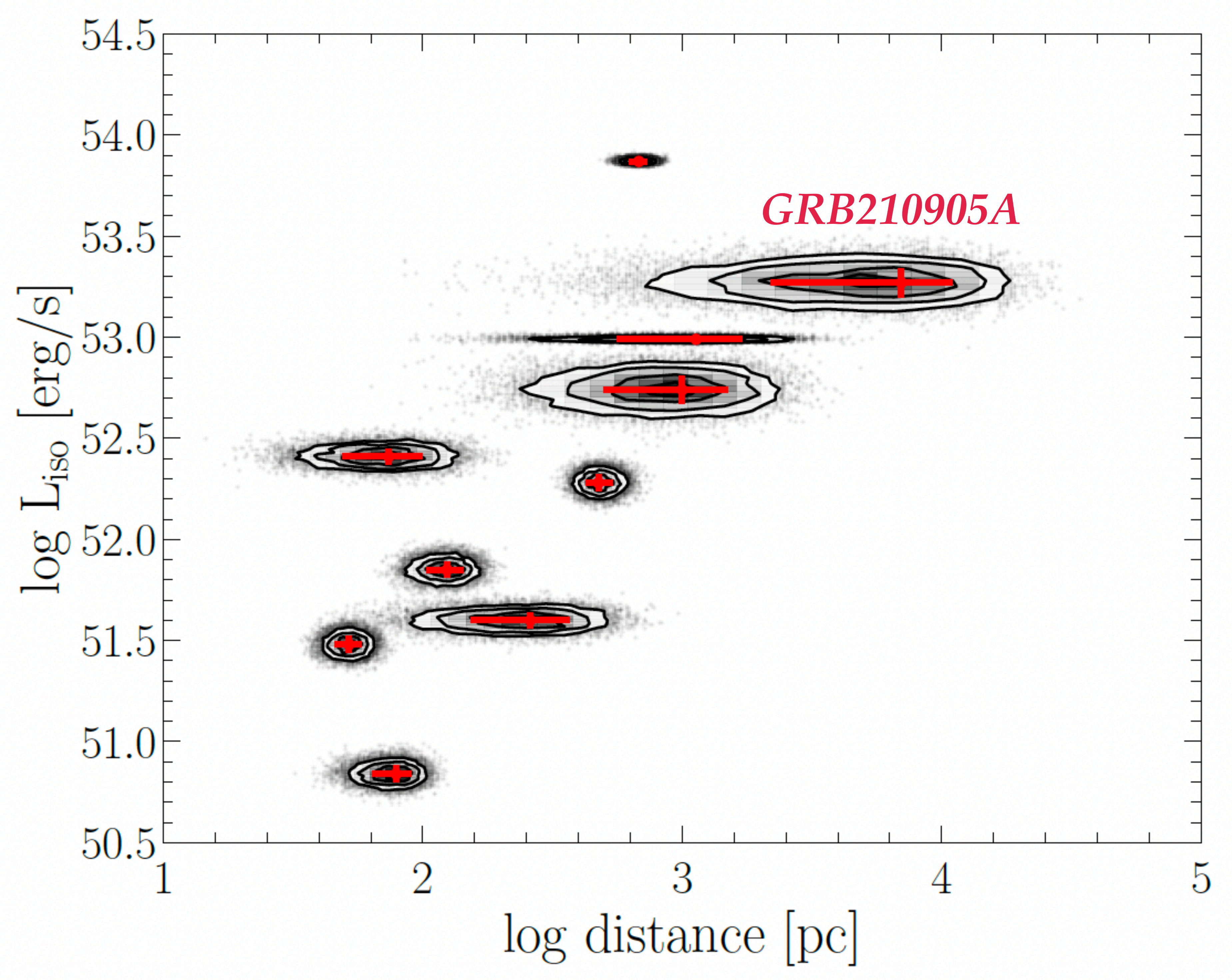

A. Saccardi, S.D. Vergani, A. De Cia et al. 2023

Backup Slides

Component IV:	$[Zn/Fe]_{fit}$	0
	Δv [km/s]	-25
	Proper Distance [kpc]	?

$[Zn/Fe]_{fit}$	0	0	0.53	0.53	0.57	
Δv [km/s]	-255	+46	+75	-203	-136	
Proper Distance [kpc]	?	17	16	11	7	
Component	I	V	VI	II	III	GRB

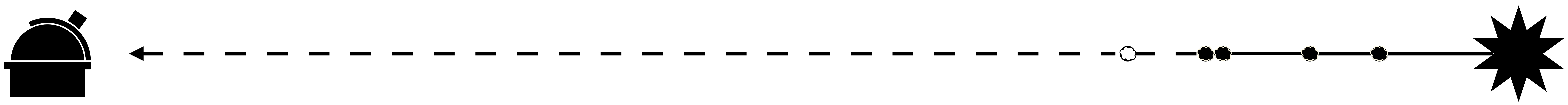

1 kpc

A. Saccardi, S.D. Vergani, A. De Cia et al. 2023

Backup Slides

Credits: Rossi et al. 2022

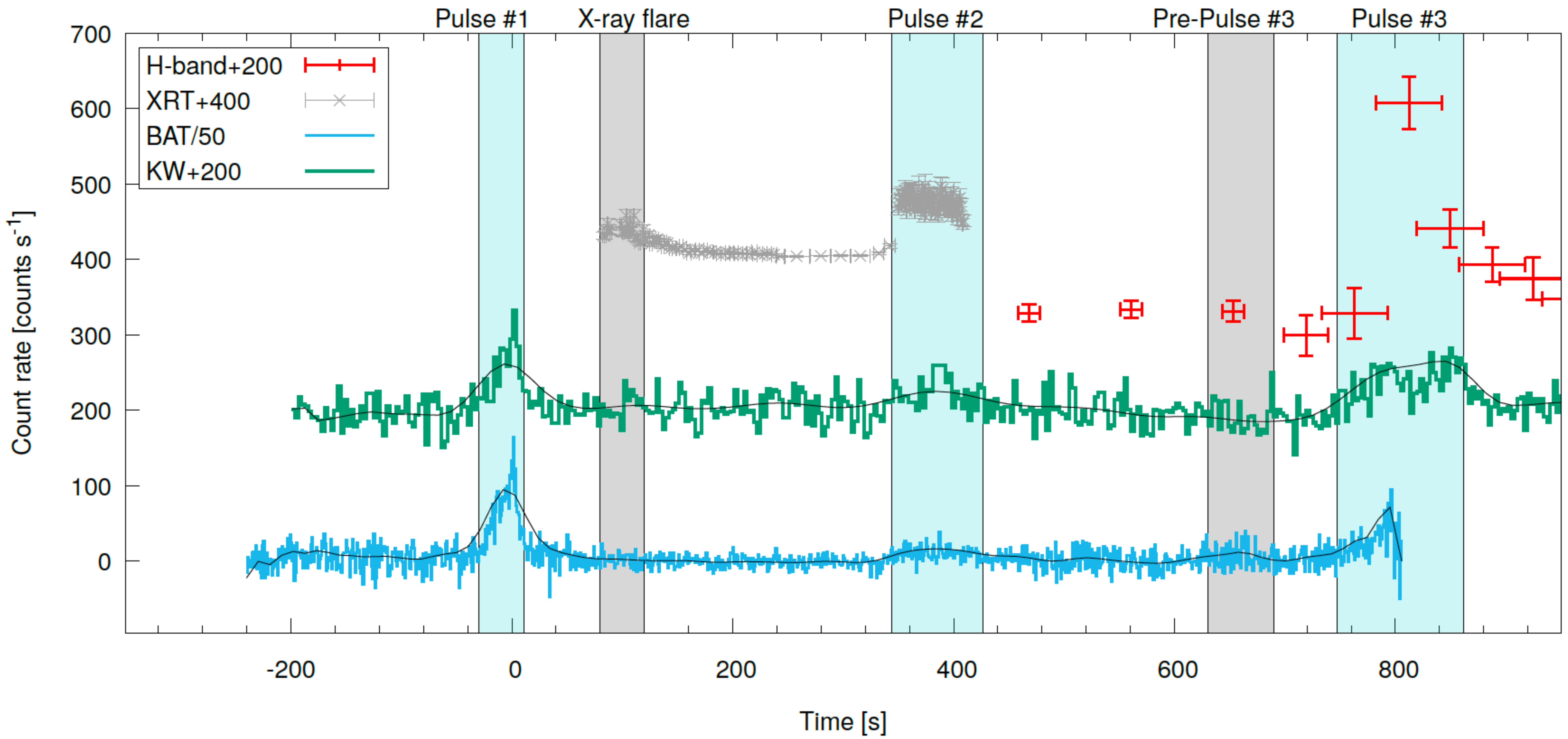

Fig. 1. Multi-band prompt emission light curve of GRB 210905A. The light curve of GRB 210905A as seen by *Swift*/BAT (15–350 keV, 6 s binning, count rate/50, cyan), Konus-*Wind* (20–400 keV, 5.888 s binning, count rate+200, green points), *Swift*/XRT (0.3–10 keV, count rate+400, grey points) and REM (flux density+200 in units of 0.1 Jy, red points). The evolution of the gamma-ray emission is highlighted with a black smoothed spline to guide the eye. The intervals corresponding to the three main and two smaller pulses are highlighted by turquoise- and grey-shaded areas, respectively.

Backup Slides

Credits: Rossi et al. 2022

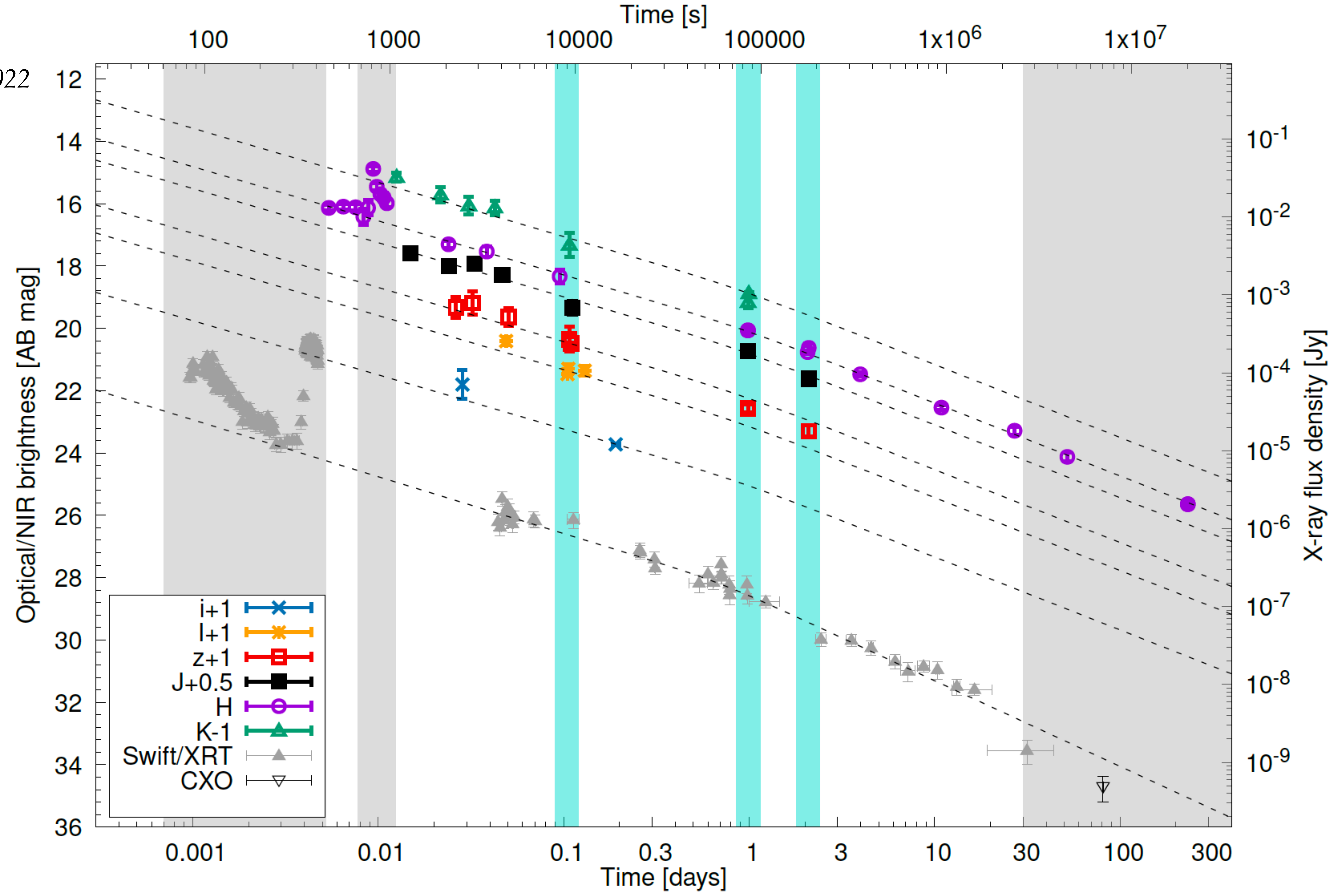

Backup Slides

Credits: Rossi et al. 2022

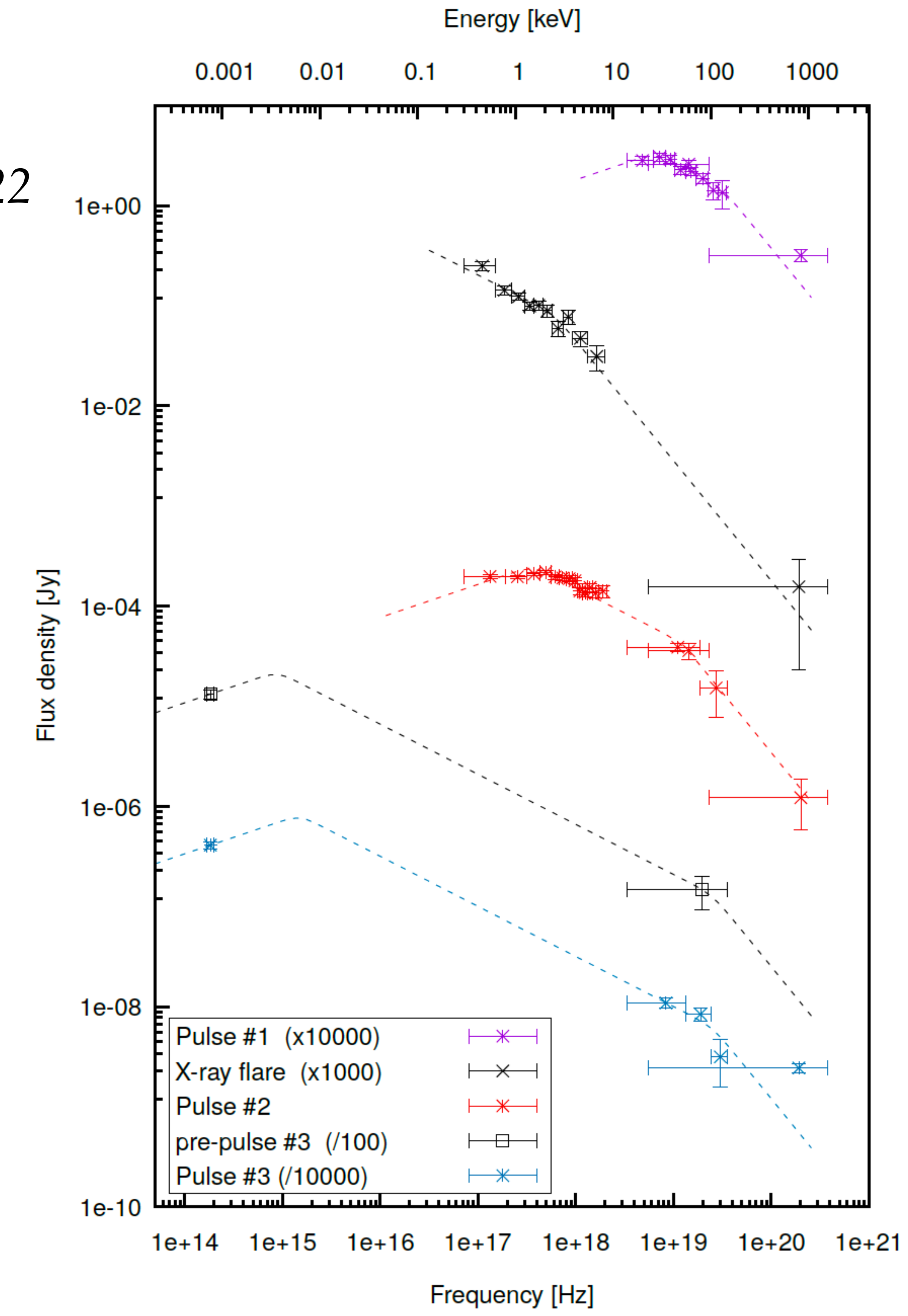

Fig. 2. Optical/NIR to gamma-ray SEDs of the prompt phase at five different epochs (see Sect. 3.2). All SEDs have been modelled with a double broken power-law following the expectations from synchrotron theory. Note that we could not constrain the low-energy break during the X-ray flare. In the fourth SED, we have simply scaled the solution from the last epoch (there is no KW detection during this epoch). Note that the photon indices described in the text correspond to spectral indices 1/3, −1/2, −1.3 shown here. X-ray data are corrected for Galactic and intrinsic absorption.

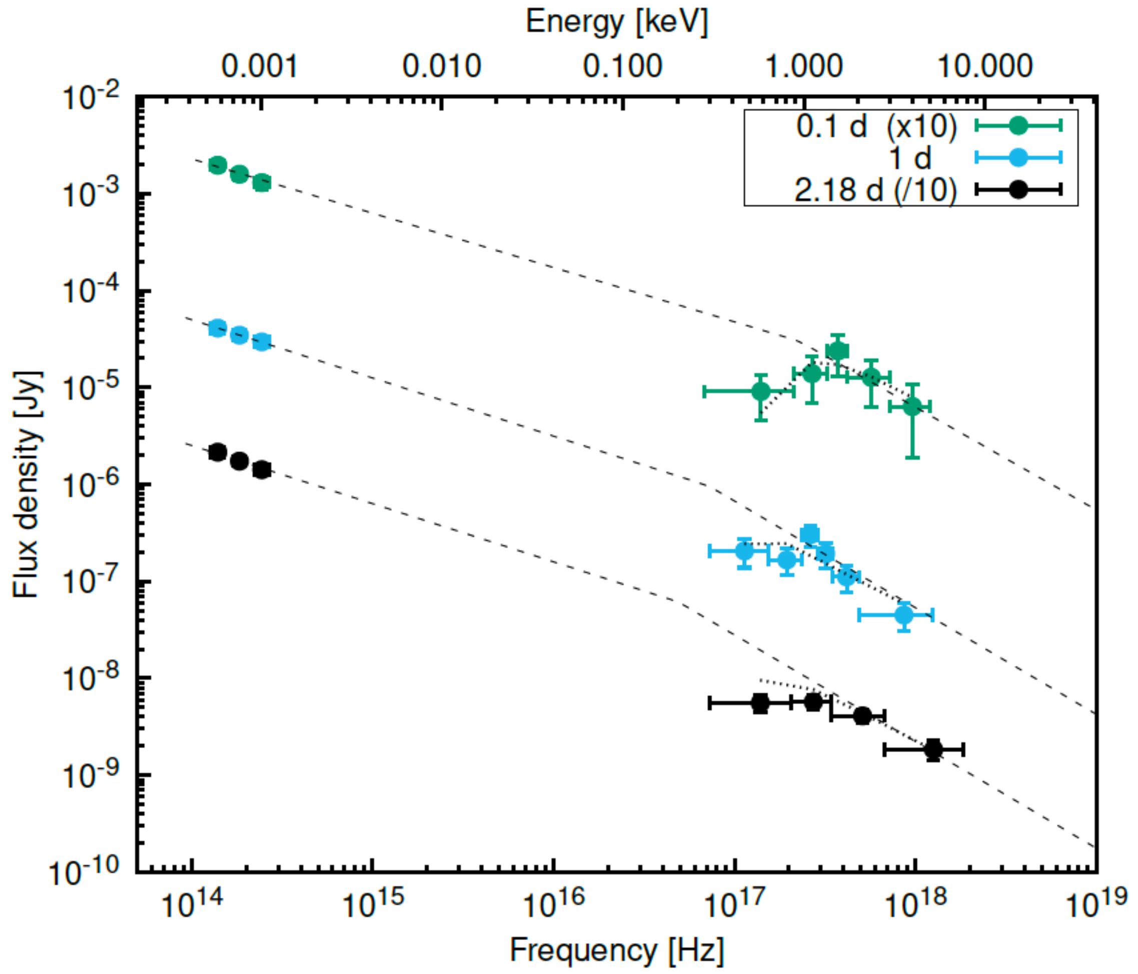

Fig. 4. Optical/NIR to X-ray SEDs of GRB 210905A at three different epochs (0.1, 1.0, 2.18 d). The best fit with a broken power-law is shown in all three epochs, and the best-fit parameters are shown in Table 3 (see Sect. 3.3). The dotted- and dashed-lines show the absorbed and unabsorbed models, respectively.

Backup Slides

Credits: Rossi et al. 2022

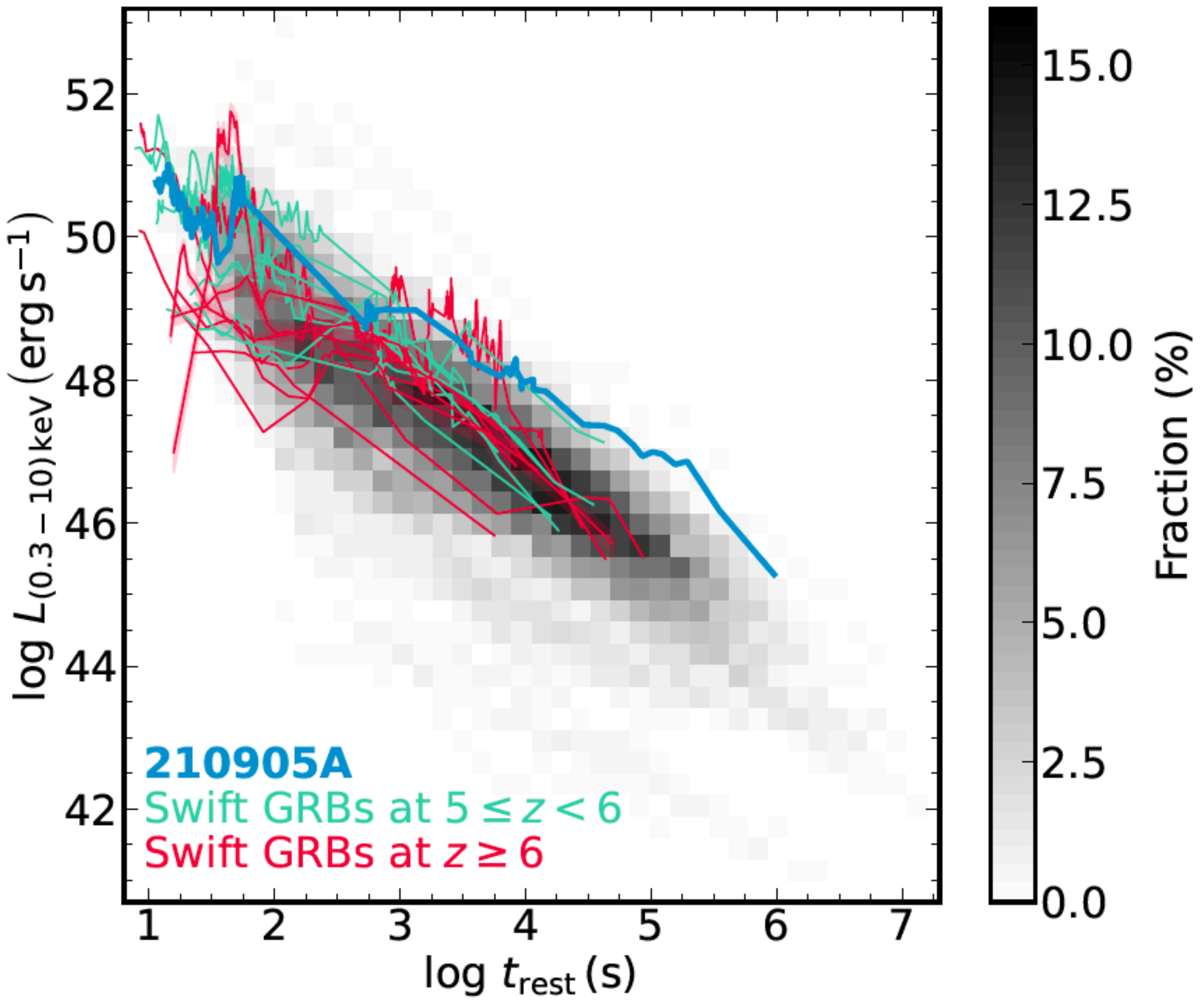

Fig. 9. X-ray afterglow of GRB 210905A (blue line) in the context of other high-redshift GRBs (green and red) and the world-sample of *Swift* GRBs with known redshifts (grey density plot). The afterglow of GRB 210905A is the most luminous after 10 ks among all $z > 5$ GRBs and one of the most luminous in general. The colour table on the right side translates a grey shade at a given luminosity and time into a fraction of bursts.

Backup Slides

Credits: Rossi et al. 2022

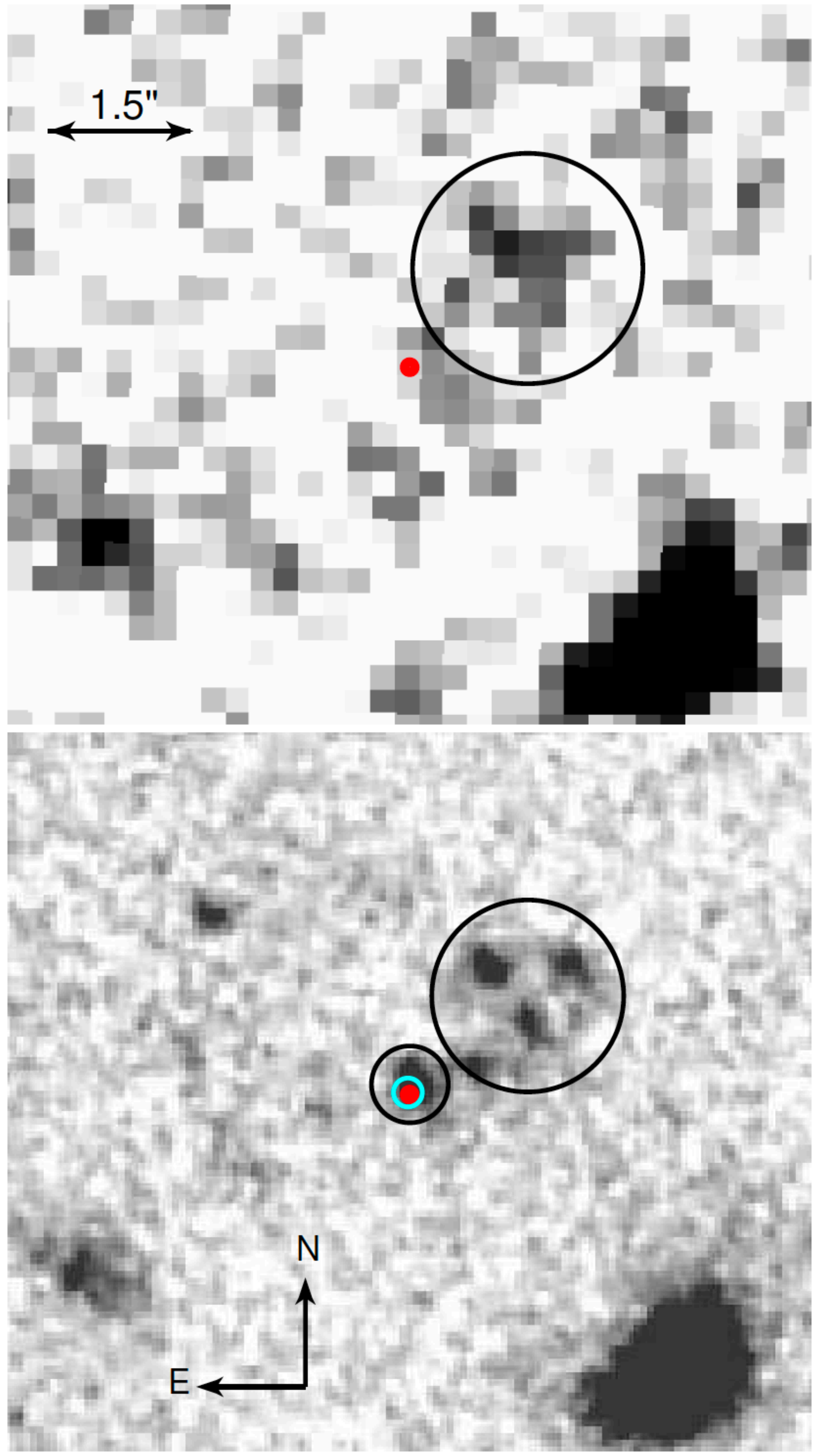

GRB 240218A

Backup Slides

Credits: Saccardi et al submitted

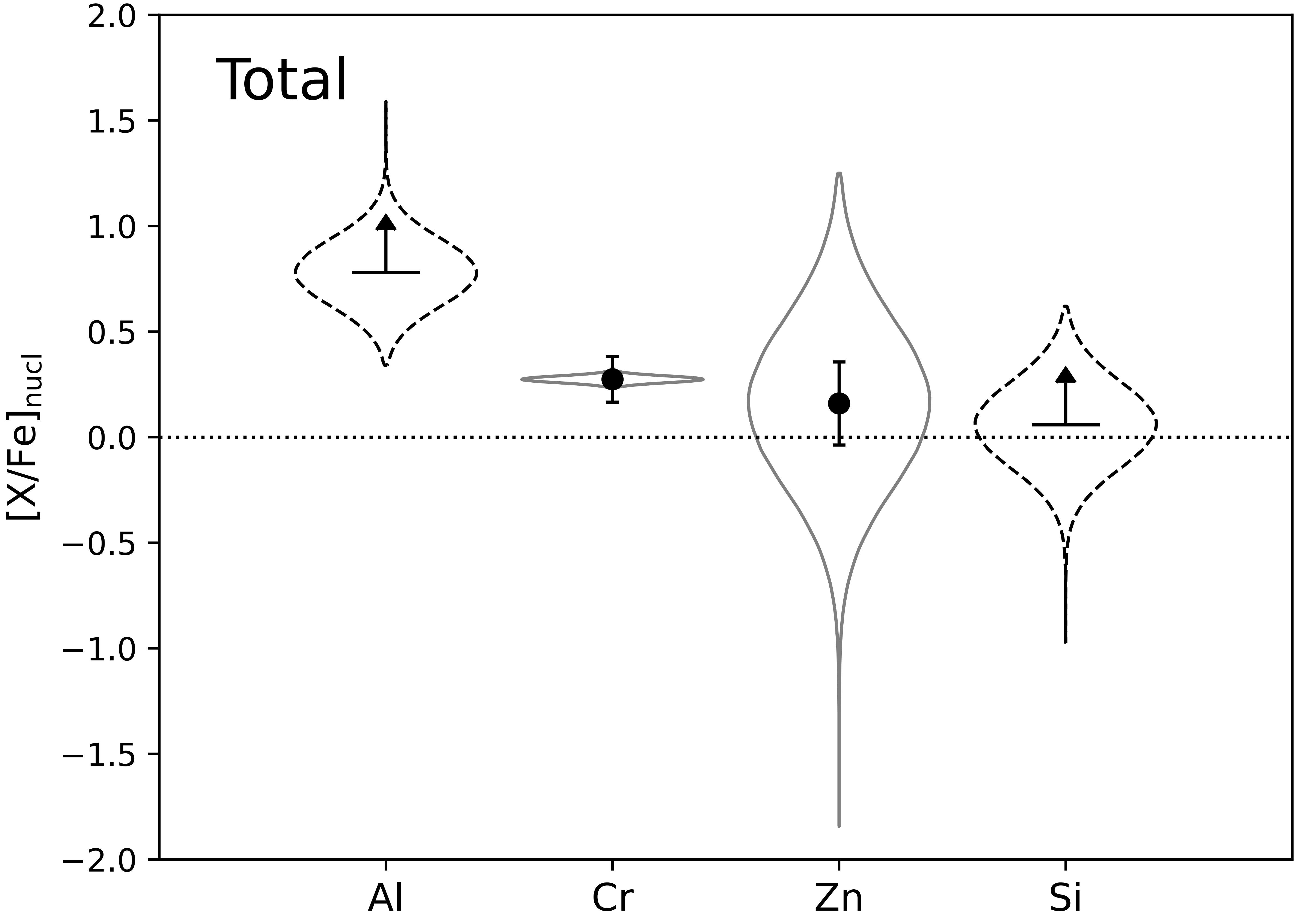

Backup Slides

Credits: Saccardi et al submitted

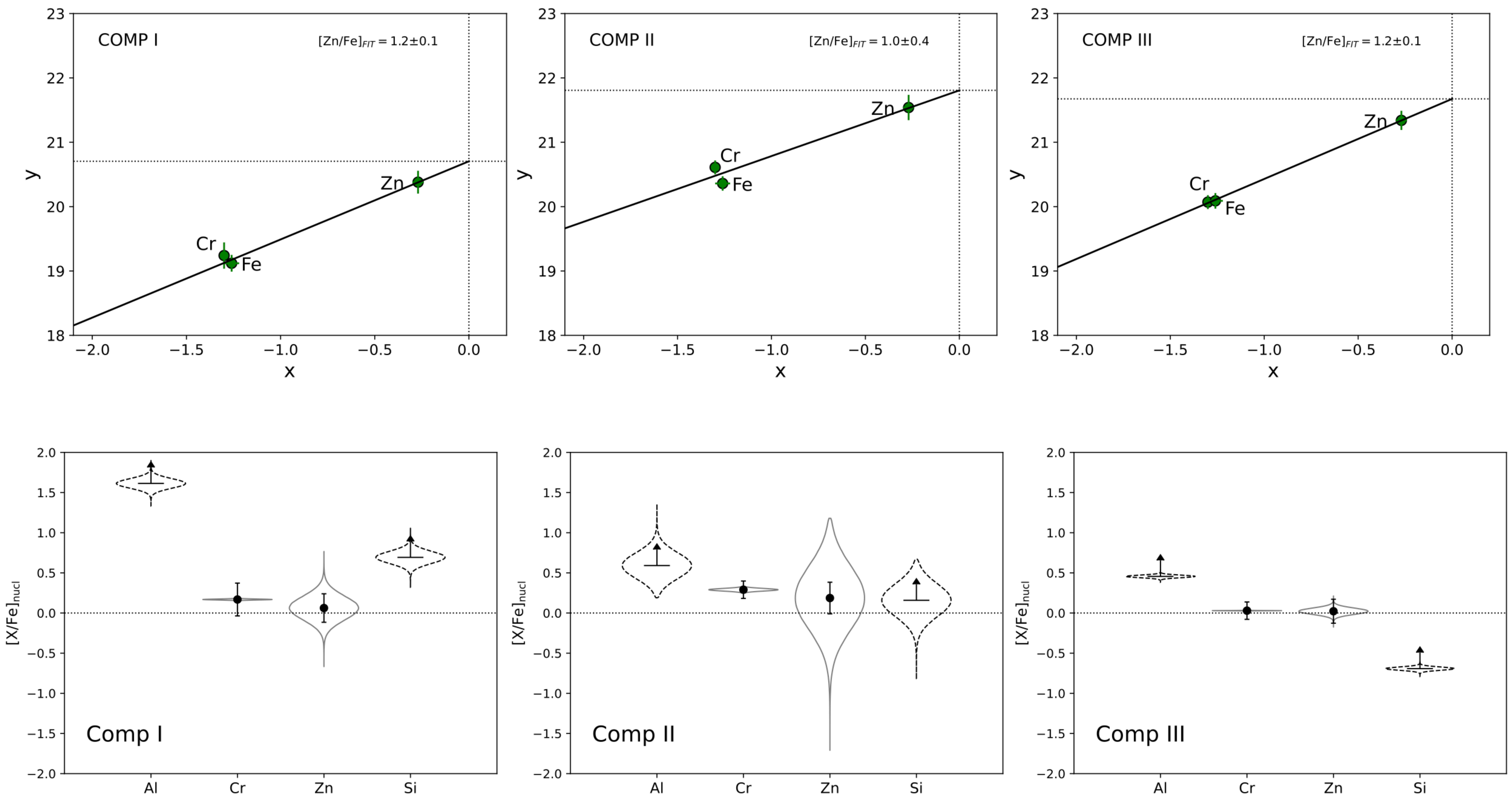

Backup Slides

Credits: Saccardi et al submitted

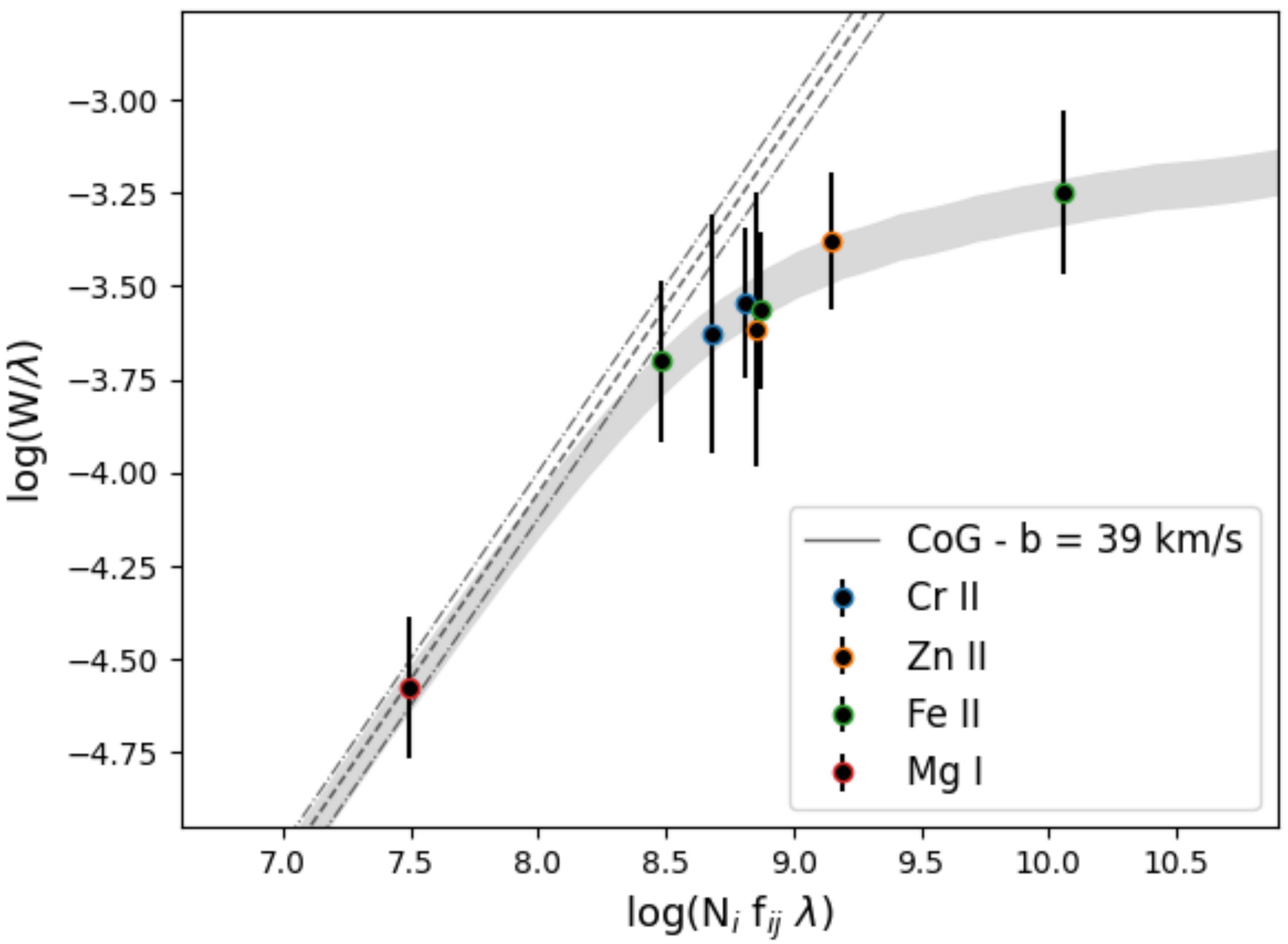

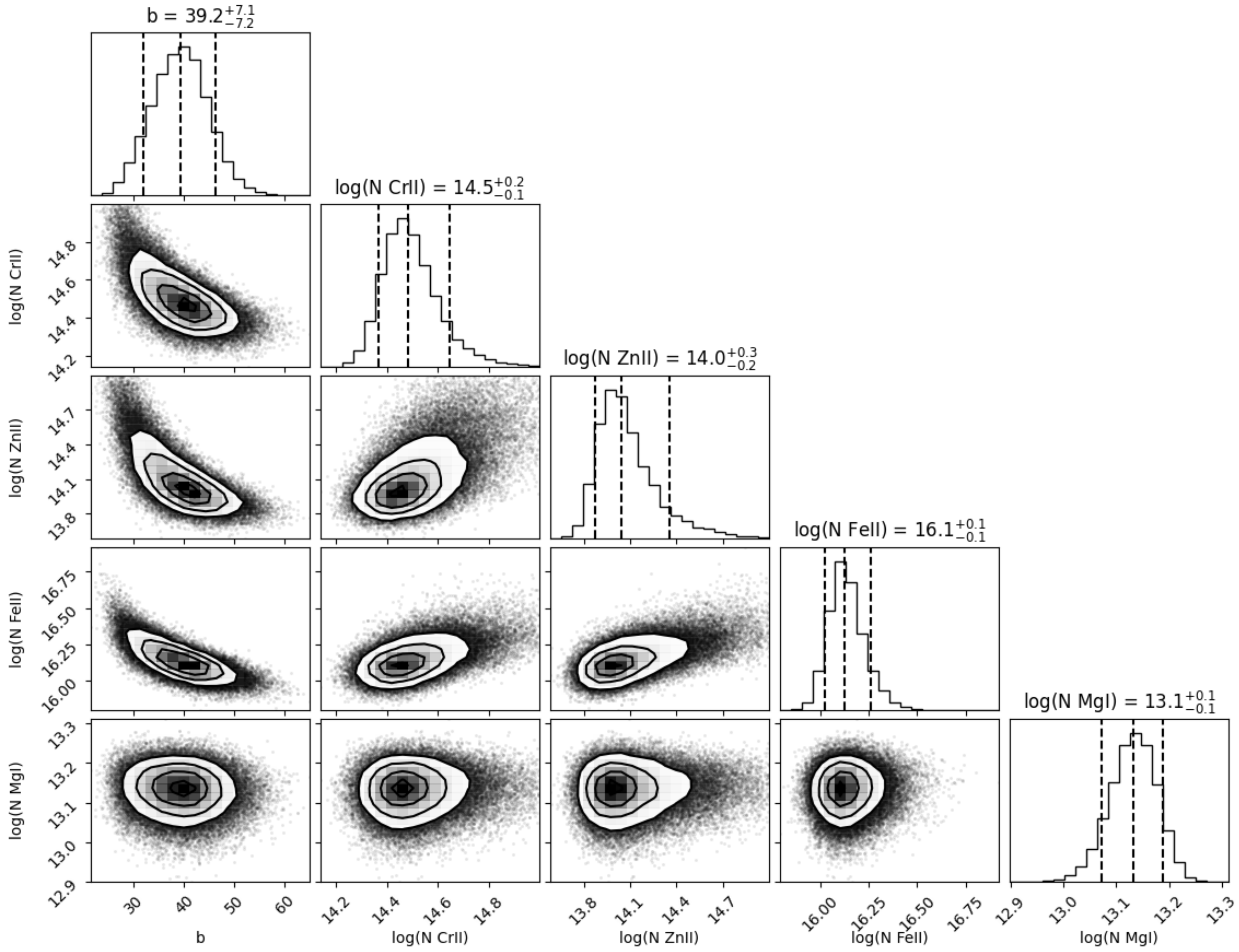

Backup Slides

Credits: Saccardi et al submitted

X	$\log(N/\mathrm{cm}^{-2})$	[X/H]	[X/Fe]
Al	> 15.3	> -1.7	$[> 0.3]$
Zn	$> 14.3\,[14.3 \pm 0.2]$	$[-0.8 \pm 0.4]$	$[1.2 \pm 0.2]$
Si	> 16.6	> -1.4	$[> 0.6]$
Fe	$> 16.0\,[16.0 \pm 0.1]$	$[-1.9 \pm 0.3]$	
Cr	$> 14.5\,[14.5 \pm 0.1]$	$[-1.6 \pm 0.3]$	$[0.3 \pm 0.1]$

Species	*I*	*II*	*III*
	$-200\,\mathrm{km\,s^{-1}}$	$0\,\mathrm{km\,s^{-1}}$	$+50\,\mathrm{km\,s^{-1}}$
Al II $\lambda1670$	> 14.7	> 15.0	> 14.5
Zn II $\lambda2026, \lambda2062$	12.9 ± 0.2	$> 14.1\,[14.1 \pm 0.2]$	$> 13.9\,[13.9 \pm 0.1]$
Cr II $\lambda2056, \lambda2062$	13.0 ± 0.2	$> 14.4\,[14.4 \pm 0.1]$	$> 13.8\,[13.8 \pm 0.1]$
Si II $\lambda1526$	> 15.9	> 16.5	> 15.5
Fe II $\lambda1608, \lambda1611, \lambda2260^{\ddagger}$	14.6 ± 0.1	$> 15.8\,[15.8 \pm 0.1]$	$> 15.6\,[15.6 \pm 0.1]$
Fe II* $\lambda2612$ (1s)	< 13.3	13.8 ± 0.1	12.6 ± 0.4
Fe II* $\lambda1613, \lambda1702$ (5s)		14.5 ± 0.1	13.8 ± 0.3
Si II* $\lambda1533$	< 12.4	> 14.8	> 15.1
Ni II* $\lambda2166, \lambda2217, \lambda2223$	< 12.9	14.2 ± 0.1	13.3 ± 0.1
Al III $\lambda1854, \lambda1862^{\dagger}$	13.3 ± 0.2	> 14.1	> 13.2
$b\,(\mathrm{km\,s^{-1}})^{*}$	34 ± 4	27 ± 4	21 ± 4

Element	Transition	Observed Wavelength [Å]	Equivalent Width (EW_r) [Å]
Fe II	1608	12517.22	0.91 ± 0.09
Fe II	1611	12538.63	0.32 ± 0.03
Fe II	2260	17593.76	0.62 ± 0.07
Zn II	2026	15768.40	0.90 ± 0.08
Zn II	2062	16048.32	0.50 ± 0.09
Cr II	2056	16001.72	0.58 ± 0.06
Cr II	2062	16051.65	0.49 ± 0.08
Mg I	2026	15770.37	0.05 ± 0.01

Species	1	2	3
	$-200\,\mathrm{km\,s^{-1}}$	$0\,\mathrm{km\,s^{-1}}$	$+140\,\mathrm{km\,s^{-1}}$
C IV $\lambda1548, \lambda1550^{\S}$	> 14.7	> 15.7	> 15.8
Si IV $\lambda1393, \lambda1402^{\S}$	> 14.3	> 15.2	> 13.7
$b\,(\mathrm{km\,s^{-1}})$	38 ± 4	44 ± 4	17 ± 4

Backup Slides

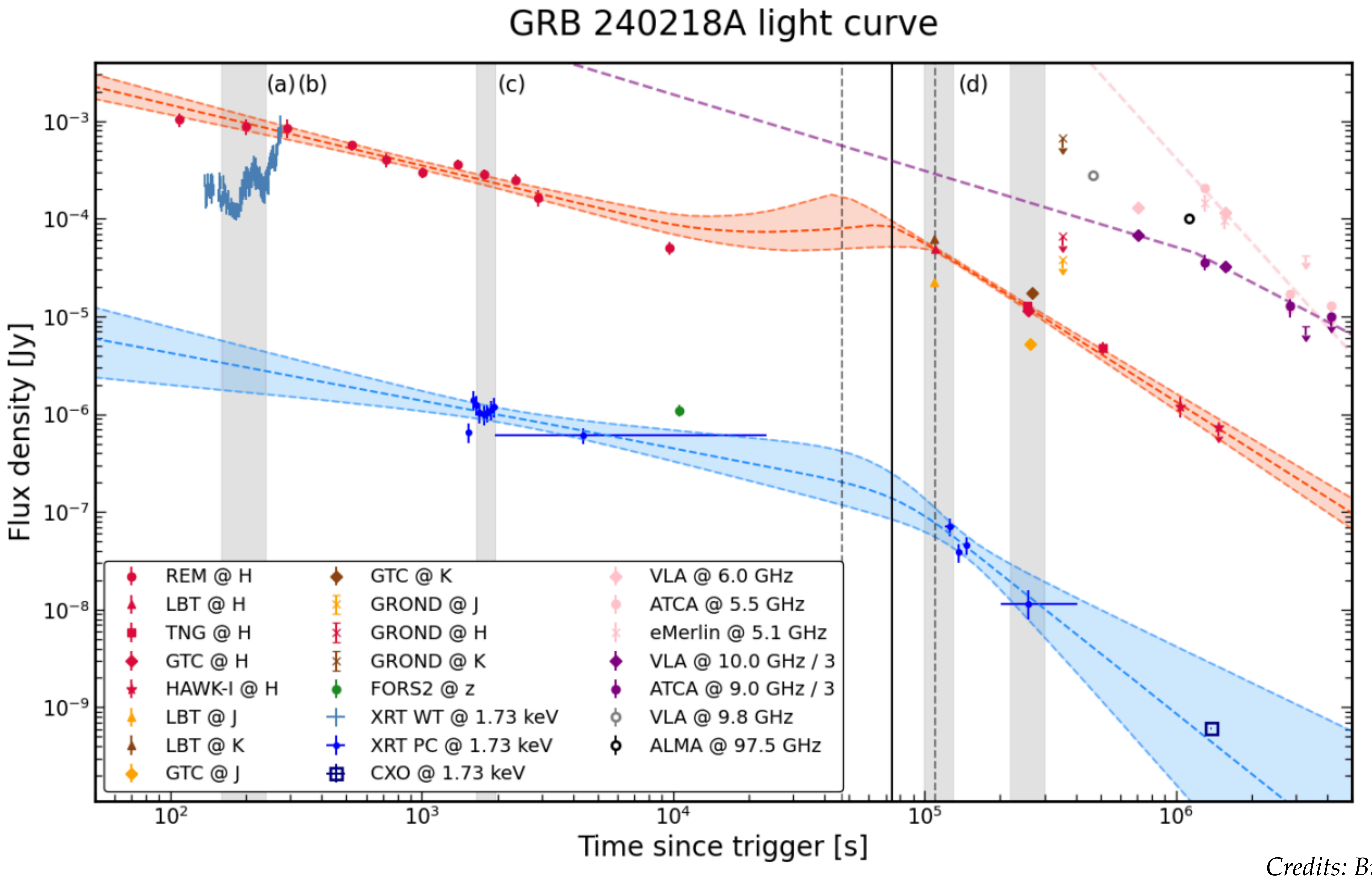

Credits: Brivio et al. 2025

Backup Slides

Credits: Saccardi et al submitted

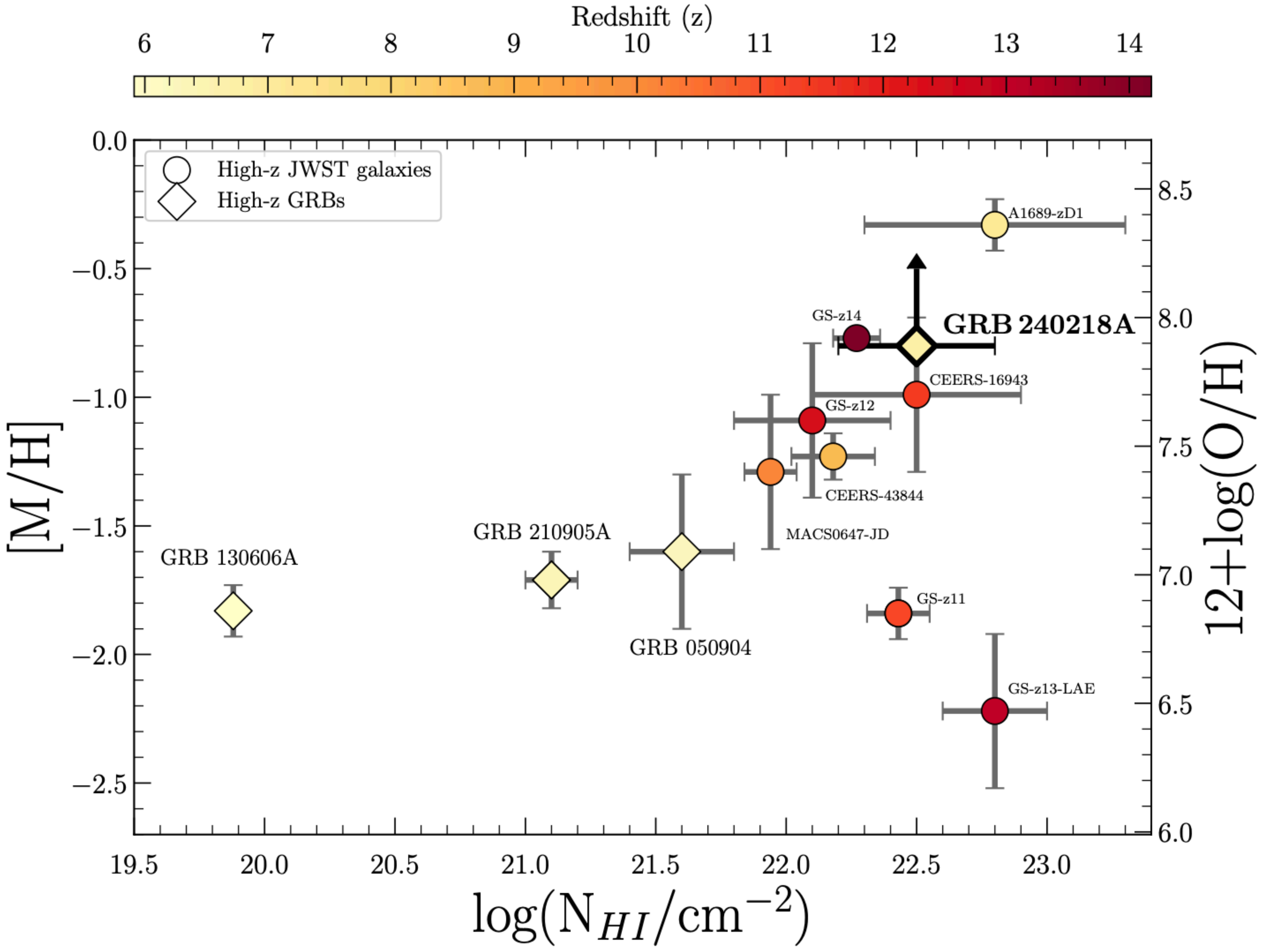

Backup Slides

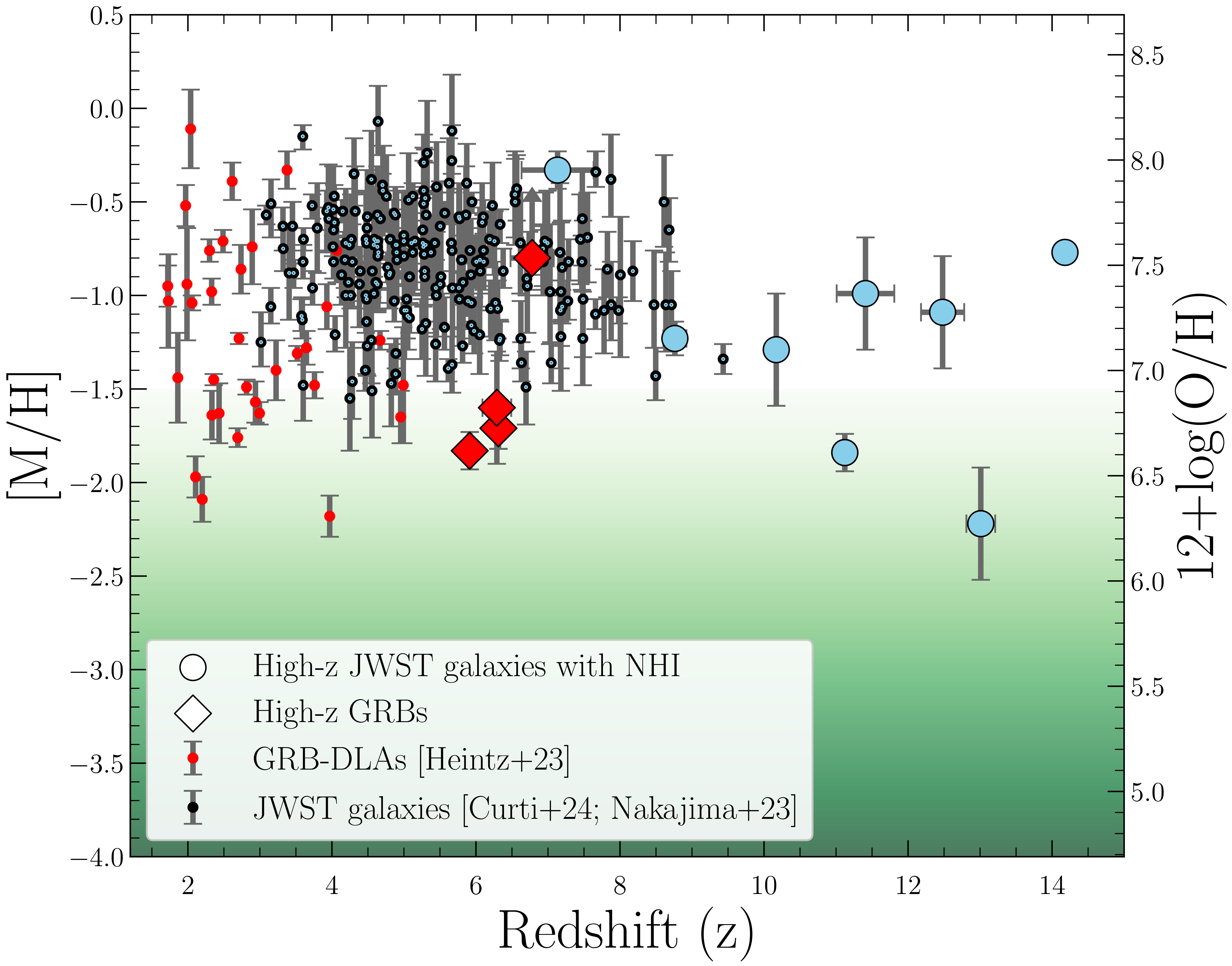

EP 240315a

Backup Slides

The fast X-ray transient EP240315a: a z ~ 5 gamma-ray burst in a Lyman continuum leaking galaxy

@Nature Astronomy - A. J. Levan, P. Jonker, **A. Saccardi**, et al.

Submitted

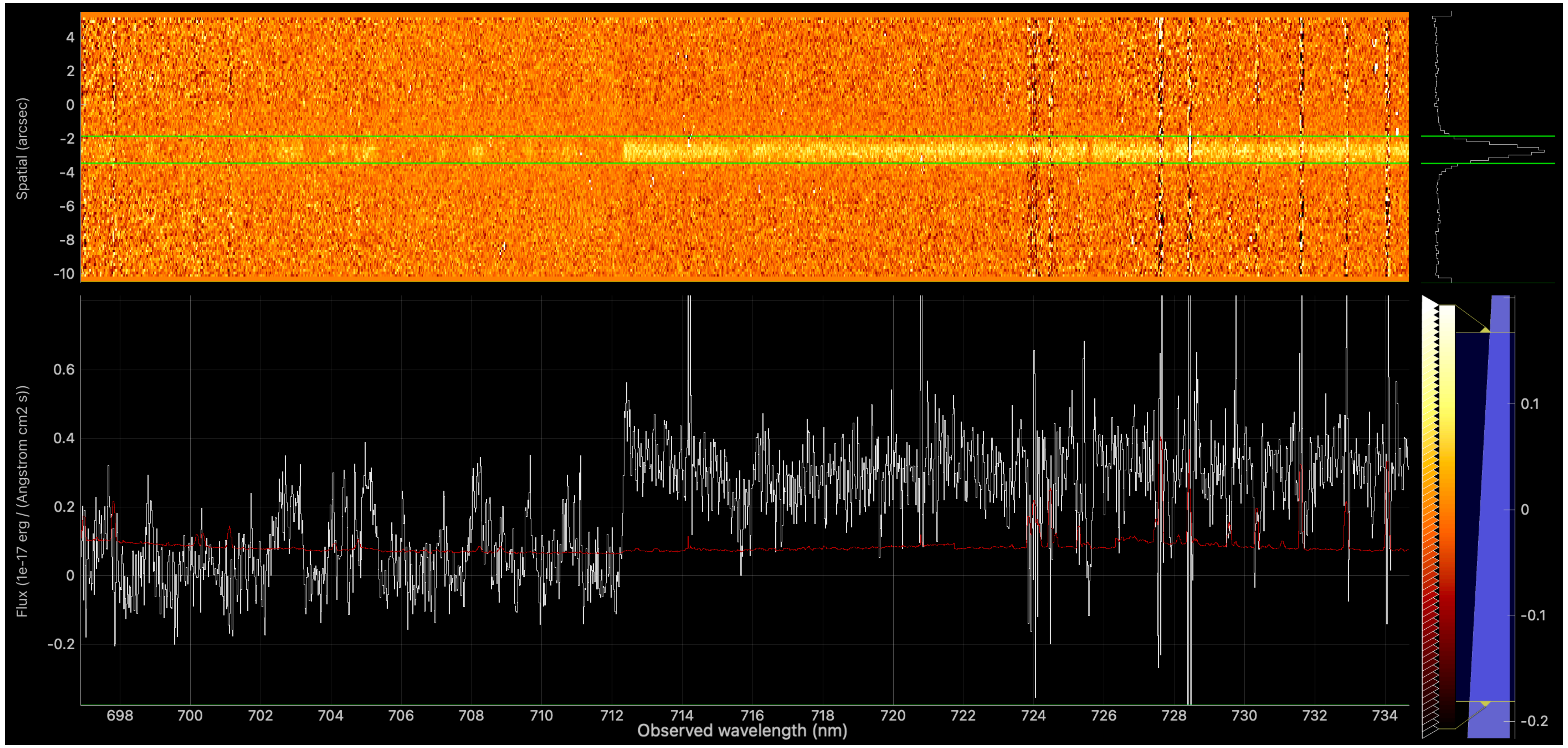

Credits: Stargate/A. Saccardi

Backup Slides

A. J. Levan, P. Jonker, A. Saccardi, et al. submitted

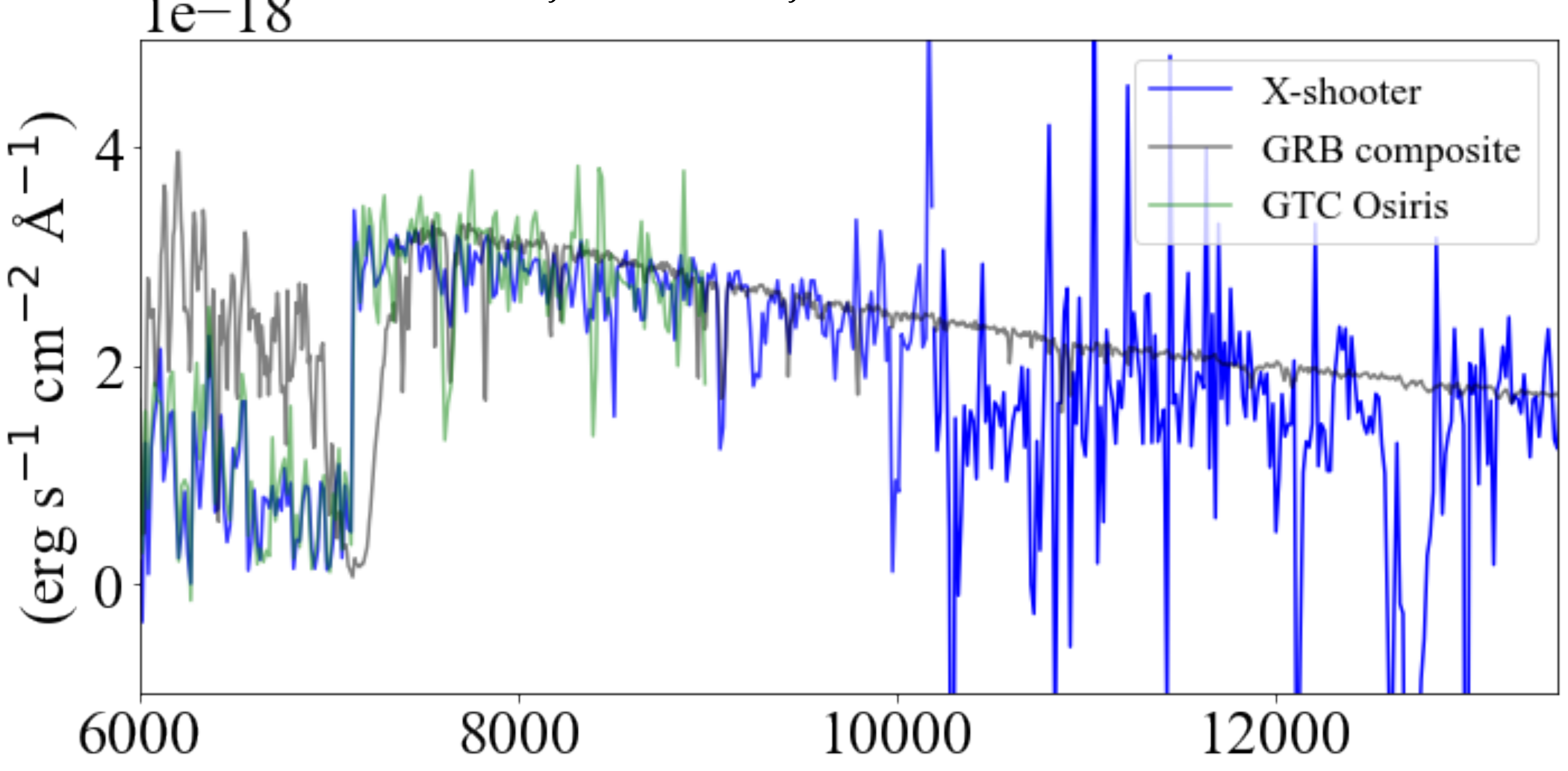

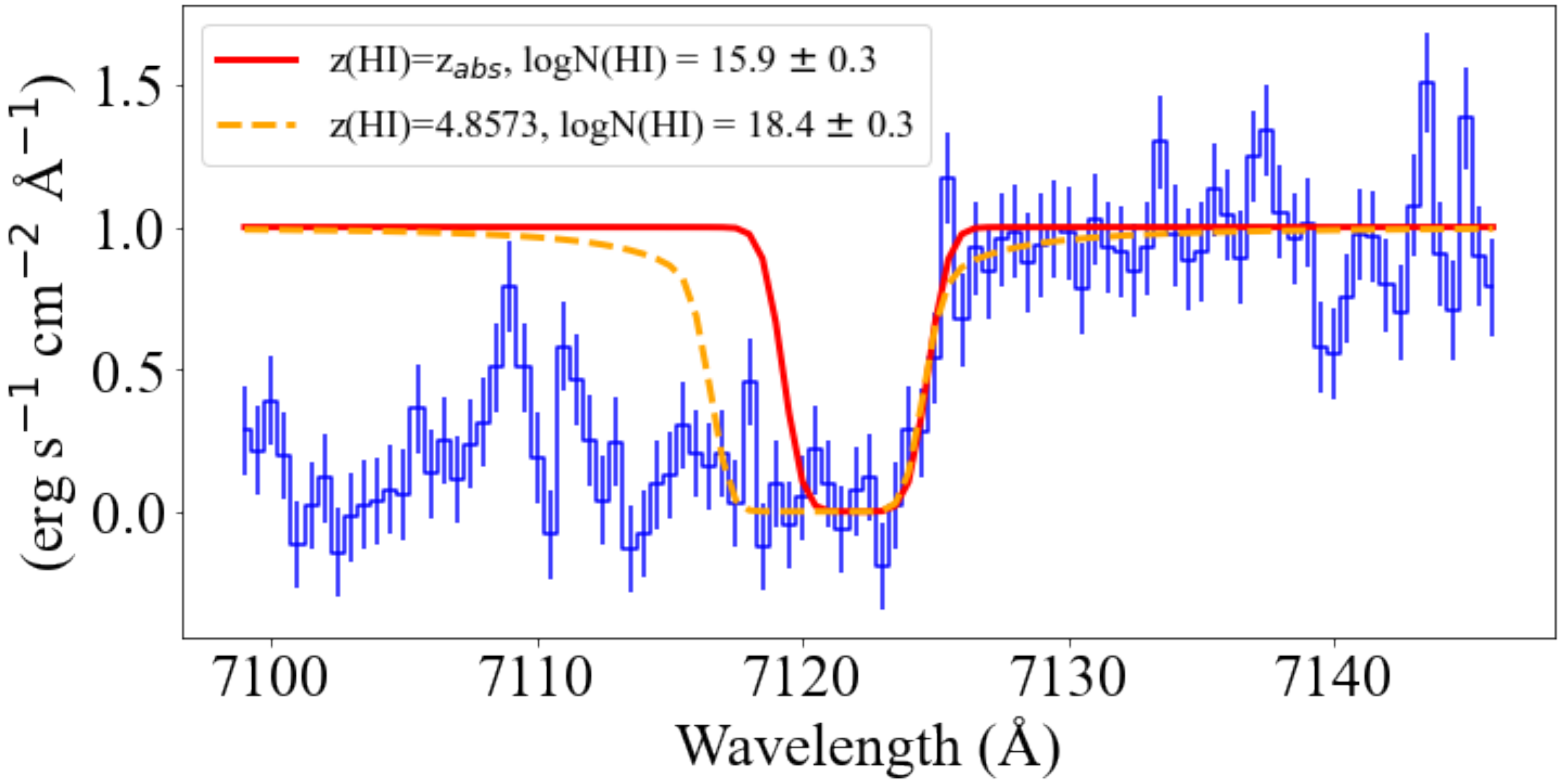

z = 4.859

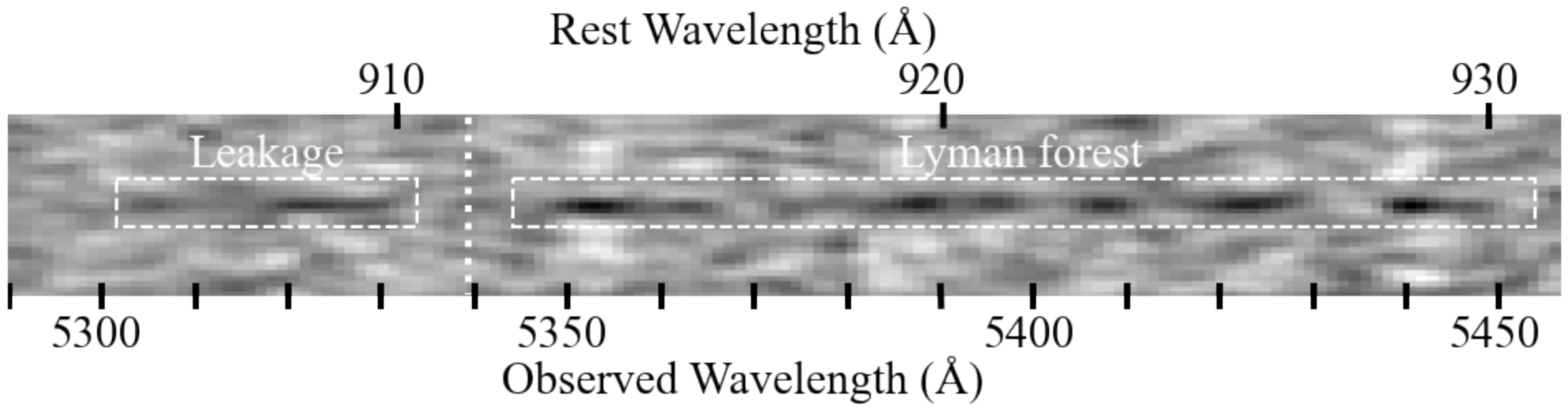

A. J. Levan, P. Jonker, A. Saccardi, et al. submitted

A low column density of neutral hydrogen indicating that the event is embedded in a low-density environment, further supported by direct detection of leaking ionising Lyman-continuum.

Backup Slides

A. J. Levan, P. Jonker, A. Saccardi, et al. submitted

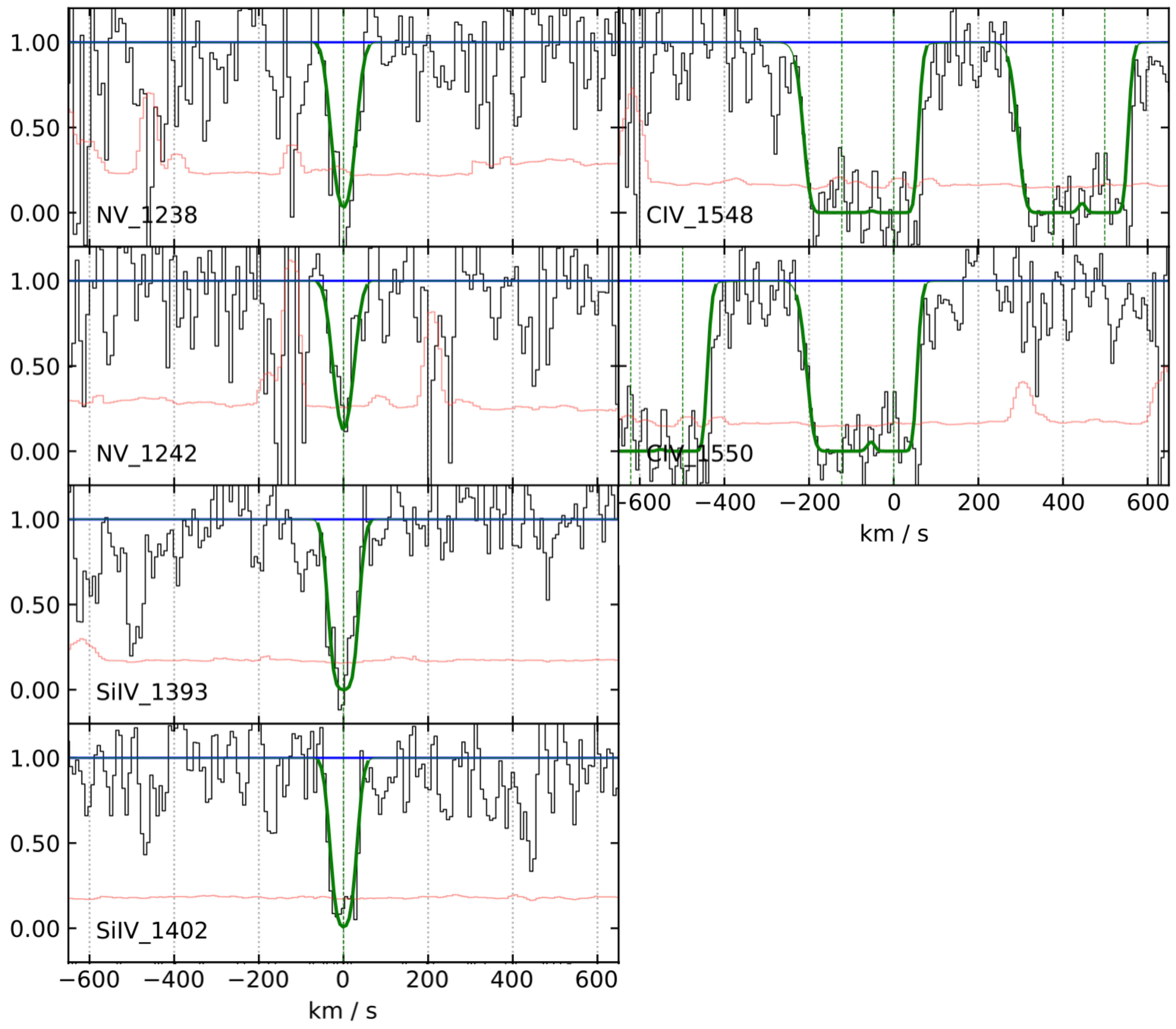

A. J. Levan, P. Jonker, A. Saccardi, et al. submitted

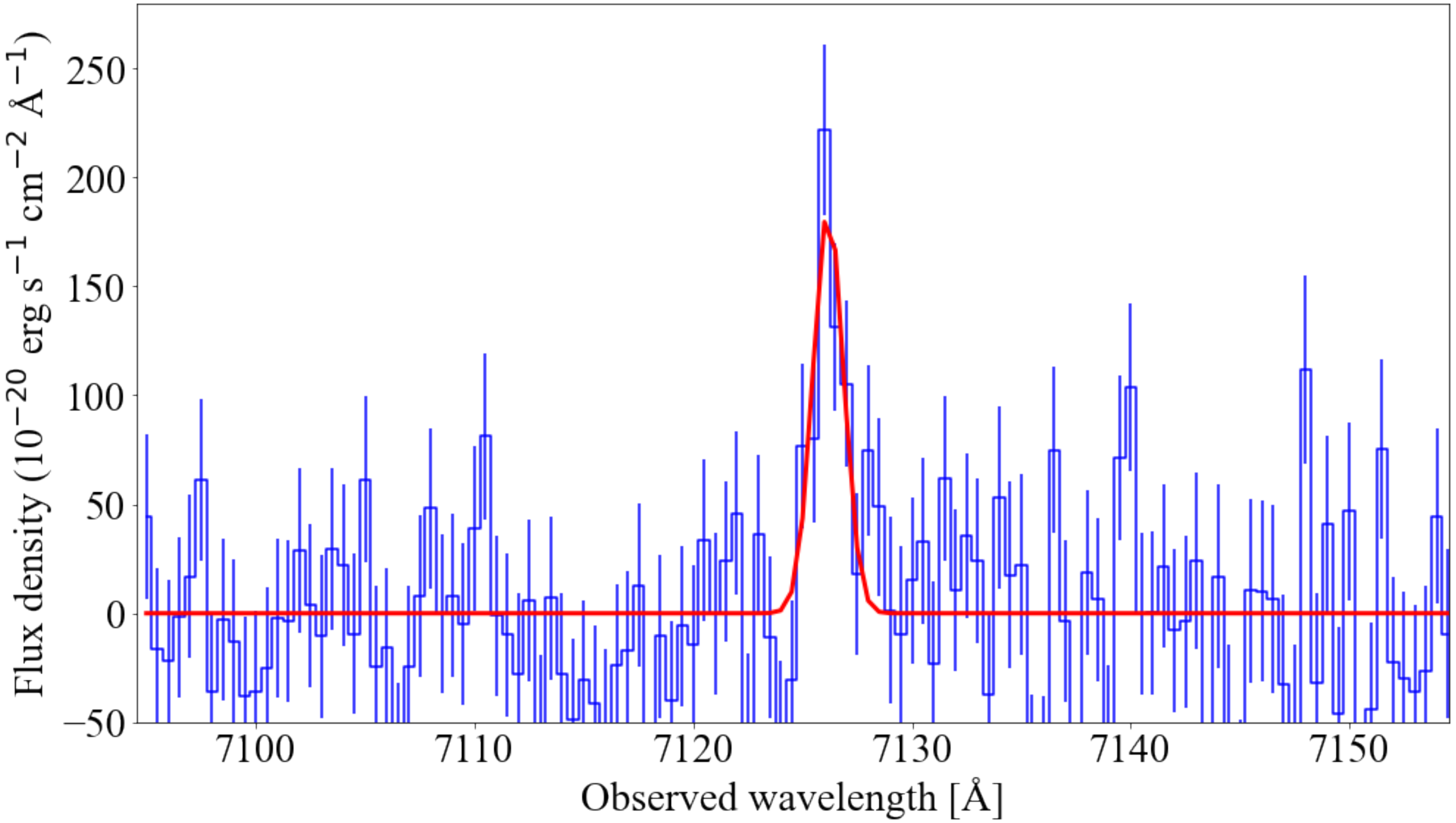

Absence of low-ionisation transitions (we only detected high-ionisation transitions e.g. NV, SiIV, CIV)
Tentative detection of Ly-a in Epoch 1 and confirmed by Epoch 2

Backup Slides

EP

EP carries a Wide-field X-ray Telescope (WXT) with a large instantaneous FoV, which adopts such a novel lobster-eye MPO technology. Complementary to this wide-field instrument is a Follow-up X-ray Telescope (FXT) with a large effective area and a narrow field-of-view.

FXT is a Wolter-I telescope operating in the 0.3-10 keV energy range. It has a narrow field of view (60 arcmin in diameter) and a source localization error of 5-15 arcsec.

The FXT is responsible for the quick follow-up observations (within 5 minutes) of the triggered sources from WXT, and will also observe other interested targets during the all sky survey at the rest time

WXT consists of 12 identical modules with 375 mm focal length, each covering about 300 square degrees. The 12 modules make a total un-vignetted FoV of WXT of about 3600 square degrees (~1.1 steradian).

WXT has a moderate angular resolution of FWHM ~ 5 arcmin and positioning accuracy of 1 arcmin (90%) in the 0.5 - 4 keV energy band.

SVOM

Backup Slides

SVOM

GOAL: boost to 50/60% the fraction of GRBs with redshift determination and enhance the number of high-z GRBs

Launch 22 June 2024

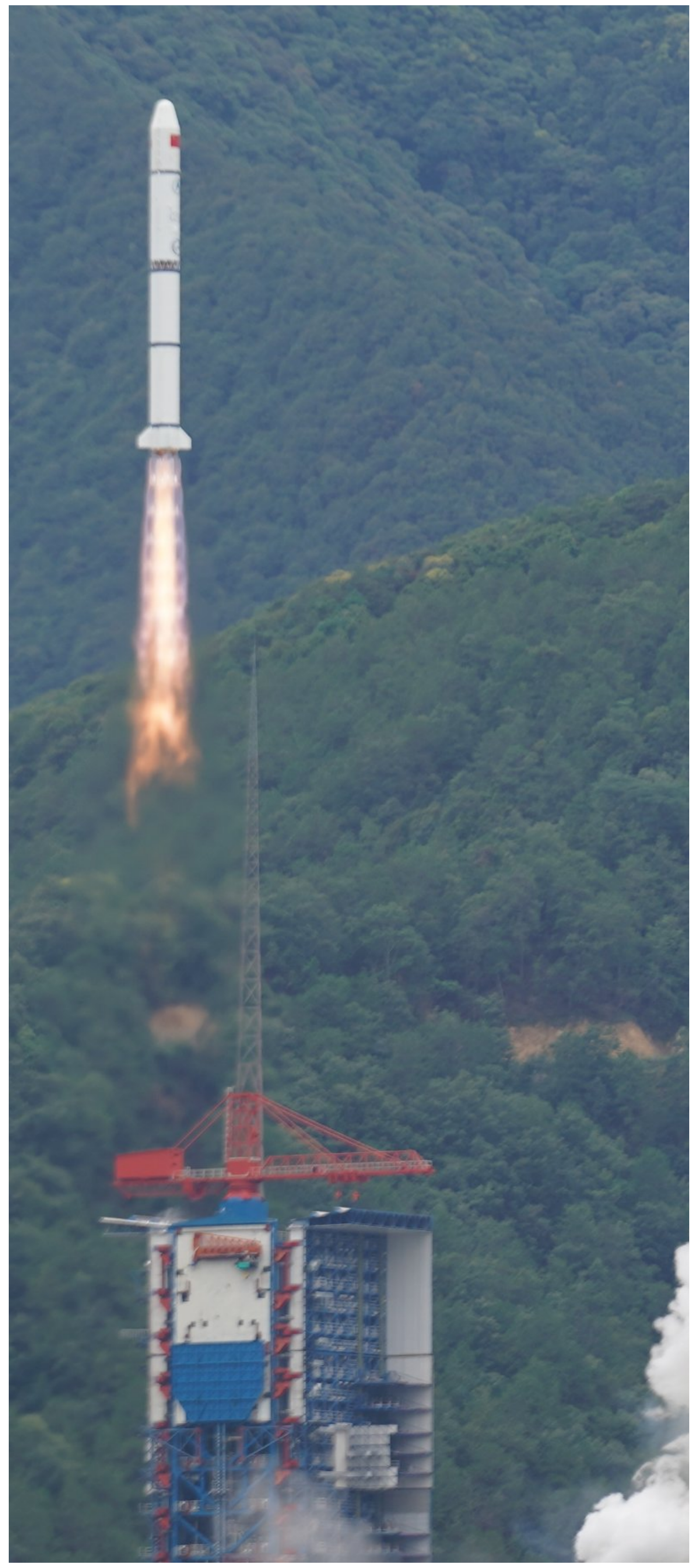

Credits: Chen Haojie, via Wu Lei sur X

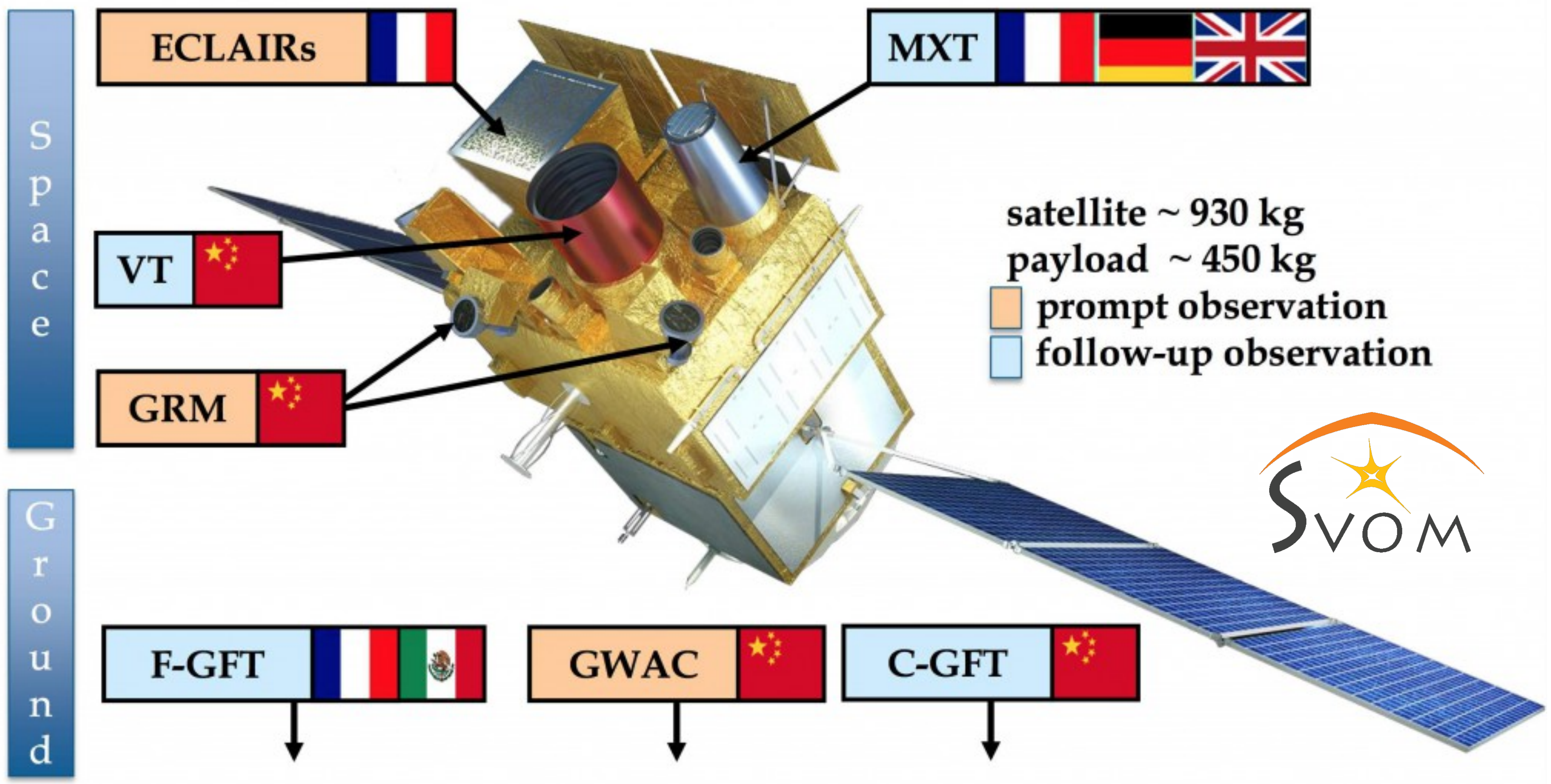

Credits: SVOM, *https://www.svom.eu/*

SVOM Payload

-γ-ray monitor GRM
(FoV ~ 5.6 sr; up to 5MeV)

-γ-ray telescope ECLAIRs
(< 12′; FoV ~ 2 sr; 4keV- 120keV)

-X-ray telescope MXT
(< 13″; 0.2–10 keV)

-Visible telescope **VT**
(~ 1″; 400–1000 nm)

SVOM Ground-based observation

Ground-based Wide Angle Camera (GWAC) and the robotic Ground Follow-up Telescopes, GFTs, French (F) and Chinese (C)

Overview of the onboard VHF alert sequence

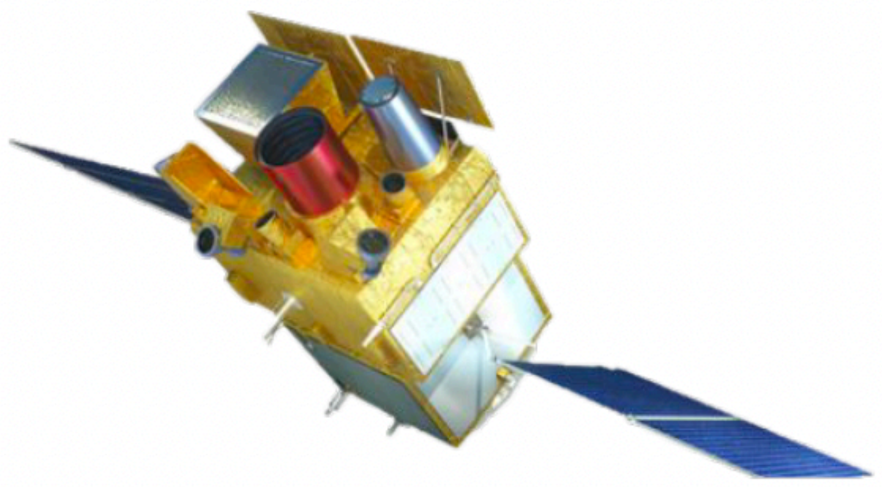

Potential alert seq.

1. GRM/ECLAIRs (no slew)
2. ECLAIRs/GRM (no slew)
3. GRM only (no slew)
4. GRM/ECLAIRs/MXT/VT (slew)
5. ECLAIRs/GRM/MXT/VT (slew)

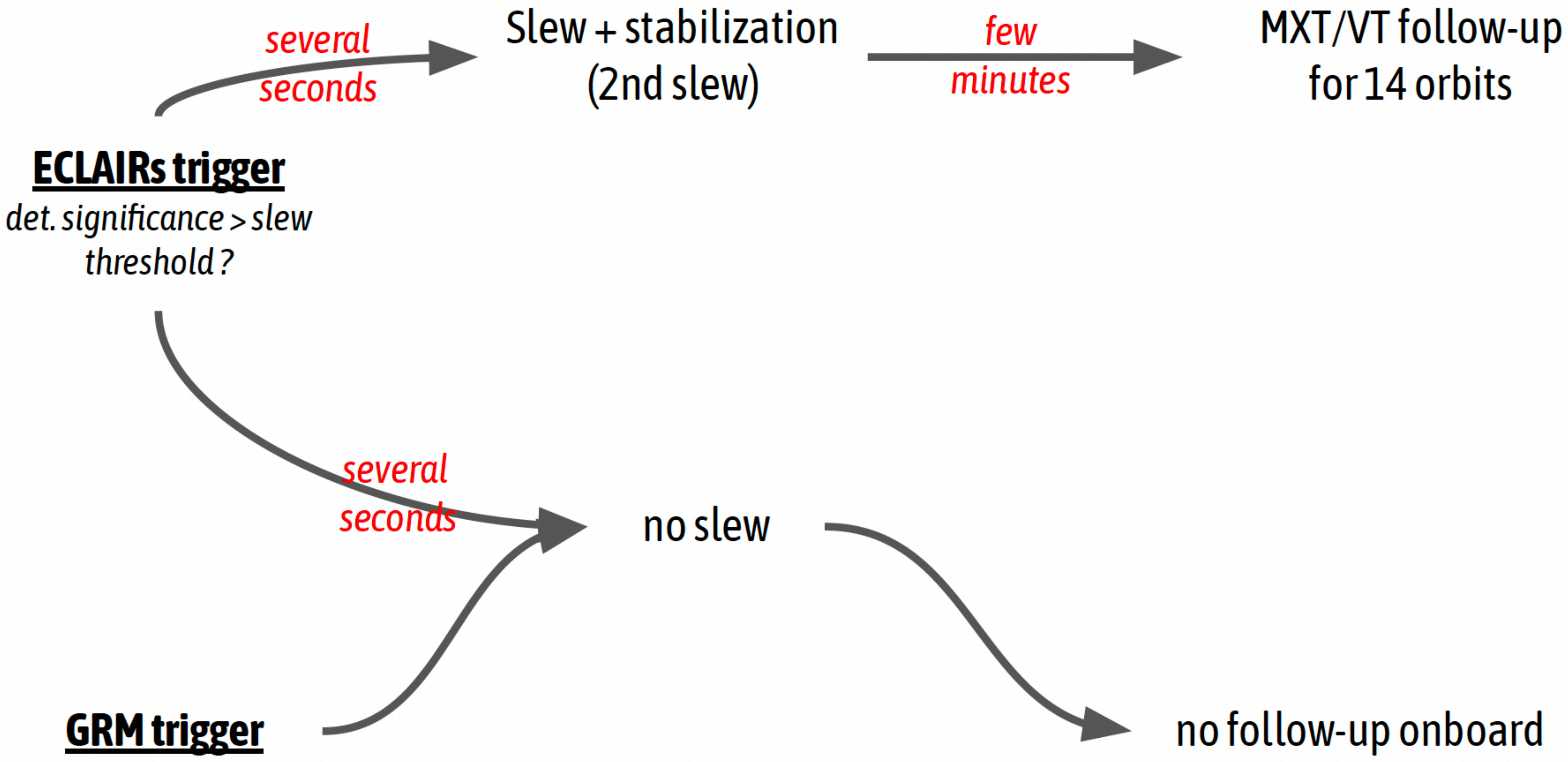

Credits: SVOM

Backup Slides

Table 1. Main requirements on COLIBRI

Observatory location	Observatorio Astronómico Nacional, San Pedro Mártir, Mexico
Delay for pointing	$<$ 30 seconds (goal: $<$ 20 seconds)
Precision of localization	$<$ 0.5 arcsec
Primary mirror diameter	1.3 m
Photometric channels	Three simultaneous arms: two in the visible (gri and zy) and one in the NIR (JH)
Field of view	26 arcmin
Pixel scale	0.38 arcsec/pix in the visible and 0.64 arcsec/pix in the infrared
Real-time data processing	$<$ 5 minutes

Filter	Exposures	Dark night	Bright night
g	8×30s	22.22	21.16
r	8×30s	22.00	21.38
i	8×30s	21.42	20.87
z	8×30s	20.51	20.21
y	8×30s	19.52	19.52
J	8×30s	19.73	19.73
H	16×13s	18.85	18.85

4.2 Photometric redshift

One of the critical scientific requirement of COLIBRI is to provide a photometric redshift during the first minutes of observations of the GRBs by the SVOM mission. This information is strategic in order to optimize in quasi-real time the observation program carried out on the GRB.

To fulfill this requirement, a special attention was paid to the SED fitting procedure to obtain quickly an accurate photometric redshift. This is based on the fit of the overall shape of the spectra and on the detection of the strong spectral properties. In fact only two prominent signatures can really hint information about the redshift: the Lyman-break at 912×(1+z) Åand the Lyman-α at 1216×(1+z) Å.

The relative accuracy is found to be about 10% for $3.5 < z < 8$ and ∼13-14% for $z > 8$ (Ref. 14). It confirms the ability of COLIBRI to detect dusty and highly redshifted GRBs, and to reliably estimate their photometric redshift in less than 5 minutes.

Backup Slides

SVOM

Using the fraction of observed sky per year, simulations show that SVOM/ECLAIRs will detect ~ 80 GRBs/yr

The estimated number of GRB with redshift determination is of the order of ~ 160 (3yr; nominal duration)

Simulated redshift distribution of GRBs to be detected by ECLAIR

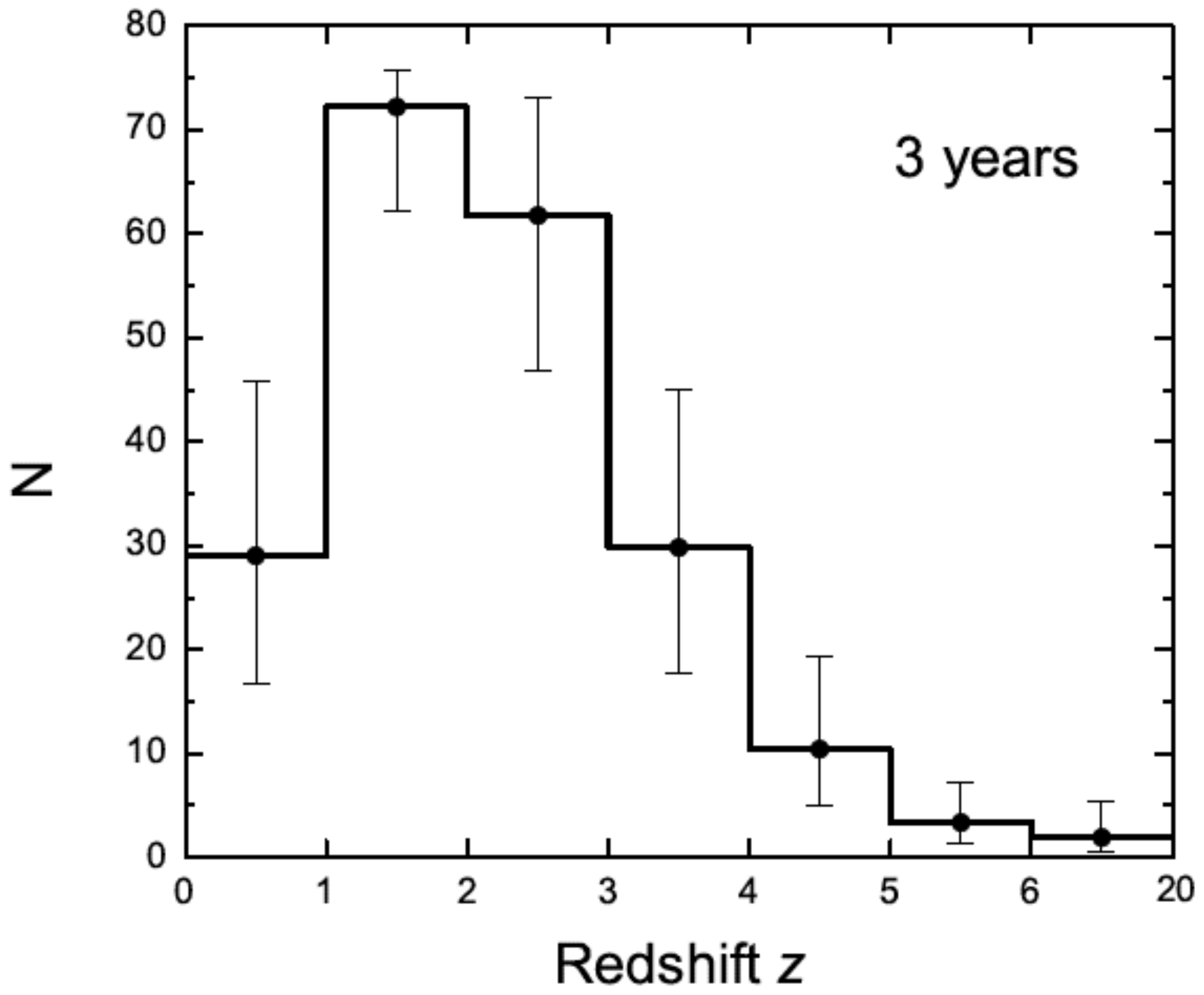

Credits: Wei et al. 2016

Future Prospectives

Backup Slides

Limitations

(i) poor fraction of GRBs with an optical/NIR afterglow spectrum(20-30%)

(ii) lack of satellites capability to detect high-redshift GRBs

Credits: Ghirlanda et al. 2015

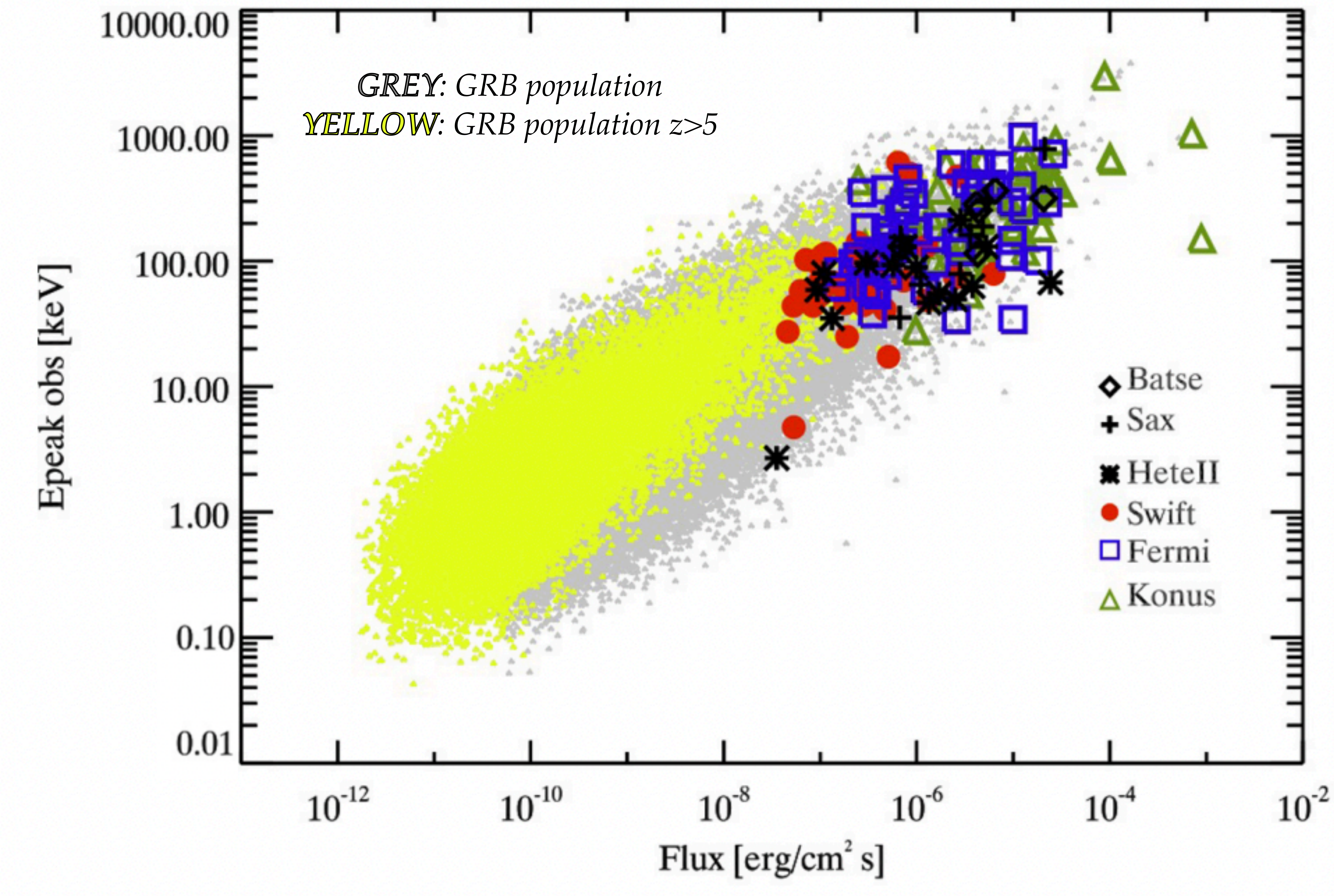

Backup Slides

THESEUS

Selected for ESA M7 Phase-A

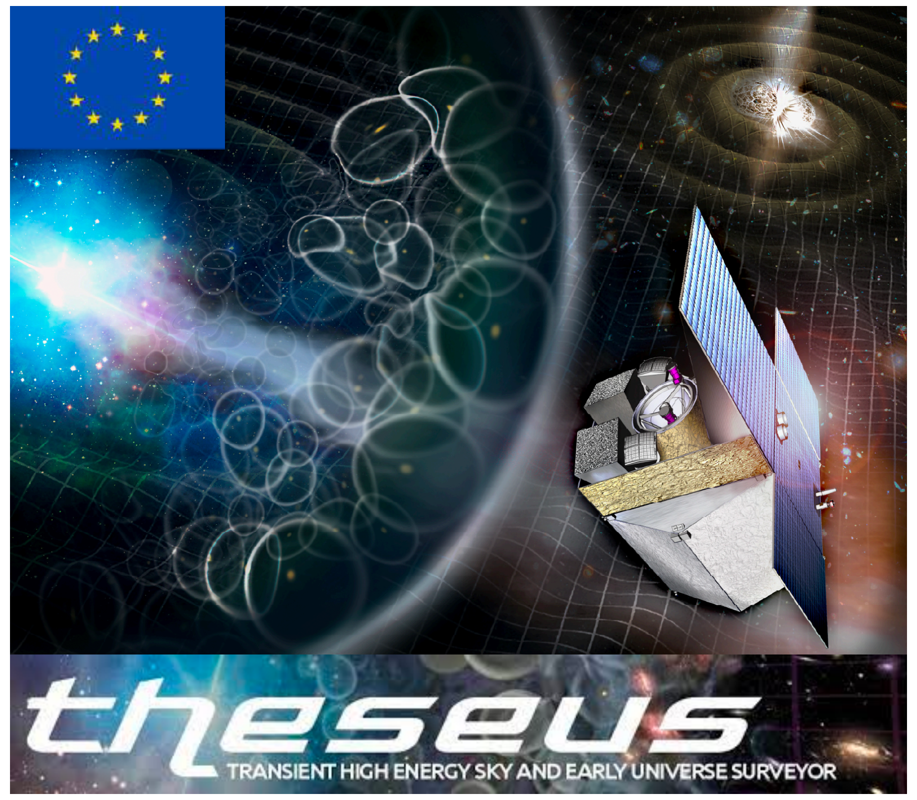

http://www.isdc.unige.ch/theseus

THESEUS Payload

-Soft X-ray Imager (SXI, 0.3 – 5 keV)

-X-Gamma rays Imaging Spectrometer (XGIS, 2 keV – 10 MeV)

-InfraRed Telescope **(IRT, 0.7 – 1.8 μm)**

The predicted annual rate of GRB detections by THESEUS/SXI is ~ 300-700 per year

The estimated number of GRB with redshift determination is of the order of ~ 150-350 per year

THESEUS is expected to detect between 40 and 80 GRBs at z > 6 over a 3.45 yr mission, with between 10 and 25 of these at z > 8 (and several at z > 10).

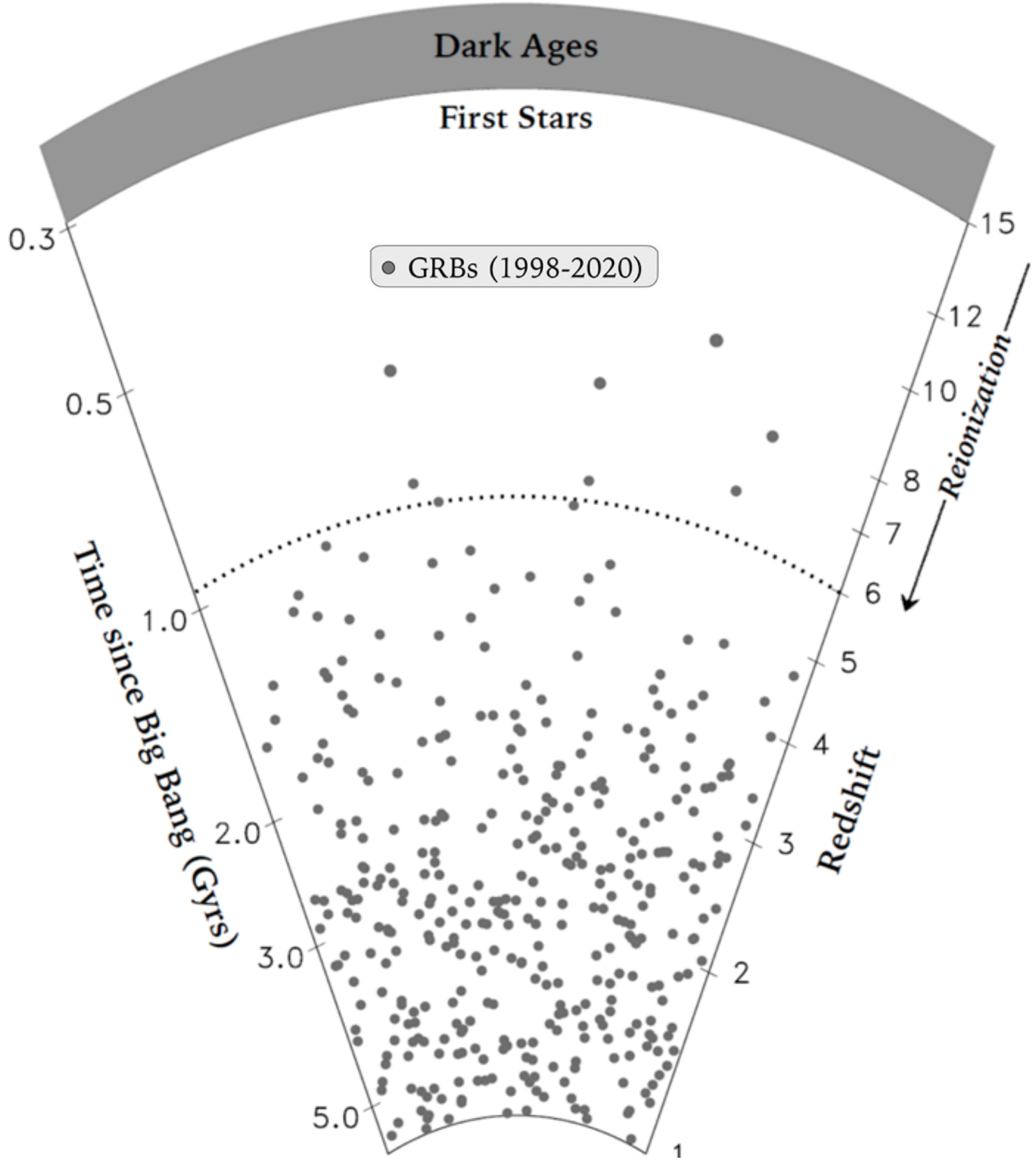

Credits: L. Amati; THESEUS

Backup Slides

THESEUS

Selected for ESA M7 Phase-A

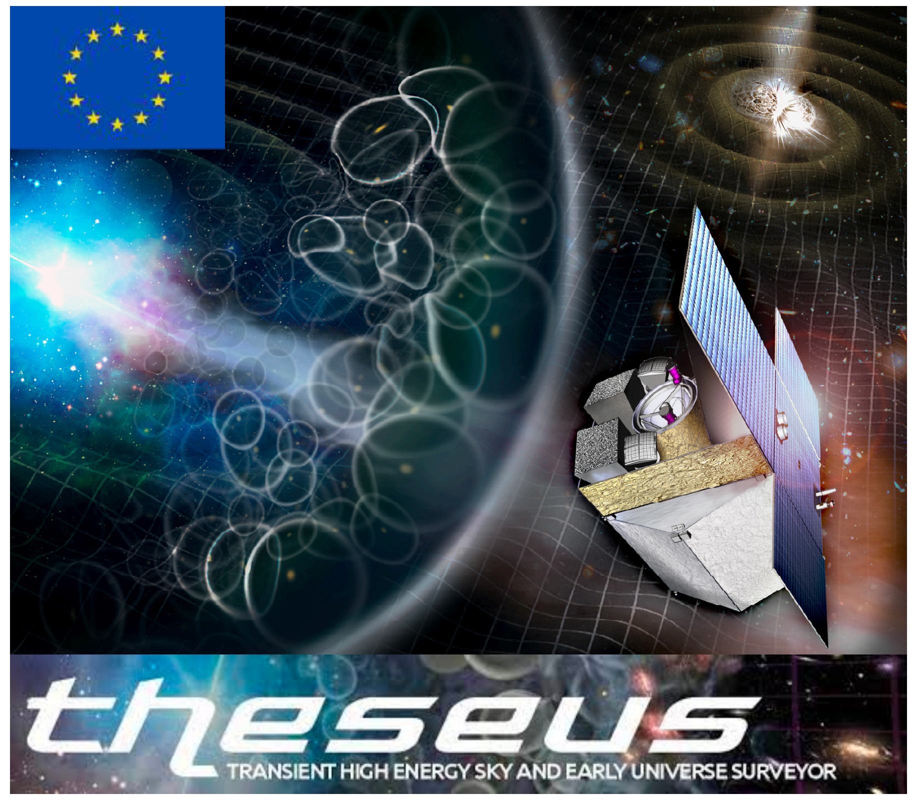

http://www.isdc.unige.ch/theseus

THESEUS Payload

-Soft X-ray Imager (SXI, 0.3 – 5 keV)

-X-Gamma rays Imaging Spectrometer (XGIS, 2 keV – 10 MeV)

-InfraRed Telescope **(IRT, 0.7 – 1.8 μm)**

The predicted annual rate of GRB detections by THESEUS/SXI is ~ 300-700 per year

The estimated number of GRB with redshift determination is of the order of ~ 150-350 per year

THESEUS is expected to detect between 40 and 80 GRBs at $z > 6$ over a 3.45 yr mission, with between 10 and 25 of these at $z > 8$ (and several at $z > 10$).

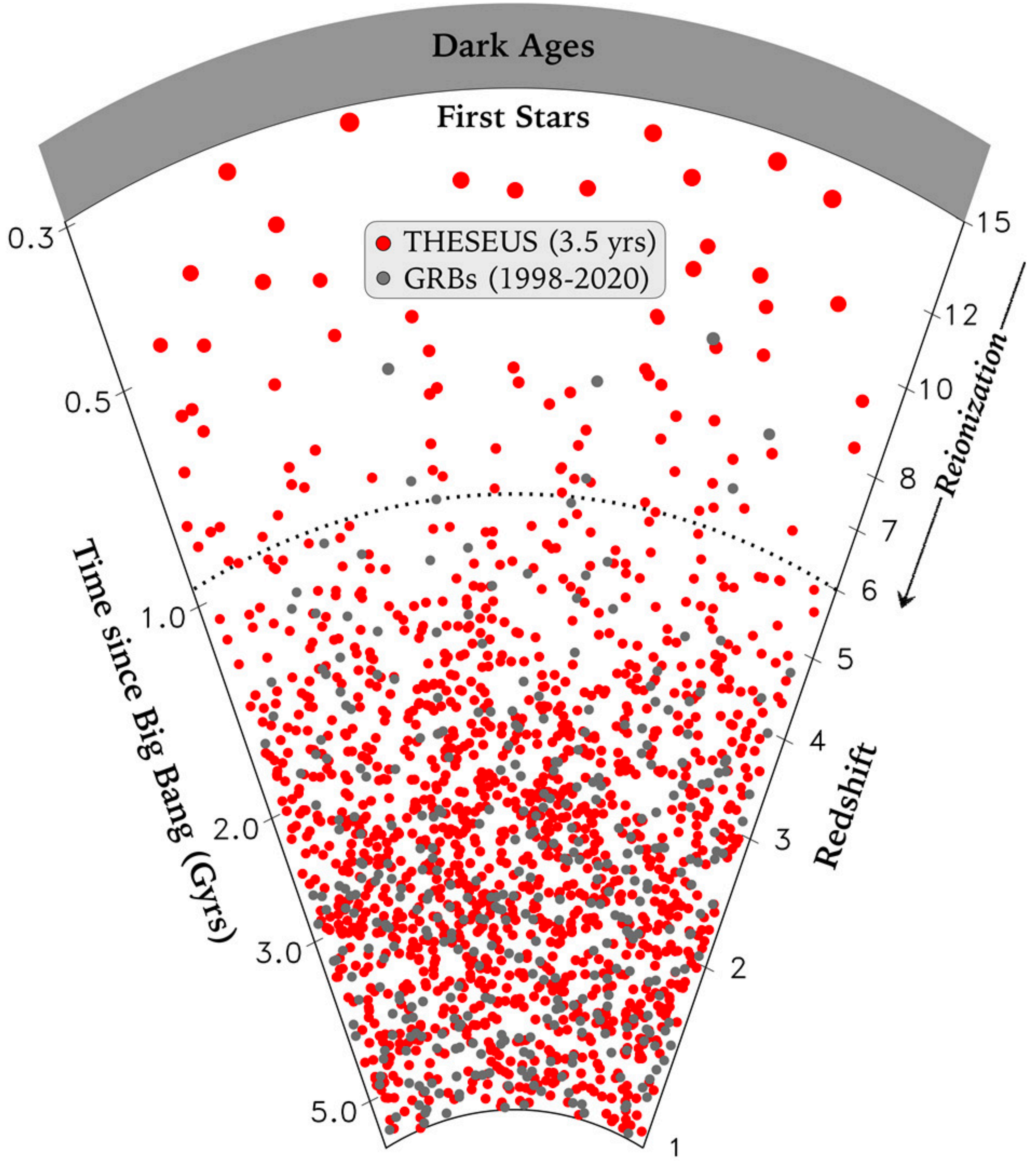

Credits: Theseus Yellow Book

Backup Slides

NEW FACILITIES

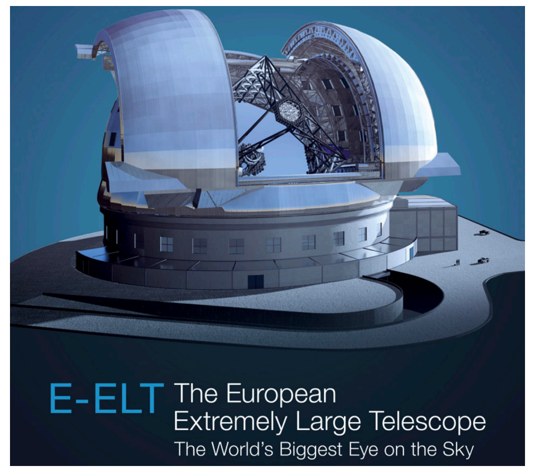

Credits: ESO

ANDES

Marconi et al. 2024

-Three spectrographs (UBV, RIZ, YJH)

-Spectral resolution R~100,000

-Simultaneous wavelength coverage 0.4-1.8 μm

Credits: ANDES White Book (D'Odorico et al. 2023)
Adapted from Saccardi et al. 2023a

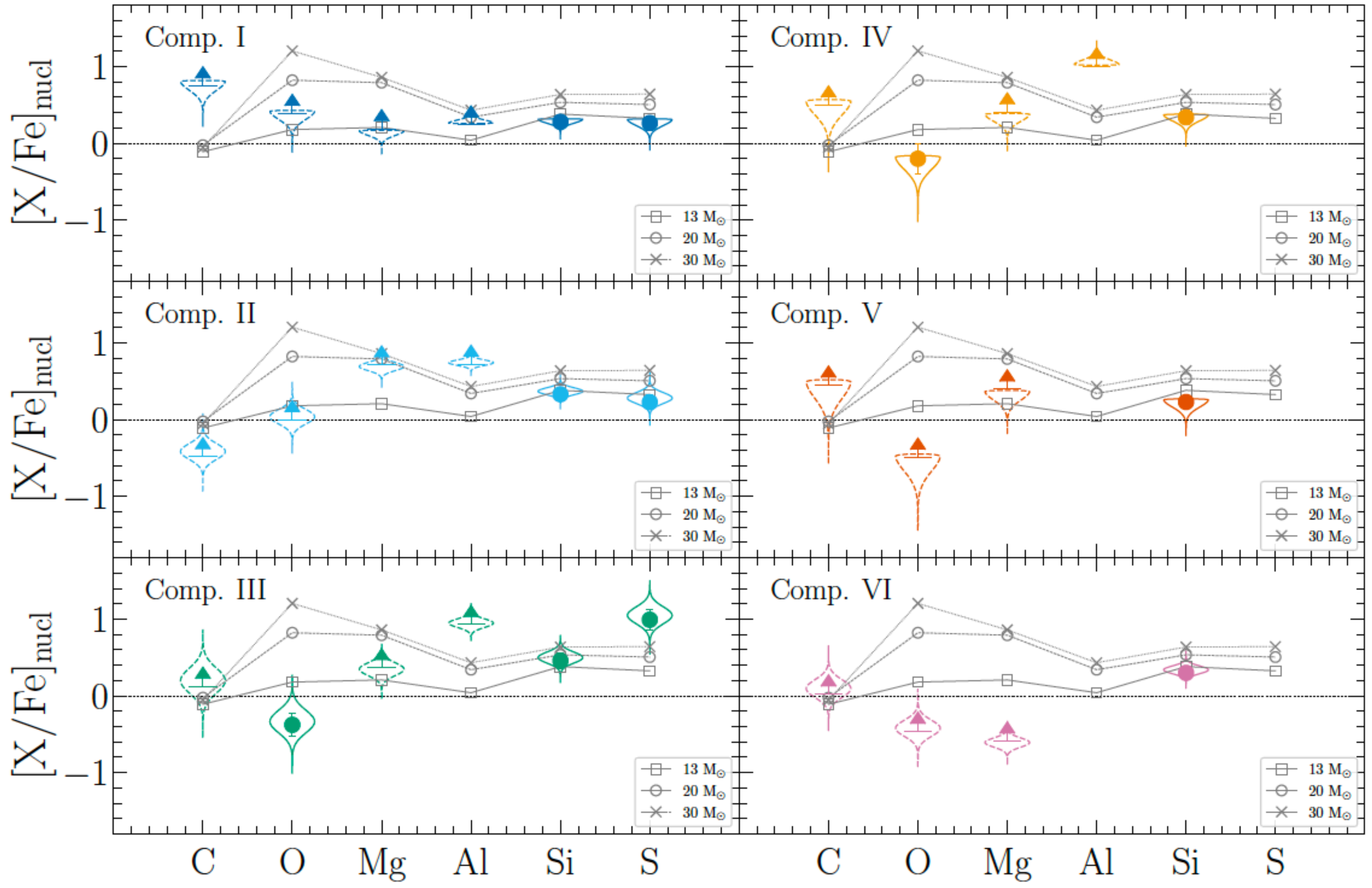

WG3: Galaxy Formation and Evolution and the Inter-Galactic Medium

Allowing to:

(i) reach the **SNR levels** needed to study the faint high-z sources

(ii) constrain **key elements** column density

(iii) study relative abundances in **individual gas components**

(iv) discern between different enrichment scenarios probing the existence of very massive Pop III stars

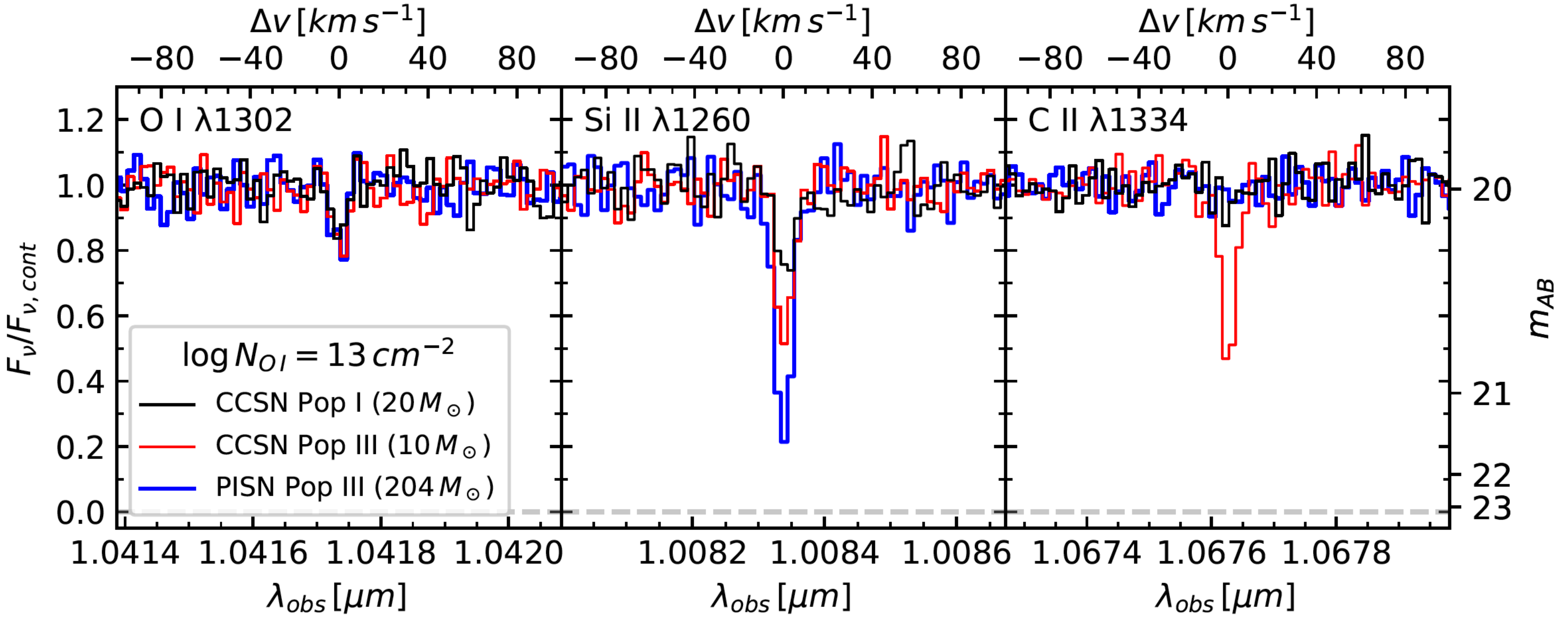

Credits: ANDES White Book (D'Odorico et al. 2023)

Backup Slides

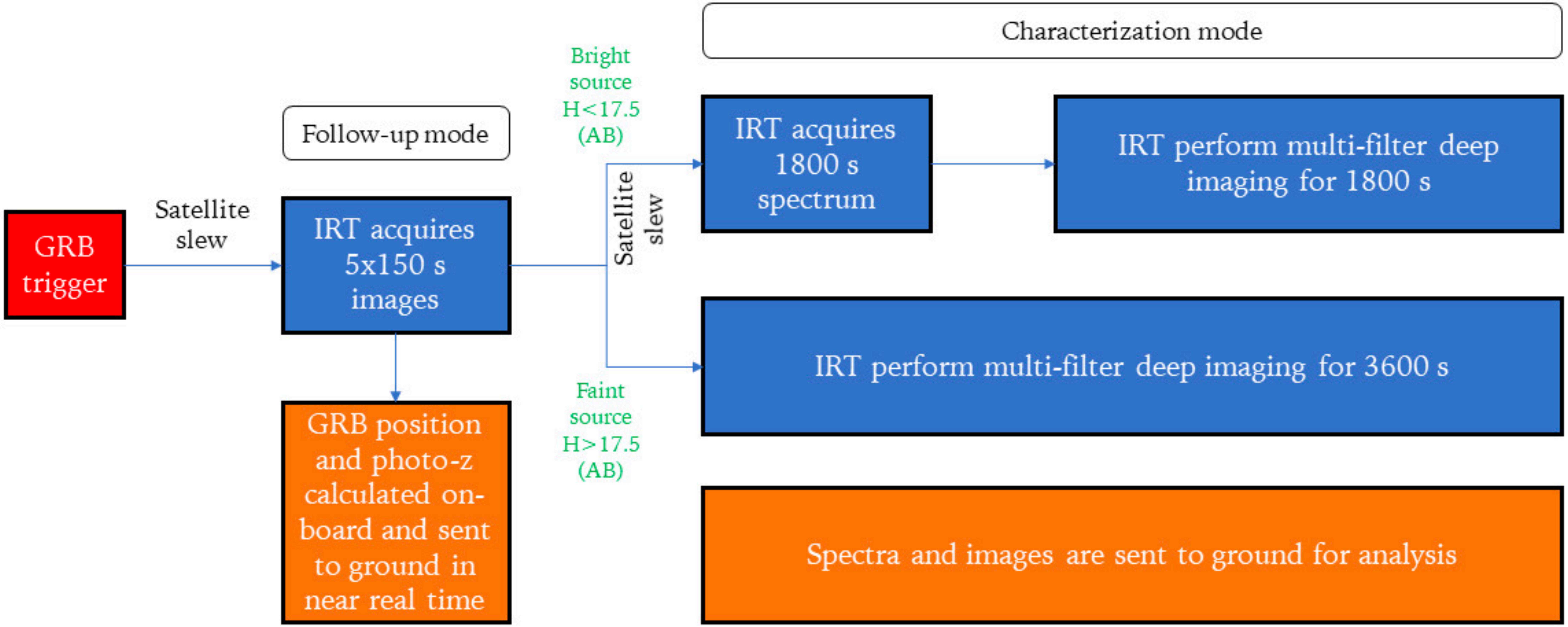

Backup Slides

THESEUS

Fractions

The predicted annual rate of GRB detections by THESEUS/SXI is ~ 300-700 per year

The estimated number of GRB with redshift determination is of the order of ~ 150-350 per year

THESEUS is expected to detect between 40 and 80 GRBs at z > 6 over a 3.45 yr mission, with between 10 and 25 of these at z > 8 (and several at z > 10).

Simulated redshift distribution of GRBs to be detected by SXI
+
Measured redshift on board with IRT

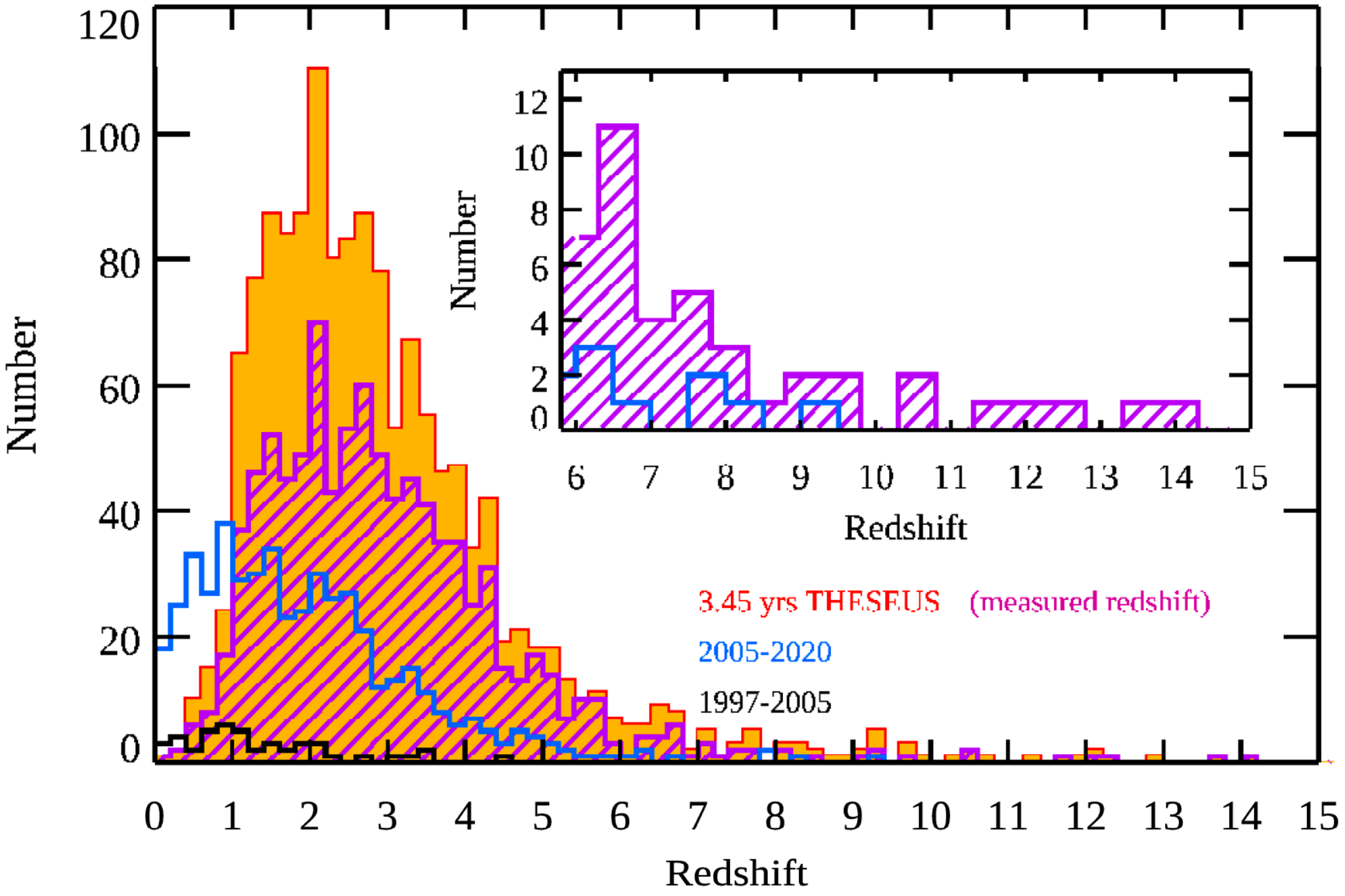

Credits: Theseus Yellow Book